Hematite is a mineralogical marker of ancient climate change on Mars

Marek Szczerba[1†], Tanya S. Peretyazhko[2*†], Elizabeth B. Rampe[3], Thomas F. Bristow[4], Benjamin M. Tutolo[5], Douglas W. Ming[3], David T. Vaniman[6], Richard V. Morris[3], Silas J. Ralston[2], Nikole C. Haney[2], Bum Soo Kim[2], David F. Blake[4], Steve J. Chipera[6], Robert T. Downs[7], Robert M. Hazen[8], Shaunna M. Morrison[8,9], Allan H. Treiman[10], Albert S. Yen[11§], Valerie M. Tu[2], Michael T. Thorpe[12, 13, 14], Cherie N. Achilles[13], David J. Des Marais[4], John P. Grotzinger[15], Nicholas Castle[6], Patricia C. Craig[6], Elisabeth M. Hausrath[16], Sarah L. Simpson[17]

[1] Institute of Geological Sciences, Polish Academy of Sciences, Krakow, Poland.
[2] Amentum, NASA Johnson Space Center, Houston, TX, USA.
[3] Astromaterials Research and Exploration Science Division, NASA Johnson Space Center, Houston, TX, USA.
[4] Exobiology Branch, NASA Ames Research Center, Moffett Field, CA, USA.
[5] Department of Earth, Energy, and Environment, University of Calgary, Calgary, AB, Canada.
[6] Planetary Science Institute, Tucson, AZ, USA.
[7] Department of Geosciences, University of Arizona, Tucson, AZ, USA.
[8] Earth and Planets Laboratory, Carnegie Institution for Science, Washington, DC, USA.
[9] Department of Earth and Planetary Sciences, Rutgers University New Brunswick, Piscataway, NJ, USA
[10] Lunar and Planetary Institute, Universities Space Research Association, Houston, TX, USA.
[11] Jet Propulsion Laboratory, California Institute of Technology, Pasadena, CA, USA.
[12] Department of Astronomy, University of Maryland, College Park, MD, USA.
[13] Solar System Exploration Division, NASA Godard Space Flight Center, Greenbelt, MD, USA.
[14] Center for Research and Exploration in Space Science and Technology, NASA Goddard Space Flight Center, Greenbelt, MD, USA.
[15] Division of Geological and Planetary Sciences, California Institute of Technology, Pasadena, CA, USA.
[16] Department of Geoscience, University of Nevada-Las Vegas, Las Vegas, NV, USA.
[17] Texas State University, Amentum, NASA Johnson Space Center, Houston, TX, USA.

*Corresponding author. Email: tanya.peretyazhko@nasa.gov
[†]These authors contributed equally to this work.
[§]Present address: Planetary Science Institute, Tucson, AZ, USA.

The ancient climate of Mars changed from warm to cold surface conditions. This climate transition is demonstrated by geomorphological evidence, but lacks suitable mineralogical indicators. We investigate the crystallographic properties of hematite (iron oxide) in Gale crater, measured by the Curiosity rover, and compare them to laboratory experiments. Hematite crystallite sizes are ~5 to ~65 nm in the oldest sedimentary rocks investigated by the rover (the Murray formation) and <10 nm in the younger overlying strata (Mirador and Carolyn Shoemaker formations). We attribute the larger crystallites in the Murray formation to post-depositional coarsening by groundwater in warm and wet conditions, which persisted for several million years. Hematite with small crystallites co-occurs with goethite (iron oxyhydroxide) in the overlying layers, consistent with colder and water-limited conditions.

The surface of Mars is cold and dry, but it once had abundant surface water and groundwater. Ancient lake, river, and delta deposits record an active hydrological cycle ~3 to 4 billion years (Ga) ago (*1*). Secondary minerals, formed by water-rock interactions in these sedimentary deposits, constrain the past environmental conditions. However, there is little direct mineralogical evidence of the climate transition from warm to cold. Hematite (α-Fe_2O_3) is a secondary mineral formed by reactions between water and iron-rich minerals. On Mars, iron is released from the silicate minerals in basalt rocks, and from sedimentary rocks derived from basalts, which occur planet-wide (*2*). The crystallographic characteristics of hematite, such as crystallite sizes (single-crystal domains within a grain) and shapes (morphology), are sensitive to formation conditions (*3, 4*). We investigate how these crystallographic parameters, and the Fe-bearing minerals found with hematite, changed on ancient Mars.

The Mars Science Laboratory Curiosity rover is exploring Gale crater (Fig. S1). Prior to rover landing, hematite was identified using orbital visible and near-infrared spectroscopy (*5)*. Orbital observations showed that hematite is concentrated in the Vera Rubin ridge (VRR) area of lower Aeolis Mons (informally called Mount Sharp), a ~5 km-tall mound of layered sedimentary rock within Gale crater (*5, 6*). In situ measurements by the rover have since shown that hematite is not limited to VRR region, but is widespread in Gale crater sedimentary rocks *(7)*.

To characterize mineral assemblages in Gale crater, Curiosity carries the Chemistry and Mineralogy (CheMin) instrument, which performs X-ray diffraction (XRD) measurements of rock powder samples collected using the rover's drill (*8*). XRD peaks identify specific minerals, while their width and shape can quantify the crystallite size and morphology. We investigate the hematite crystallite sizes and shapes in the sedimentary rocks in the stratigraphic sequence of

Murray, Carolyn Shoemaker, and Mirador formations (Fig. 1). We compare the results to experimental data, to determine the processes by which hematite formed and grew (*9*).

Stratigraphic context

Previous studies using CheMin have detected 1 to 16 wt.% hematite (*10*) in lacustrine (lake) mudstones, and fluvial (river) and eolian (wind-blown) sandstones, in the Mount Sharp group (Fig. 1) deposited ~3.6 to 3.2 Ga ago (*11*). We restrict our analysis to samples containing ≥1.5 wt.% hematite, for which the XRD peaks are sufficiently strong to determine the crystallite sizes and shapes. By sol 3627 (Mars days since landing, equivalent to October 2022) the rover had investigated three formations in the Mount Sharp group: i) the Murray formation, the lowest formation, consists of lacustrine mudstones and intervals of fluvial sandstones *(12)*; ii) the Carolyn Shoemaker formation conformably (deposited without interruption) overlies the Murray formation and includes mudstone, siltstone, and sandstone deposited in lake margin or fluvial environments (*13*); and iii) the Mirador formation unconformably overlies the Carolyn Shoemaker formation and is dominated by eolian sandstone (*14*).

The Murray formation contains abundant smectite, a phyllosilicate mineral (Fig. S2), indicating that the ancient fluvial-lacustrine freshwater environments had near-neutral pH (*15-17*). Some drill samples also contain jarosite ($(H_3O^+, K^+, Na^+)Fe_3(SO_4)_2(OH)_6$) and akaganeite (β-FeOOH) (Fig. 1), which are secondary minerals produced by interaction with acidic and saline fluids. The jarosite has been dated to 2.12 ± 0.36 Ga, indicating that those acidic and saline fluids probably arose during a later post-depositional alteration phase (*18*).

The Carolyn Shoemaker formation contains abundant smectite and minor siderite ($FeCO_3$), an Fe(II) carbonate. These indicate that the formation was deposited in near-neutral and fresh waters and was not subsequently altered by acidic fluids (*17*).

The eolian deposits in the Mirador formation indicate a shift to much drier depositional environments. Smectite is absent in this formation, but some locations have hydrated Mg sulfate and siderite. These indicate saline and alkaline water-limited environments, produced by the evaporation of near-surface groundwater (*19, 20*).

None of these formations contain minerals indicative of widespread burial diagenesis (post-depositional changes). Thermal models show that these sedimentary rocks did not experience temperatures >125 °C consistent with smectite preservation (*21*).

Hematite crystallite sizes

Hematite forms hexagonal crystals and crystallites (Fig. 1C). We used the most intense XRD peaks, from the (104) and (110) crystallographic planes, to determine the crystallite sizes in two directions (*9*) (Figs. S3-S24). The (110) peak width provides crystallite size in the a-b plane, whereas the (104) peak width reflects size in the c direction (Fig. 1C). We use whole powder pattern modeling method, with independent fitting of the mean sizes for each hematite peak (*9*). The results (Fig. 1B) show that the (104) crystallite sizes vary substantially with the stratigraphy.

The Carolyn Shoemaker and Mirador formations contain hematite crystallites <10 nm, whereas the Murray formation has crystallites ranging from ~5 to ~65 nm. The largest crystallites occur in the OU and CH drill targets (sample abbreviations are defined in Fig. 1) in the stratigraphically lowest section of this formation. The unit cell parameters do not vary with

crystallite size, indicating negligible ionic substitution (such as Al^{3+}), which would otherwise affect crystallite dimensions and shape (Fig. S25, Table S1).

The derived sizes from the (110) and (104) peaks (Fig. 2A, Table S1) show that the crystallites are of approximately equant thickness in every crystallographic direction, implying uniform growth. This size evolution differs from observations of hematite on Earth, which adopts both platy and equant shape morphologies in a wide range of formation and diagenetic conditions. Figure 2B shows equivalent size measurements for Earth samples: Ediacaran redbeds, paleosols, hydrothermally altered basalt and tuffs of the East European Craton, non-Ediacaran sedimentary rocks, and hydrothermally altered Hawaiian basalt (Tables S3, S4). Hematite crystallites in Gale crater are also smaller than in gray volcanic hematite on Earth (Table S4).

Hematite formation in Gale crater

We consider how the equant-shaped hematite formed and grew in Gale crater, and how it relates to the ancient climate of Mars. For comparison with rover data, we used hematite synthesized by four different processes: forced hydrolysis of Fe(III) solutions (*22*); aqueous alteration of ferrihydrite (poorly-crystalline hydrous Fe(III) oxyhydroxide) (*22-24*); oxidation of Fe(II) during hydrothermal alteration of (Mars analog) basaltic glass (*25*); and thermal decomposition of Fe(III) oxyhydroxides (*9*). We applied the laboratory results to test the plausibility of previous proposals that hematite in Gale crater formed by direct precipitation from solution and alteration of Fe(III) oxyhydroxides (*15, 26*). Although our experimental data do not cover all conditions that could influence hematite formation in complex natural settings such as Gale crater, they do include the presence of Mars-relevant ions (ClO_4^-, Cl^-, SO_4^{2-}, Al^{3+}, Si^{4+}, Mg^{2+}) and a solid substrate (Mars analog basaltic glass, (*9*)).

We find that the hematite could have formed from aqueous alteration of ferrihydrite at neutral to slightly alkaline pH. Crystallites of synthetic hematite formed from ferrihydrite at pH 8 were 7 to 12 nm in size and of equant shape (Fig. 2C), matching the samples from the Murray formation (DU, MJ, SB), and slightly exceeding sizes in the Carolyn Shoemaker and Mirador formations. Goethite, an iron(III) oxyhydroxide (α-FeOOH), usually forms together with hematite produced from ferrihydrite, under a broad pH range (*3*). Goethite occurs with hematite in some samples from the Carolyn Shoemaker and Mirador formations (Fig. 1). The abundance ratios H/(H+G), hematite (H) to the total hematite and goethite (G), are 0.88 ± 0.14 for NT, 0.85 ± 0.27 for PT, 0.75 ± 0.13 for MG, 0.63 ± 0.23 for AV, and 0.68 ± 0.18 for CA. These ratios are consistent with ferrihydrite crystallization to hematite and goethite at pH 6-8 (*27*). Goethite is absent in the Murray formation, which we attribute to the loss of goethite during later diagenesis (discussed below).

Small hematite crystallites might alternatively form by dehydration of ferrihydrite at elevated temperatures, such as would be experienced by burial diagenesis in Gale crater. We performed thermal alteration experiments on three Fe(III) oxyhydroxides that have been identified in Gale crater: goethite, akaganeite, and ferrihydrite (*16, 26, 28*). The resulting crystallites were either of platy morphology (formed from goethite, Fig. 2D), unlike the equant shapes found in Gale crater, or required higher temperatures than the estimated maximum during burial diagenesis (125 °C) for rocks in Gale crater (*21*) (from akaganeite at 450 °C, Fig. 2D). Only ferrihydrite heated at 100 °C produced equant <10 nm hematite consistent with the small <10 nm crystallites in Gale crater (Fig. 2D). We consider this temperature an upper limit on anhydrous ferrihydrite alteration; however, small hematite crystallites with equant shape can also form from ferrihydrite at lower temperatures (such as ~17 °C (*29*); Table S1).

We also considered formation of hematite under acidic conditions (Fig. 2C) (*9*). Crystallites of equant shape formed only under extreme acidic pH < 2, unlikely for Gale crater. Otherwise, Fe(III) sulfate minerals would have formed instead of hematite. We therefore exclude this possibility.

The combination of equant shapes and small crystallite sizes indicates that ferrihydrite is a plausible hematite precursor in Gale crater. We found that <10 nm hematite crystallites of equant shape could form by ferrihydrite alteration by low-temperature solid-state reactions or in solutions with neutral or slightly alkaline pH. However, an additional mechanism is required to explain the larger crystallites in the Murray formation.

Ostwald ripening of Murray formation hematite

Hematite crystallites in the Murray formation have log-normal size distributions (Fig. 3A). The samples with the largest hematite crystallites (CH, OU) from the lowest stratigraphic levels lack <10 nm crystallites, while all other samples do include such small crystallites (Fig. 3A) (*9*). We infer that hematite grows by Ostwald ripening, with dissolution of smaller crystallites feeding the growth of larger ones (*30*). The measured evolution of the log-normal distributions is consistent with theoretical predictions for Ostwald ripening in a closed system (*30*) (Fig. 3B).

Interpretation of hematite in Gale crater

Our analyses indicate that hematite in the sedimentary rocks in Gale crater could have formed from the same precursor, ferrihydrite, but crystallite growth differed between the Murray formation and the overlying Carolyn Shoemaker and Mirador formations. Figure 4 shows our conceptual model for how this might have occurred.

We propose that ferrihydrite in the Murray and Carolyn Shoemaker formations formed in lacustrine settings, but in the Mirador formation ferrihydrite formed through interaction with oxidizing groundwater as conditions became drier and water-limited. The sedimentary rocks then experienced two phases of diagenesis. During early diagenesis, neutral or slightly alkaline groundwater partially or completely transformed ferrihydrite into hematite and goethite. Small hematite crystallites continued forming from ferrihydrite after sediment drying and lithification under low-temperature [<125 °C, (*21*)] diagenesis (Fig. 4). Goethite likely did not form then, as low moisture favors hematite crystallization from ferrihydrite (*31*). Previously formed goethite was unaffected, because this would produce platy hematite (Fig. 2D), which is not observed.

We attribute the lack of goethite in the Murray formation to its removal during late diagenesis. Goethite transforms to hematite in warm (≥ 50 °C), neutral to alkaline (pH ~ 7 to 12) solutions (*9, 32, 33*). Similarly warm late diagenetic fluids have been proposed to explain hematite coarsening in the Murray formation (*26*). We hypothesize that these warm fluids removed goethite (or lowered its abundance below the CheMin detection limit), followed by hematite precipitation (Fig. 4). This late diagenesis favored hematite coarsening by Ostwald ripening in a closed system, by facilitating the dissolution of small crystallites and uptake of Fe(III) into larger crystallites. The measured variable degree of coarsening in the Murray formation (Fig. 1B) may reflect differences in water activity frequency, duration, or solution pH. We estimate that the time necessary for crystallites to grow from the size of Duluth (DU) crystallites (~5 nm) to the size of Confidence Hills (CH) crystallites (~65 nm) is 1.1 to 4.7 million years (Ma) at pH 7, and ~4 days to 27 yrs at pH 2 and 50 °C, dependent on the solution composition (*9, 34*). The calculated time reflects the total duration of water presence, whether continuous or episodic. A minimum pH ~ 7 is necessary for concurrent goethite alteration and

hematite coarsening. Under this scenario, warm groundwater might have persisted for up to ~4.7 Ma, at least in the deepest layers of Gale crater. Such long-lived aquifers could have been potentially habitable, though other criteria are also required for habitability.

Goethite is still present in the Carolyn Shoemaker and Mirador formations, suggesting lower temperatures prevented its transformation into hematite (<50 °C, (*9*)). Adopting a thermal model of the sedimentary rocks along the Curiosity traverse *(20)*, we suggest that this difference in rock temperatures could reflect the shift of Mars' climate from warmer (surface temperatures ≥0 °C) to the colder conditions that persist today (Fig. 5, (*9*)). We attribute the presence of <10 nm hematite crystallites in these formations to a combination of the shorter duration of water activity, and the climate transition to drier and colder conditions, compared to the formation and evolution of hematite in the Murray formation (Fig. 4).

The proposed model is an extension of our hypothesis that in the Murray formation, goethite formed with hematite then was removed by diagenesis. Alternatively, hematite alone could have formed from ferrihydrite in saline solutions (*35*) previously inferred in Gale crater (*19*). We cannot distinguish between these possibilities.

Hematite as a climate change marker

Our analysis shows that hematite crystallographic characteristics, and its co-occurrence with goethite, reflect diagenetic and climate conditions on ancient Mars. In the Carolyn Shoemaker and Mirador formations, small hematite crystallites coexisting with goethite indicate lower burial temperatures and shorter duration of water exposure than in the Murray formation, which experienced warmer and wetter conditions, resulting in goethite loss and hematite coarsening. Calculations show that hematite growth persisted for a total of up to 4.7 Ma at near-neutral pH, indicating the intermittent or continuous groundwater presence.

References

1. M. C. Malin, K. S. Edgett, Sedimentary rocks of early Mars. *Science* **290**, 1927-1937 (2000).
2. J. L. Bandfield, A. D. Rogers, Olivine dissolution by acidic fluids in Argyre Planitia, Mars: Evidence for a widespread process? *Geology* **36**, 579-582 (2008).
3. R. Cornell, U. Schwertmann, *The iron oxides: structure, properties, reactions, occurrence and uses*. (VCH, 2003).
4. J. Środoń *et al.*, Thermal history of the central part of the Karst Dinarides, Croatia: Combined application of clay mineralogy and low-T thermochronology. *Tectonophysics* **744**, 155-176 (2018).
5. A. Fraeman *et al.*, The stratigraphy and evolution of lower Mount Sharp from spectral, morphological, and thermophysical orbital data sets. *J. Geophys. Res. Planets* **121**, 1713-1736 (2016).
6. A. Fraeman *et al.*, A hematite-bearing layer in Gale Crater, Mars: Mapping and implications for past aqueous conditions. *Geology* **41**, 1103-1106 (2013).
7. E. B. Rampe *et al.*, Mineralogy and geochemistry of sedimentary rocks and eolian sediments in Gale crater, Mars: A review after six Earth years of exploration with Curiosity. *Geoch* **80**, 125605 (2020).
8. D. Blake *et al.*, Characterization and calibration of the CheMin mineralogical instrument on Mars Science Laboratory. *Space Sci. Rev.* **170**, 341-399 (2012).
9. Materials and methods are available as supplementary materials.
10. M. Szczerba, T. S. Peretyazhko, T. F. Bristow, Data from: Hematite is a mineralogical marker of ancient climate change on Mars. *Astrobiology Habitable Environment Database* (2026); https://doi.org/10.48667/0v03-m213.
11. J. Grotzinger *et al.*, Deposition, exhumation, and paleoclimate of an ancient lake deposit, Gale crater, Mars. *Science* **350**, aac7575 (2015).
12. L. A. Edgar *et al.*, A lacustrine paleoenvironment recorded at Vera RubinRidge, Gale crater: Overview of the sedimentology and stratigraphy observed by the Mars Science Laboratory Curiosity Rover. *J. Geophys. Res. Planets* **125**, e2019JE006307 (2020).
13. C. M. Fedo *et al.*, Geology and stratigraphic correlation of the Murray and Carolyn Shoemaker formations across the Glen Torridon region, Gale crater, Mars. *J. Geophys. Res. Planets* **127**, e2022JE007408 (2022).
14. M. J. Meyer *et al.*, Geological context and significance of the clay-sulfate transition region in Mount Sharp, Gale crater, Mars: An integrated assessment based on orbiter and rover data. *Geol. Soc. Am. Bull.* **137**, 82-115 (2024).
15. J. A. Hurowitz *et al.*, Redox stratification of an ancient lake in Gale crater, Mars. *Science* **356**, eaah6849 (2017).
16. E. B. Rampe *et al.*, Mineralogy of an ancient lacustrine mudstone succession from the Murray formation, Gale crater, Mars. *Earth. Planet. Sci. Lett.* **471**, 172-185 (2017).
17. M. T. Thorpe *et al.*, Mars Science Laboratory CheMin data from the Glen Torridon region and the significance of lake-groundwater interactions in interpreting mineralogy and sedimentary history. *J. Geophys. Res. Planets* **127**, e2021JE007099 (2022).
18. P. Martin *et al.*, A two-step K-Ar experiment on Mars: Dating the diagenetic formation of jarosite from Amazonian groundwaters. *J. Geophys. Res. Planets* **122**, 2803-2818 (2017).
19. S. Chipera *et al.*, Mineralogical investigation of Mg-Sulfate at the Canaima drill site, Gale crater, Mars. *J. Geophys. Res. Planets* **128**, e2023JE008041 (2023).

20. B. M. Tutolo *et al.*, Carbonates identified by the Curiosity rover indicate a carbon cycle operated on ancient Mars. *Science* **388**, 292-297 (2025).
21. C. S. Borlina, B. L. Ehlmann, E. S. Kite, Modeling the thermal and physical evolution of Mount Sharp's sedimentary rocks, Gale crater, Mars: Implications for diagenesis on the MSL Curiosity rover traverse. *J. Geophys. Res. Planets* **120**, 1396-1414 (2015).
22. T. Peretyazhko, D. Ming, E. Rampe, R. Morris, D. Agresti, Effect of solution pH and chloride concentration on akaganeite precipitation: Implications for akaganeite formation on Mars. *J. Geophys. Res. Planets* **123**, 2211-2222 (2018).
23. T. S. Peretyazhko *et al.*, Synthesis of akaganeite in the presence of sulfate: Implications for akaganeite formation in Yellowknife Bay, Gale Crater, Mars. *Geochim. Cosmochim. Acta* **188**, 284-296 (2016).
24. T. S. Peretyazhko, D. W. Ming, R. V. Morris, D. G. Agresti, W. P. Buckley, Formation of Fe (III) (hydr)oxides from Fe (II) sulfides: Implications for akaganeite detection on Mars. *ACS Earth Space Chem.* **5**, 1934-1947 (2021).
25. S. Ralston *et al.*, Phyllosilicate formation on early Mars via open-system acid alteration of basaltic glass. *Earth. Planet. Sci. Lett.* **603**, 117987 (2023).
26. E. B. Rampe *et al.*, Mineralogy of Vera Rubin Ridge from the Mars Science Laboratory CheMin Instrument. *J. Geophys. Res. Planets* **125**, e2019JE006306 (2020).
27. U. Schwertmann, E. Murad, Effect of pH on the formation of goethite and hematite from ferrihydrite. *Clays Clay Miner.* **31**, 277-284 (1983).
28. D. T. Vaniman *et al.*, Mineralogy of a mudstone at Yellowknife Bay, Gale crater, Mars. *Science* **343**, 1243480 (2014).
29. T. S. Peretyazhko, S. J. Ralston, B. Sutter, D. W. Ming, Evidence for adsorption of chlorine species on iron(III) (hydr)oxides in the Sheepbed mudstone, Gale crater, Mars. *J. Geophys. Res. Planets* **125**, e2019JE006220 (2020).
30. D. Eberl, V. Drits, J. Srodon, Deducing growth mechanisms for minerals from the shapes of crystal size distributions. *Am. J. Sci.* **298**, 499-533 (1998).
31. Y. Cudennec, A. Lecerf, The transformation of ferrihydrite into goethite or hematite, revisited. *J. Solid State Chem.* **179**, 716-722 (2006).
32. S. Das, M. J. Hendry, J. Essilfie-Dughan, Transformation of two-line ferrihydrite to goethite and hematite as a function of pH and temperature. *Environ. Sci. Technol.* **45**, 268-275 (2011).
33. X. Wang *et al.*, Formation and secondary mineralization of ferrihydrite in the presence of silicate and Mn (II). *Chem. Geol.* **415**, 37-46 (2015).
34. K. Miyazaki, A numerical simulation of textural evolution due to Ostwald ripening in metamorphic rocks: A case for small amount of volume of dispersed crystals. *Geochim. Cosmochim. Acta* **60**, 277-290 (1996).
35. J. Torrent, R. Guzman, Crystallization of Fe (III)-oxides from ferrihydrite in salt solutions: osmotic and specific ion effects. *Clay Minerals* **17**, 463-469 (1982).
36. P. Dera *et al.*, High pressure single-crystal micro X-ray diffraction analysis with GSE_ADA/RSV software. *High Press. Res.* **33**, 466-484 (2013).
37. D. Golden, D. Ming, R. Morris, T. Graff, Hydrothermal synthesis of hematite spherules and jarosite: Implications for diagenesis and hematite spherule formation in sulfate outcrops at Meridiani Planum, Mars. *Am. Mineral.* **93**, 1201-1214 (2008).
38. C. Achilles *et al.*, Evidence for multiple diagenetic episodes in ancient fluvial-lacustrine sedimentary rocks in Gale crater, Mars. *J. Geophys. Res. Planets* **125**, e2019JE006295 (2020).

39. D. Balzar, "Voigt-function model in diffraction line-broadening analysis" in *Defect and microstructure analysis by diffraction,* R. L. Snyder, J. Fiala, H. J. Bunge, Eds. (Oxford University Press, 1999), pp. 94-126,
40. P. Scardi, C. L. Azanza Ricardo, C. Perez-Demydenko, A. A. Coelho, Whole powder pattern modelling macros for TOPAS. *J. Appl. Crystallogr.* **51**, 1752-1765 (2018).
41. S. J. Smith *et al.*, Novel synthesis and structural analysis of ferrihydrite. *Inorg. Chem.* **51**, 6421-6424 (2012).
42. K. Ståhl *et al.*, On the akaganéite crystal structure, phase transformations and possible role in post-excavational corrosion of iron artifacts. *Corros. Sci.* **45**, 2563-2575 (2003).
43. U. Schwertmann, R. M. Cornell, *Iron oxides in the laboratory: preparation and characterization*. (Wiley-VCH, 2000).
44. Standard reference material 660a; lanthanum hexaboride powder line position and line shape standard for powder diffraction (National Institute of Standards and Technology, US Department of Commerce, Gaithersburg, 2000).
45. J. Środoń, "Illitization of smectite and history of sedimentary basins" in *Proceedings of the 11th EUROCLAY Conference* (Aveiro, Portugal, 2007), pp. 74-82,
46. R. V. Morris *et al.*, Hydrothermal precipitation of sanidine (adularia) having full Al, Si structural disorder and specular hematite at Maunakea volcano (Hawai'i) and at Gale Crater (Mars). *J. Geophys. Res. Planets* **125**, e2019JE006324 (2020).
47. K. Fukushi, Y. Sekine, E. B. Rampe, Reconstruction of pH, redox condition, and concentrations of major components in ancient liquid water from the Karasburg member, Murray formation, Gale Crater, Mars. *Geochim. Cosmochim. Acta* **325**, 129-151 (2022).
48. K. Fukushi, Y. Sekine, H. Sakuma, K. Morida, R. Wordsworth, Semiarid climate and hyposaline lake on early Mars inferred from reconstructed water chemistry at Gale. *Nat. Commun.* **10**, 1-11 (2019).
49. E. S. Kite, S. Conway, Geological evidence for multiple climate transitions on Early Mars. *Nat. Geosci.***17**, 10-19 (2024).
50. B. M. Hynek, K. L. Rogers, M. Antunovich, G. Avard, G. E. Alvarado, Lack of microbial diversity in an extreme Mars analog setting: Poás Volcano, Costa Rica. *Astrobiology* **18**, 923-933 (2018).
51. M. Y. Zolotov, M. V. Mironenko, Timing of acid weathering on Mars: A kinetic-thermodynamic assessment. *J. Geophys. Res. Planets* **112**, (2007).
52. J. Bigham, U. Schwertmann, S. Traina, R. Winland, M. Wolf, Schwertmannite and the chemical modeling of iron in acid sulfate waters. *Geochim. Cosmochim. Acta* **60**, 2111-2121 (1996).
53. C. I. Fassett, J. W. Head III, Valley network-fed, open-basin lakes on Mars: Distribution and implications for Noachian surface and subsurface hydrology. *Icarus* **198**, 37-56 (2008).
54. S. Das, M. J. Hendry, Characterization of hematite nanoparticles synthesized via two different pathways. *J. Nanopart. Res.* **16**, 1-16 (2014).
55. L. E. Davidson, S. Shaw, L. G. Benning, The kinetics and mechanisms of schwertmannite transformation to goethite and hematite under alkaline conditions. *Am. Mineral.* **93**, 1326-1337 (2008).
56. H. Vu, S. Shaw, L. G. Benning, Transformation of ferrihydrite to hematite: an in situ investigation on the kinetics and mechanisms. *Mineral. Mag.* **72**, 217-220 (2008).
57. A. A. Fraeman *et al.*, Synergistic ground and orbital observations of iron oxides on Mt. Sharp and Vera Rubin ridge. *J. Geophys. Res. Planets* **125**, e2019JE006294 (2020).

58. Context of Curiosity landing site in Gale crater, with ellipse (2011); https://science.nasa.gov/resource/context-of-curiosity-landing-site-in-gale-crater-with-ellipse/.
59. A. R. Vasavada *et al.*, Overview of the Mars Science Laboratory mission: Bradbury Landing to Yellowknife Bay and beyond. *J. Geophys. Res. Planets* **119**, 1134-1161 (2014).
60. F. J. Calef III, T. Parker, "MSL Gale merged orthophoto mosaic," (U.S.G.S. PDS Annex, 2016); https://astrogeology.usgs.gov/search/map/mars_msl_gale_merged_orthophoto_mosaic_25cm.
61. B. Lafuente, R. T. Downs, H. Yang, & , N. Stone, "The power of databases: the RRUFF project. " in *Highlights in Mineralogical Crystallography,* T. Armbruster, R. M. Danisi, Eds. (W. De Gruyter, Berlin, Germany, 2015), https://www.rruff.net/.
62. M. Paszkowski *et al.*, Detrital zircon U-Pb and Hf constraints on provenance and timing of deposition of the Mesoproterozoic to Cambrian sedimentary cover of the East European Craton, Belarus. *Precambrian Res.* **331**, 105352 (2019).
63. A. Derkowski *et al.*, Long-distance fluid migration defines the diagenetic history of unique Ediacaran sediments in the East European Craton. *Basin Research* **33**, 570-593 (2021).
64. J. Środoń *et al.*, Diagenetic history of the Podhale-Orava Basin and the underlying Tatra sedimentary structural units (Western Carpathians): evidence from XRD and K-Ar of illite-smectite. *Clay Minerals* **41**, 751-774 (2006).
65. C. I. Steefel, P. Van Cappellen, A new kinetic approach to modeling water-rock interaction: The role of nucleation, precursors, and Ostwald ripening. *Geochim. Cosmochim. Acta* **54**, 2657-2677 (1990).
66. X. Li *et al.*, Dissolution behavior of isolated and aggregated hematite particles revealed by in situ liquid cell transmission electron microscopy. *Environ. Sci. Technol.* **53**, 2416-2425 (2019).

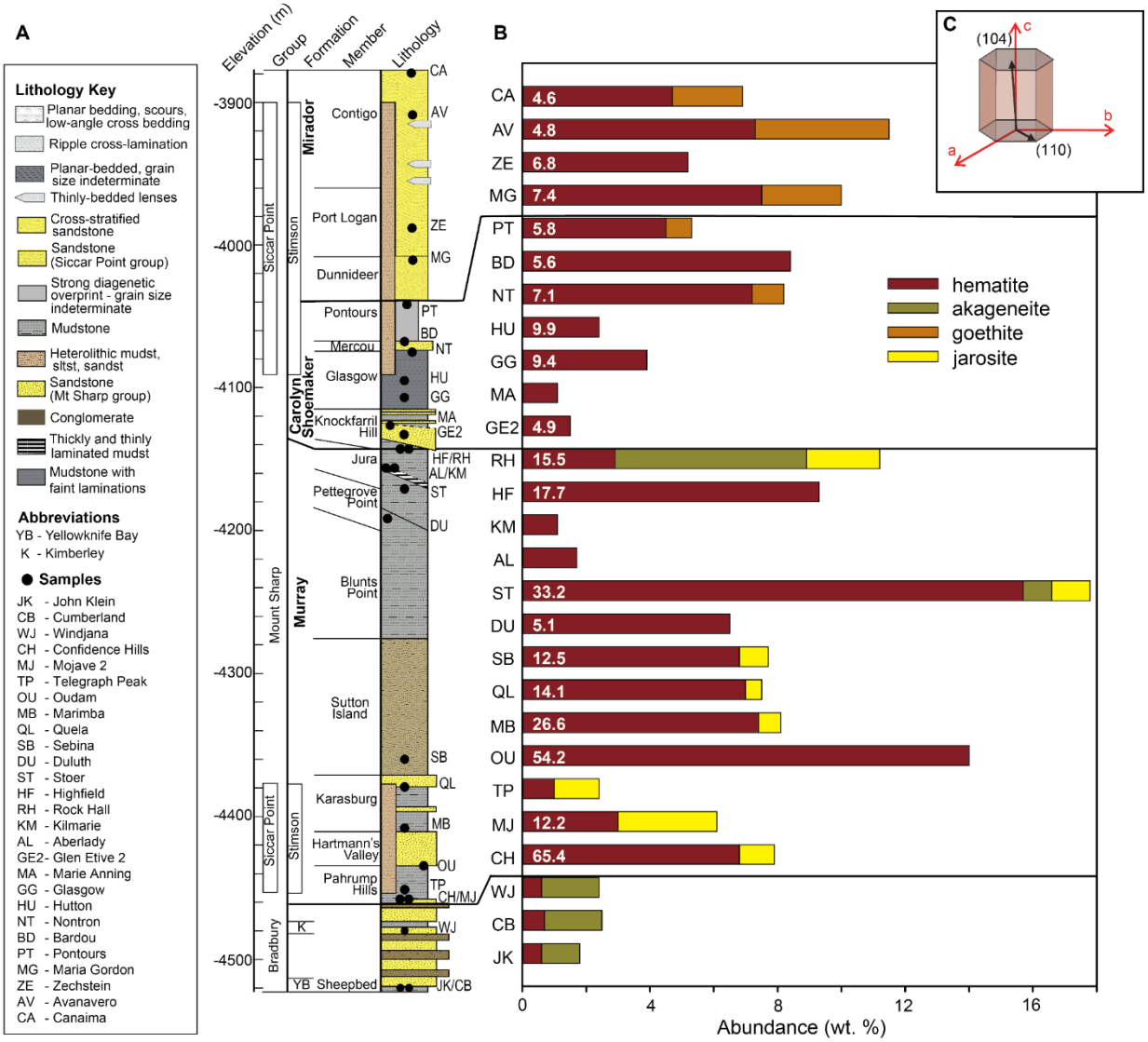

Fig 1. Variations of hematite crystallite size with stratigraphy. (**A**) Stratigraphic column of geologic units investigated by Curiosity through sol 3627. Colors and hatching styles indicate the lithology (see legend). The elevation is relative to the Mars geoid. Sample names and abbreviations are listed in the legend. (**B**) Colored bars indicate the abundances of hematite, goethite, akaganeite, and jarosite (see legend). Numbers within the hematite bars are the hematite crystallite sizes measured from the (104) XRD peak. Samples excluded from analysis have no numbers. (**C**) Crystal structure of hematite. The (104) XRD peak primarily constrains the size in the c direction.

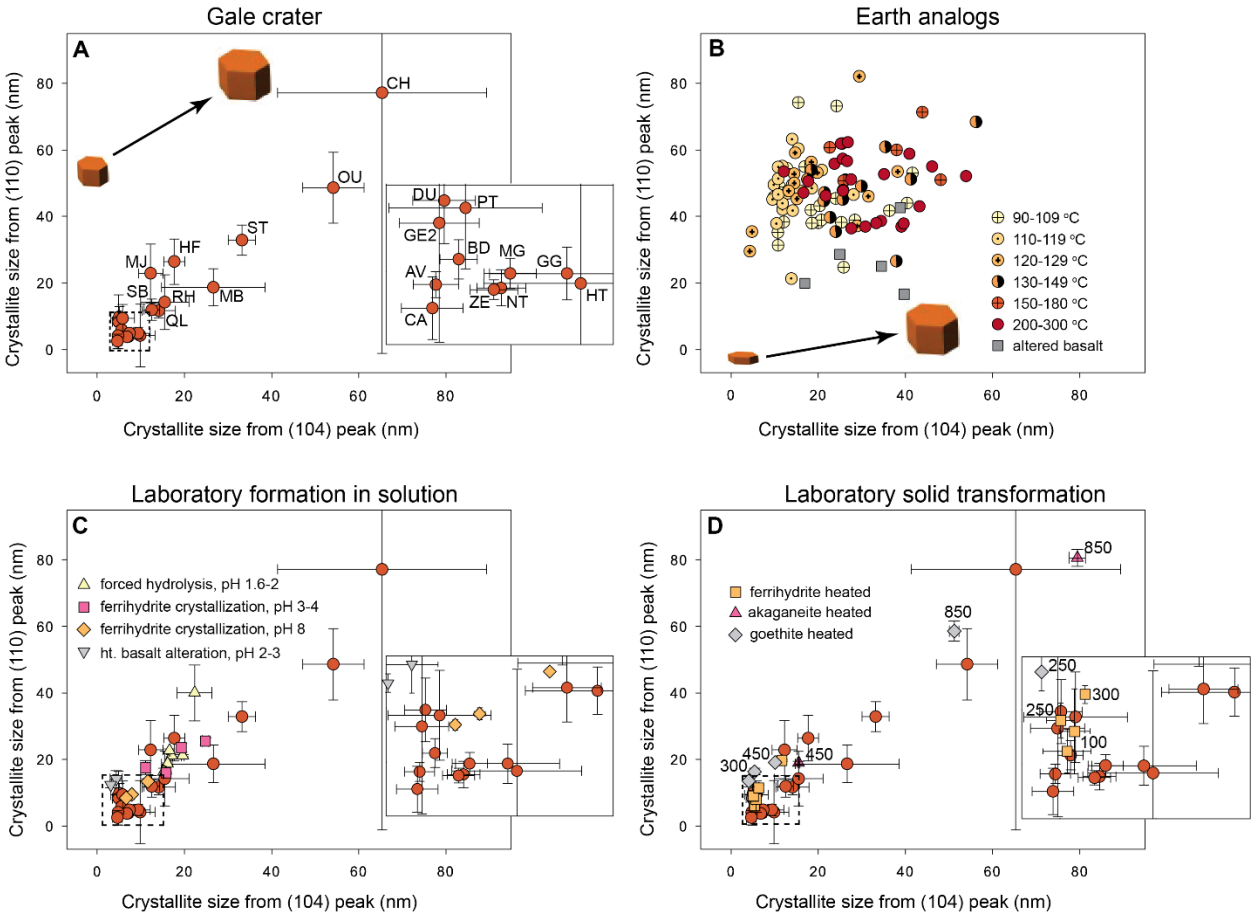

Fig. 2 Two dimensional mean sizes of hematite crystallites. Sizes were derived from whole powder pattern modeling with independent fitting of the (110) and (104) diffraction peaks of hematite. Those peaks constrain the sizes in the two crystallographic directions shown in Fig. 1C. (**A**) Samples from Gale crater (individual XRD spectra are shown in Figs. S5-S24). Data points are the mean values, error bars are 1 sigma. The inset zooms into samples with crystallites <10 nm (dashed box in main panel). (**B**) The same parameters measured from Earth analog samples of natural hematite from the Ediacaran redbeds, paleosols, hydrothermally altered basalt, and tuffs of the East European Craton, non-Ediacaran sedimentary rocks (colored circles indicate maximum paleotemperatures), and altered basalt in Hawaii (gray squares) ((*9*), Tables S3, S4). (**C**) Same Gale crater measurements as panel A (circles), but compared with laboratory experiments (Figs. S26-S31) that formed hematite by acidic hydrolysis (yellow triangles), ferrihydrite crystallization at pH 3 to 4 (purple squares) and pH 8 (orange diamonds), and hydrothermal (ht.) basalt alteration (grey downward triangles). (**D**) Same Gale crater measurements as panel A but compared to laboratory experiments (Figs. S32-S34) that produced hematite by thermal alteration of ferrihydrite (orange squares), akageneite (pink triangles), and goethite (gray diamonds). Labelled numbers are the temperatures in Celsius. For ferrihydrite, the two lowest points correspond to 100 ºC for 2 weeks and 4 months. The insets in panels C and D zoom into samples with crystallites <15 nm (dashed boxes in main panels).

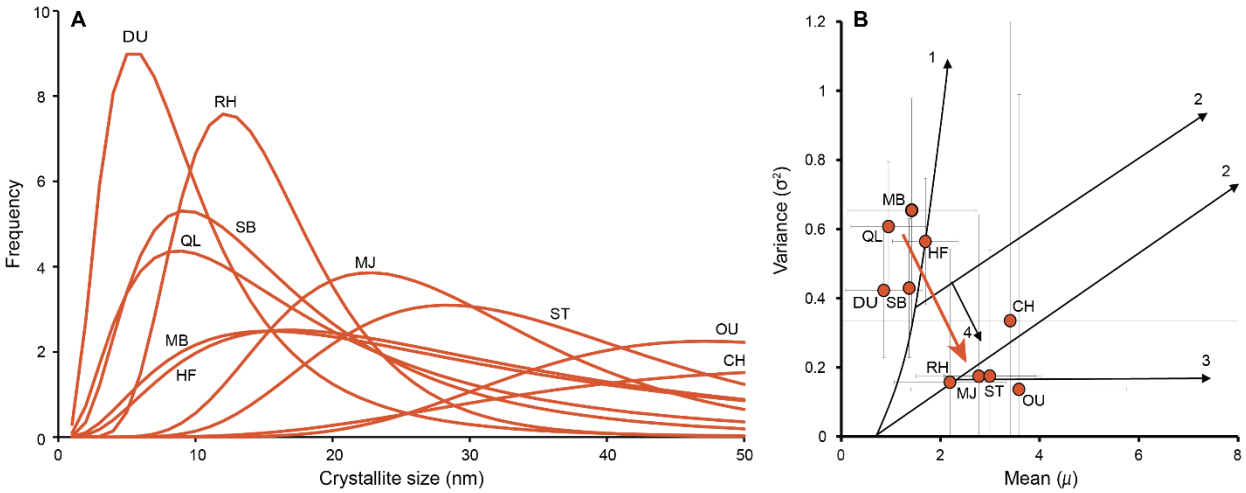

Fig. 3. Size distributions of hematite crystallites. (**A**) Volume-weighted size distributions of hematite crystallites derived from the XRD model fitting (*9*). Each line represents a different sample location (labelled as in Fig. 1). (**B**) The mean (μ) and variance (σ^2) of number-weighted log-normal models fitted to each distribution, error bars are 1 sigma (Table S2). Numbered arrows indicate the expected trends for different growth mechanisms: 1 - continuous nucleation and growth, 2 - surface-controlled growth (open system), each arrow - different initial size distribution; and 3 - random ripening, 4 - Ostwald ripening, both in a closed system (*30*). The directional trend (orange arrow) from smaller to larger crystallites is consistent with Ostwald ripening.

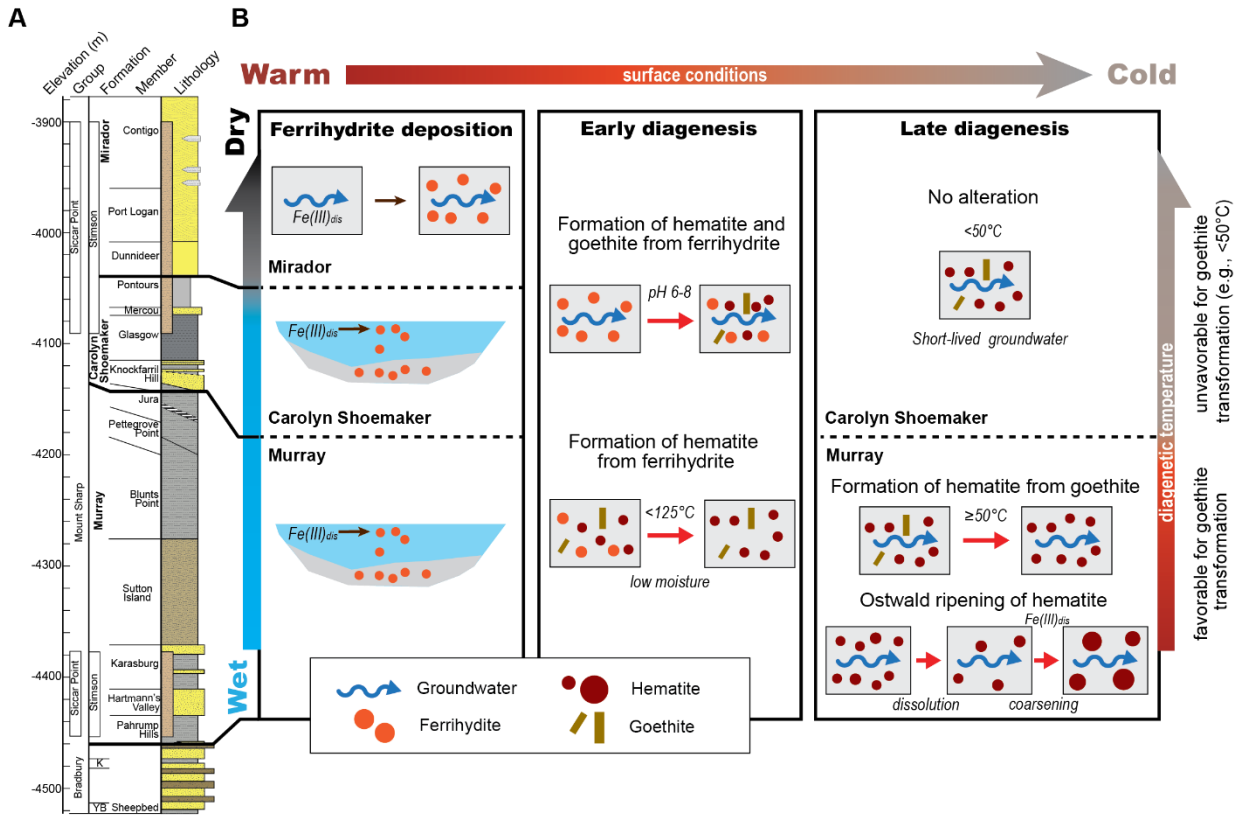

Fig. 4 Proposed conceptual model of hematite formation and evolution in Gale crater. (**A**) Stratigraphic column as in Fig. 1A, showing boundaries between the Murray, Carolyn Shoemaker, and Mirador formations (black lines). **(B)** Left panel: ferrihydrite formation from dissolved Fe(III) and deposition. A gradient-colored arrow indicates a transition from wet (blue) to dry (dark gray) surface conditions reflecting a shift from lacustrine deposition in the Murray and Carolyn Shoemaker formations to groundwater-dominated settings in the Mirador formation. Central panel: early diagenesis forming small hematite crystallites and goethite from ferrihydrite. Right panel: late diagenesis. A gradient-colored arrow shows decreasing diagenetic temperatures from warmer conditions (red), favoring goethite-to-hematite transformations and hematite coarsening in the Murray formation, to colder conditions (gray) that inhibit alterations. A red-to-gray gradient arrow at the top indicates cooling surface temperatures from ≥0 °C to present day conditions. Dotted lines within panels are boundaries between formations. Red arrows within diagenesis panels indicate warm conditions. Symbols for hematite, ferrihydrite, goethite and groundwater are in the legend.

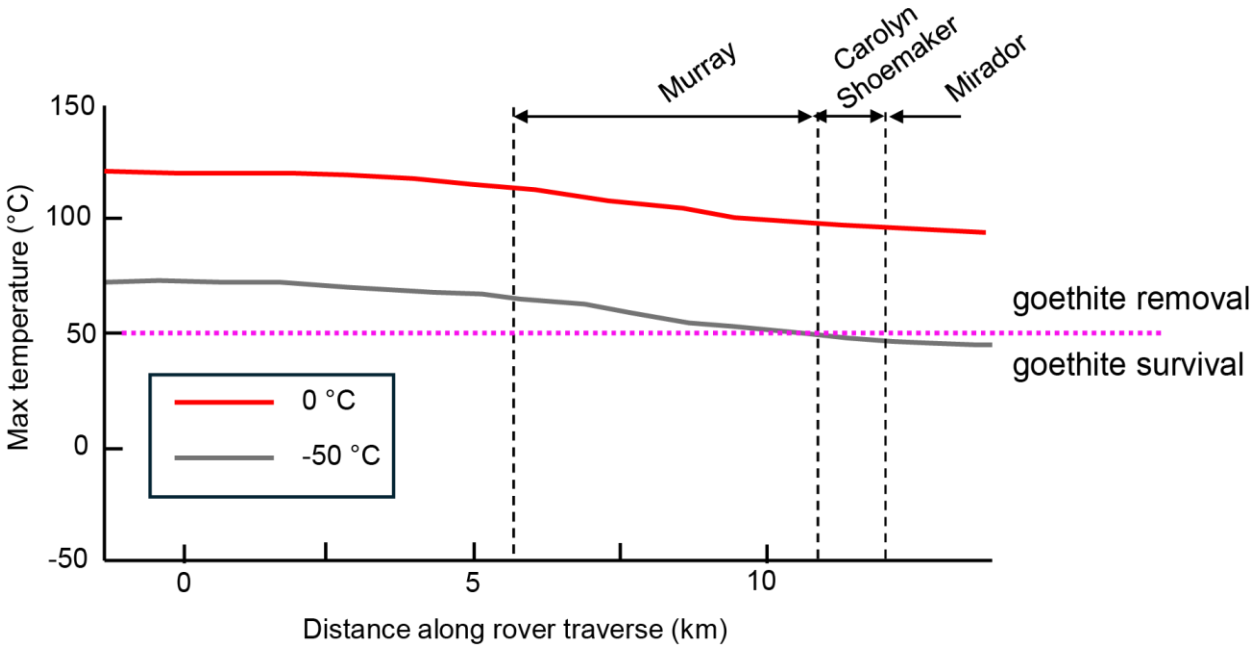

Fig. 5. Maximum burial temperatures experienced in Gale crater. Colored lines are results from previous thermal modelling of sedimentary rocks along the Curiosity traverse (*21*). The red line represents warm early Mars and the gray line represents present-day cold conditions (surface temperatures of 0 °C and -50 °C) (*9*). The pink dotted line at 50 °C marks the lowest temperature at which goethite transforms to hematite in the laboratory experiments (*9*). Vertical dotted lines are the boundaries between formations, labeled above. Under warm surface conditions, goethite would transform into hematite in all three formations, contrary to its detection in the Carolyn Shoemaker and Mirador formations. Under cold conditions, goethite remains stable above the Murray formation, in agreement with the rover data.

Acknowledgments: We acknowledge the support of the Jet Propulsion Laboratory engineering and management teams and Mars Science Laboratory science team members who participated in tactical and strategic operations, without whom the data presented here could not have been collected. M.S. acknowledges Jan Środoń, the leader of the grant under which the Earth samples were collected and analyzed.

Funding: M.S. acknowledges support from the Polish National Science Centre MAESTRO grant 2013/10/A/ST10/00050. T.S.P., E.B.R., D.W.M., R.V.M., S.J.R., N.C.H., B.S.K., V.M.T., and S.L.S. acknowledge NASA Internal Scientist Funding Model. T.F.B. acknowledges support for CheMin operations provided by NASA's Mars Exploration Program. B.M.T. acknowledges funding from the Canadian Space Agency, grant 22EXPMSLCA. E.M.H. acknowledges funding from MSL PS grant 80NSSC22K0656.

Author contributions:

Conceptualization: M.S., T.S.P., E.B.R.

Methodology: M.S., T.S.P.

Formal analysis: M.S., T.S.P.

Investigation: M.S., T.S.P., E.B.R., T.F.B., B.M.T., D.W.M., D.T.V., R.V.M., S.J.R., N.C.H., B.S.K., D.F.B., S.J.C., R.T.D., R.M.H., S.M.M., A.H.T., A.S.Y, V.M.T., M.T.T., C.N.A., D.J.D.M., J.P.G., N.C., P.C.C., E.M.H., S.L.S.

Writing-original draft: T.S.P.

Writing-review and editing: T.S.P., M.S., E.B.R., T.F.B., B.M.T., D.W.M., D.T.V., R.V.M., S.J.R., B.S.K.

Resources: M.S., T.S.P., E.B.R., R.V.M.

Competing interests: The authors declare that they have no competing interests.

Data and materials availability: The CheMin XRD data we analyzed are available in the Astrobiology Habitable Environment Database (AHED) repository (*10*). Laboratory synthesized hematite samples and hematite samples from Hawaii are stored at Amentum, NASA Johnson Space Center. All other Earth analog samples are stored at the Institute of Geological Sciences, Polish Academy of Sciences. The measured XRD patterns of these samples are provided in the AHED repository (*10*). The measured crystallographic parameters are listed in Table S1 for Gale crater and synthetic samples, and in Table S4 for the Earth analog samples. The measured abundances of hematite, goethite, akaganeite, jarosite, and phyllosilicates are available in the AHED repository (*10*).

Supplementary Materials

Materials and Methods
Supplementary Text
Figs. S1 to S36
Tables S1 to S8
References *(36-66)*

Science
AAAS

Supplementary Materials for

Hematite is a mineralogical marker of ancient climate change on Mars

Marek Szczerba[†], Tanya S. Peretyazhko[*†], Elizabeth B. Rampe, Thomas F. Bristow, Benjamin M. Tutolo, Douglas W. Ming, David T. Vaniman, Richard V. Morris, Silas J. Ralston, Nikole C. Haney, Bum Soo Kim, David F. Blake, Steve J. Chipera, Robert T. Downs, Robert M. Hazen, Shaunna M. Morrison, Allan H. Treiman, Albert S. Yen, Valerie M. Tu, Michael T. Thorpe, Cherie N. Achilles, David J. Des Marais, John P. Grotzinger, Nicholas Castle, Patricia C. Craig, Elisabeth M. Hausrath, Sarah L. Simpson

*Corresponding author. Email: tanya.peretyazhko@nasa.gov

[†]These authors contributed equally to this work

This PDF file includes:

Materials and Methods

CheMin analysis of Gale crater samples

CheMin analyzes a few tens of milligrams of drilled rock powder or scooped unconsolidated sediment. The XRD data are collected in transmission geometry from a cobalt source, with the angular range from ~5 to 52° 2 theta (2θ) and the angular resolution is 0.26 to 0.32° 2θ (increasing over the angular range) (*8*). The 2D XRD patterns are converted to 1D patterns using the GSE ver. 1.0 software (*36*). Rietveld refinement and full-pattern fitting of CheMin diffraction patterns provide quantitative mineralogy to a detection limit of ~1 wt.%, an estimation of X-ray amorphous content, and the unit-cell parameters of major crystalline phases.

Twenty samples analyzed by CheMin instrument with ≥1.5 wt.% hematite content were selected for detailed peak analysis. The samples included Confidence Hills (CH), Mojave2 (MJ), Oudam (OU), Marimba (MB), Quela (QL), Sebina (SB), Duluth (DU), Stoer (ST), Highfield (HF), Rock Hall (RH), Glen Etive2 (GE2), Glasgow (GG), Hutton (HU), Nontron (NT), Bardou (BD), Pontours (PT), Maria Gordon (MG), Zechstein (ZE), Avanavero (AV), and Canaima (CA). Although Aberlady (AL) contained 1.7 wt.% hematite, it was excluded from the analysis because overlap of hematite (104) peak with a bassanite peak introduced large errors in evaluating crystallinity.

Modeling CheMin XRD patterns

Crystallite sizes were determined by fitting the peak shapes of hematite in XRD patterns, and these are generally equal to or smaller than the grain or particle sizes (*37*). In Gale crater, hematite is described as “gray” or “red” (*26, 38*). These terms reflect differences in grain size rather than crystallite size. Gray hematite consists of coarser grains (>5 μm; HF and OU samples), whereas red hematite forms aggregates of fine grains (~5 μm; other samples) (*26, 38*). XRD-derived crystallite sizes can be similar for both types. Therefore, XRD data alone cannot distinguish red from gray hematite, as both are aggregates of hematite crystallites with comparable structural characteristics.

Beside crystallite size, lattice imperfections and instrument broadening contribute to the width of XRD peaks. To calculate instrumental contributions, a diffractogram of the quartz-beryl 3:97 standard (measured on sol 740) was fitted with a model of contributions from the Co X-ray source spectrum, receiving slit size, and tube beam spot size for exact primary and secondary goniometer radii (Fig. S4). Full width at half maximum (FWHM) dependence on 2θ angle was then tuned by addition of Gaussian and top-hat convolutions as functions of 2θ angle. All further analyses were performed with fixed instrumental contribution, using the optimized values from this procedure.

Lattice imperfections, such as vacancies, substitutions or other defects that displace atoms from ideal positions, can result in size variance of diffracting domains, a phenomenon referred to as microstrain broadening. The microstrain effects can be also anisotropic but are dependent on reflection order. In the case of the data from CheMin instrument, there are only four hematite peaks available in the measured 2θ range, which are also overlapping with reflections of other minerals. Therefore, broadening was accounted for by the size broadening effect only, although contribution from microstrain cannot be excluded.

The CheMin instrument places limits on the range of crystallite sizes that can be determined compared with conventional laboratory instruments, because there is a substantial peak broadening caused mainly by small size of the diffractometer. The upper limit of evaluation of crystallite sizes is therefore about 100 nm for the CheMin instrument, compared to ~1 μm for laboratory instruments. For crystallite sizes bigger than the limit, the uncertainties are larger than the measured sizes.

All phases identified by CheMin instrument in the studied samples were included in XRD fitting and peak analysis, to account for possible hematite peak overlaps with other mineral phases. Refinements were performed by fitting a polynomial background (Chebyschev 5th order) to account for amorphous phase contributions, which can be non-negligible at hematite peak positions. Optimizations were performed in range 25 to 51^{o} 2θ to focus on peaks belonging to hematite. In most cases hematite was allowed to have preferred orientation, while for other mineral phases random orientation was considered. The only exception was Mojave2 sample, in which hematite (110) peak is overlapping with intense plagioclase peak, and thus random orientation of hematite was used.

Two methods of whole powder pattern modelling (WPPM) were performed in TOPAS ver. 5 software:

1) WPPM with independent fitting of mean sizes of crystallites for four major hematite peaks ((012), (104), (110), (113)), using double-Voigt convolutions (*39*) with Lorentz function broadening for crystallite sizes (Fig. S5-S24, Table S1). Additionally, the unit cell a and c parameters were optimized by the software (Fig. S25, Table S1).
2) WPPM method with log-normal distribution of crystallite sizes (*40*), with two optimized parameters μ (mean) and σ (variance) (Fig. S5-S24):

$$f(x) = \frac{1}{\sqrt{2\pi}\sigma x} e\left(-\frac{(\ln x - \mu)^2}{2\sigma^2}\right) \quad \text{(S1)}$$

The obtained μ and σ parameters for the studied samples were compared in Fig. 3 with theoretical paths for different growth mechanisms. Table S2 presents μ and σ^2 values together with their estimated uncertainties.

Synthetic hematite samples

XRD data for synthetic hematite samples were analyzed using the same methodology as XRD data from Gale crater. The following samples were shown in Fig. 2C (samples from the previous work (*22*-*25*)) and Fig. 2D (samples synthesized for this study):

i) Hematite formed by forced hydrolysis (90 ^{o}C, 24 hrs.) of 0.1 M $Fe(ClO_4)_3$ at initial pH 1.6 and 2 in the presence of 0.01 to 0.1 M NaCl. pH 2 was adjusted by 0.1 M NaOH (*22*). The resulting XRD patterns for 7 samples are shown in Fig. S26-S27.

ii) Hematite formed by crystallization of ferrihydrite precipitated by hydrolysis (90 ^{o}C, 24 hrs.) of 0.1 M $Fe(ClO_4)_3$ at initial pH 8 adjusted by 0.1 M NaOH in the presence of 0.02 to 0.1 M NaCl (*22*). The resulting XRD patterns for 3 samples are shown in Fig. S28.

iii) Hematite formed by crystallization of ferrihydrite precipitated by hydrolysis (90 ^{o}C, 5 hrs.) of 0.2 M $FeCl_3$ at initial pH 4 adjusted by 16 M NaOH (*23*). The resulting XRD pattern for 1 sample is shown in Fig. S29.

iv) Hematite formed by crystallization of ferrihydrite precipitated by hydrolysis (80 ºC, 24 hrs.) of solutions leached from Falconbridge and Santa Elualia pyrrhotite natural samples at initial pH 3 and 4. Solution leached from Falconbridge pyrrhotite contained 20.5 mM Fe(II), 2 mM SO_4^{2-}, 1.2 mM Mg, 2.6 mM Al, and 1.7 mM Si. Solution leached from Santa Elualia pyrrhotite contained 20.6 mM Fe(II), 2.7 mM SO_4^{2-}, 0.08 mM Mg, 0.03 mM Al, and 0.23 mM Si. Iron(II) was oxidized by addition of H_2O_2 (*24*). The resulting XRD patterns for 3 samples are shown in Fig. S30.

v) Hematite formed through oxidation and hydrolysis of Fe(II) released from Stapafell basaltic glass in flow-through experiments (0.25 ml min^{-1} flow rate, 6 days) with inflow H_2SO_4 solution of initial pH 2 and 3, at 200 ºC (*25*). The resulting XRD patterns for 2 samples are shown in Fig. S31.

vi) Hematite formed by thermal alteration of synthetic goethite, akageneite and ferrihydrite heated at 250, 300, 450, and 850 ºC for 2 hrs. at each temperature. In addition, ferrihydrite and goethite samples were heated at 100 ºC up to 4 months (Fig. S32-S34). Fig. S33 also shows the XRD data for hematite formed after 3-year storage of ferrihydrite at 17 °C and 65 % relative humidity (*29*). Ferrihydrite was prepared by grinding a mixture of 20 g $Fe(NO_3)_3 \cdot 9H_2O$ and 12 g NH_4HCO_3 (1.7:1 mass ratio) for 15 min until CO_2 bubbling ceased and brown precipitate formed (*41*). Akaganeite was prepared by hydrolysis (80 ºC, 5 hrs.) of 0.2 M $FeCl_3$ (*42*). Goethite was synthesized by hydrolysis (70 ºC, 60 hrs.) of solution prepared by mixing together 20 ml 1 M $Fe(NO_3)_3$ and 36 ml 5 M KOH and diluting to 400 ml with deionized water (*43*).

X-ray diffraction analysis of samples i) to iii) was performed using a Panalytical X'Pert Pro instrument equipped with Co Kα radiation at 45 kV and 40 mA, 0.02° 2θ step size, and 1-min counting rate. Analyses were done with programmable divergent and antiscatter slits set to 1/4° and 1/2°, respectively. The other samples were analyzed using a Rigaku MiniFlex benchtop 600 X-ray diffractometer with Co Kα radiation at 15 kV and 40 mA, 0.02° 2θ step size counted for 10 s. Lanthanum hexaboride standard (NIST 660a LaB_6 (*44*)) was used to determine instrument line broadening for both instruments.

Earth hematite samples

83 samples from the Ediacaran redbeds, paleosols, and hydrothermally altered basalt and tuffs of the East European Craton, representing wide range of origin and diagenetic conditions was analyzed using WPPM with independent fitting of mean sizes of crystallites for four hematite peaks (Fig. S35, Tables S3 and S4 – results for the two most intense peaks, (104) and (110), are presented). 10 non-Ediacaran sedimentary rocks of different ages, diagenetic conditions, and from different localities were also analyzed (*4*). Maximum paleotemperatures were determined using illite-smectite paleothermometry from the previously determined experimental relationship between the percentage of smectite in illite-smectite and the temperature in several wells of the East Slovak Basin (*45*). Seven volcanic hydrothermal gray hematite (*46*) and 5 red hematite samples from Maunakea, Hawaii were also analyzed (Tables S3 and S4).

The volcanic gray and red hematite samples were analyzed using Panalytical X'Pert Pro and Rigaku MiniFlex, respectively, in the same way as the synthetic hematite samples. All other samples were measured using Thermo ARL X'tra diffractometer, equipped with copper (Cu) lamp, at 40 kV and 35 mA. Diffractograms were recorded in the range of 5 to 65° 2θ at 5-s counting rate and 0.02° 2θ step size. Instrumental contributions to peak shapes were calculated by fitting of lanthanum hexaboride standard (NIST 660a LaB_6) (*44*).

Calculations of Ostwald ripening time

The time required for a crystallite to grow by Ostwald ripening is (*34*):

$$R_m(t)^3 - R_m(0)^3 = Kt \quad \text{(S2)}$$

$$K = (8D_{eff}\gamma v^2 C_{eff\infty})/(9RT) \quad \text{(S3)}$$

where t is the time, R_m is the mean radius, D_{eff} is the effective bulk diffusion coefficient in rock, γ is the interfacial energy, v is the molar volume, $C_{eff\infty}$ is the effective concentration of component of dispersed phase in rock, T is the temperature, R is the gas constant. Effective concentration is related to equilibrium concentration ($C_{eq\infty}$) by the equation:

$$C_{eff\infty} = \phi C_{eq\infty} \quad \text{(S4)}$$

where ϕ is the water/rock ratio.

Following previous methods (*34*), we first calculated the solubility of hematite as a sum of all dissolved Fe(III) species at pH 2 to 7 using Geochemist's Workbench 2023. Hematite solubility was calculated in solutions containing 2.6 mol kg^{-1} dissolved chloride (Cl^-), 0.33 mol kg^{-1} dissolved sulfate (SO_4^{2-}), and in a chloride- and sulfate-free solution (denoted as an anion-free solution). Chloride and sulfate were included because the formation of anion-bearing complexes with Fe(III) enhances solubility of Fe(III) oxide and oxyhydroxide (*3*) and, consequently, accelerates Ostwald ripening. The Cl^- and SO_4^{2-} concentrations correspond to the upper limit of the anion content in the final groundwater that interacted with the rocks of the Murray formation (*47*). The solubility was multiplied by ϕ ratio of 0.01 (*34*) to obtain the effective Fe concentration in rock and divided by 2 (2 moles of Fe in 1 mole hematite) to calculate the effective equilibrium concentration of hematite at pH 2 to 7, 50 °C. The results are summarized in Table S5.

To address the effect of interfacial energy on ripening kinetics, we performed calculations using interfacial energy values reported for bulk hematite (γ_1) and nanoparticles (γ_2). Calculations were performed to determine the time required for a crystallite to grow from the size of crystallites in Duluth sample (the smallest size in Murray formation) to the size of crystallites in Confidence Hills (the largest size in Murray formation). The parameters used in equations S2 and S3 are listed in Table S6.

The results of Ostwald ripening time calculations are summarized in Table S7 and shown in Fig. S36. The calculated time differed up to eight orders of magnitude between pH 7 and 2. The timescale of Ostwald ripening at pH 7 was close to the upper limit of water duration episodes (~1 million years (Ma)) when Mars transitioned to dry climate conditions (*48, 49*). Chloride and sulfate accelerate Ostwald ripening under acidic conditions because of increased hematite solubility caused by Fe(III) complexation with the anions. The time remained about the same at neutral pH for an anion-free solution and for solutions containing chloride or sulfate because Fe(III) complexes with hydroxyl ions dominated this pH range (*3*). The calculated time reflects the total period of water presence, which could happen in multiple wet episodes or a single continuous interval.

Supplementary Texts

Acidic hematite formation

We compared hematite crystallite size and morphology observed in Gale crater with the hematite formed under acidic conditions through hydrothermal alteration of basaltic glass, forced hydrolysis of Fe(III) solutions, and acidic ferrihydrite alteration.

Synthetic hematite formed through hydrothermal alteration of basaltic glass at pH 2 to 3 has crystallites of platy morphology not observed in Gale crater (Fig. 2C). Hematite crystallites formed in solution at elevated temperatures (80 to 90 ºC) via forced acidic hydrolysis (pH 1.6 to 2) and ferrihydrite alteration (pH 3 to 4) (Fig. 2C) were of equant shape and within a range 10 to 30 nm. They are larger than hematite crystallites from the Carolyn Shoemaker and Mirador formations but similar to intermediate sizes from the Murray formation. The conditions of forced hydrolysis correspond to extreme environments like fumaroles and acidic lakes (*50*) and would destroy primary minerals and phyllosilicates (*51*). The presence of abundant plagioclase, pyroxene, and smectite in the drilled samples (*7*) suggests that they were not subject to extremely acidic conditions. Acidic ferrihydrite alteration corresponds to moderately acidic environments that existed in the Murray formation based on the presence of jarosite in some drill targets (Fig. 1B). However, the dominance of Fe(III) sulfate aqueous complexes in the pH range where jarosite forms (pH<4, (*52*)) would suppress ferrihydrite formation together with jarosite and/or alteration of pre-existing ferrihydrite into hematite (*23*). Jarosite in the Murray formation is a late-stage diagenetic product formed ~2.1 Ga ago during the Amazonian period (*18*). Younger formation of ferrihydrite would require jarosite dissolution (*37*), followed by ferrihydrite alteration to hematite, which was unlikely to happen during the Amazonian when liquid water, e.g., related to local melting of ice deposits, would have only been transiently present (*53*). We therefore conclude that formation of hematite under acidic conditions was unlikely in Gale crater.

Ferrihydrite to hematite via goethite intermediate

Experimental studies show that the formation of hematite from ferrihydrite is a two-stage reaction with a goethite intermediate involved at elevated temperatures under aqueous, neutral to alkaline conditions (*32, 33, 54*). Previous work (*32*) investigated the alteration of ferrihydrite to goethite and hematite at pH 2, 7, and 10 in a temperature range from 25 to 100 °C. Their X-ray diffraction analysis indicated that hematite and goethite formed from ferrihydrite simultaneously at pH 10 and 50 °C. Sample analyses at >7d reaction duration showed a decrease in goethite content accompanied by increasing hematite abundance. Other experiments (*33*) have expanded the pH range at which goethite-to-hematite transformation occurred. The transformation of ferrihydrite at pH 7, 10, and 12 at 60 °C leads to the formation of hematite and goethite (*33*). The goethite content approached the maximum after a 10 to 20 d reaction and then decreased. At the same time, the hematite content increased.

Based on these studies, we propose 50 °C as the lowest temperature of goethite transformation into hematite, which can occur in the pH range from pH 7 to 12. In the previous experiments, the transformation at 50 °C occurred over approximately 20 days (*32*), suggesting that a similar transformation can occur at lower temperatures given sufficient time. Because diagenesis in Gale crater likely occurred on ~Ma timescales at near-neutral pH (Table S7), the transformation of goethite to hematite could plausibly have occurred at lower temperatures, though with slower kinetics. While the experiments at 50 °C provide constraints on timescales of transformation, this mechanism of hematite formation has not been explicitly investigated under ancient Mars conditions.

The previously proposed reaction mechanism (*32, 33*) is a two-stage crystallization mechanism of hematite from ferrihydrite, with goethite as an intermediate product. This mechanism is similar to goethite - hematite transformation in alkaline solutions observed at ≥ 150 °C (*55, 56*). Hematite particles have been observed to grow on goethite crystals (*55*). Such spatial association and the lack of ferrihydrite indicate that hematite formed directly from goethite by dissolution-precipitation mechanism.

Burial temperatures along the Curiosity traverse

FIG. 5 shows the maximum temperatures buried rocks could experience along the Curiosity traverse, calculated by previous thermal modelling [(*21*), their figure 8]. The modeled path covered the *Curiosity* traverse completed from the near-landing site to the beginning of the Murray formation at the Puhrump Hills region (*16*) and then predicted future pathway beyond that point (*21*). Their predicted path went through the hematite ridge region within the Murray formation (~10 km mark in FIG. 5, [(*21*), their figure 8], later renamed as Vera Rubin Ridge (*57*). However it did not cover the locations of the Murray, Carolyn Shoemaker, and Mirador formations. To place the formation locations along the Curiosity pathway, we used their calculated traverse distance as a function of elevation [(*21*), their figure 4B]. From the elevations of the beginning of the Murray formation, the boundary between Murray to Carolyn Shoemaker, and the boundary between Carolyn Shoemaker to Mirador, we extracted the corresponding traverse distances listed in Table S8 and plotted in FIG. 5.

The thermal model (*21*) considered two evolutionary scenarios: a complete fill of Gale crater followed by partial erosion (scenario 1) and a partial fill controlled by slope wind (scenario 2). Scenario 1 calculations for the present-day cold surface conditions show the burial temperature transitioned from >50 °C to < 50 °C near the end of the Murray formation. In contrast, the thermal evolution of scenario 2 shows temperatures <50 °C in the Murray formation, which would preserve goethite, contrary to rover data. We therefore adopt scenario 1 in FIG. 5.

Figures

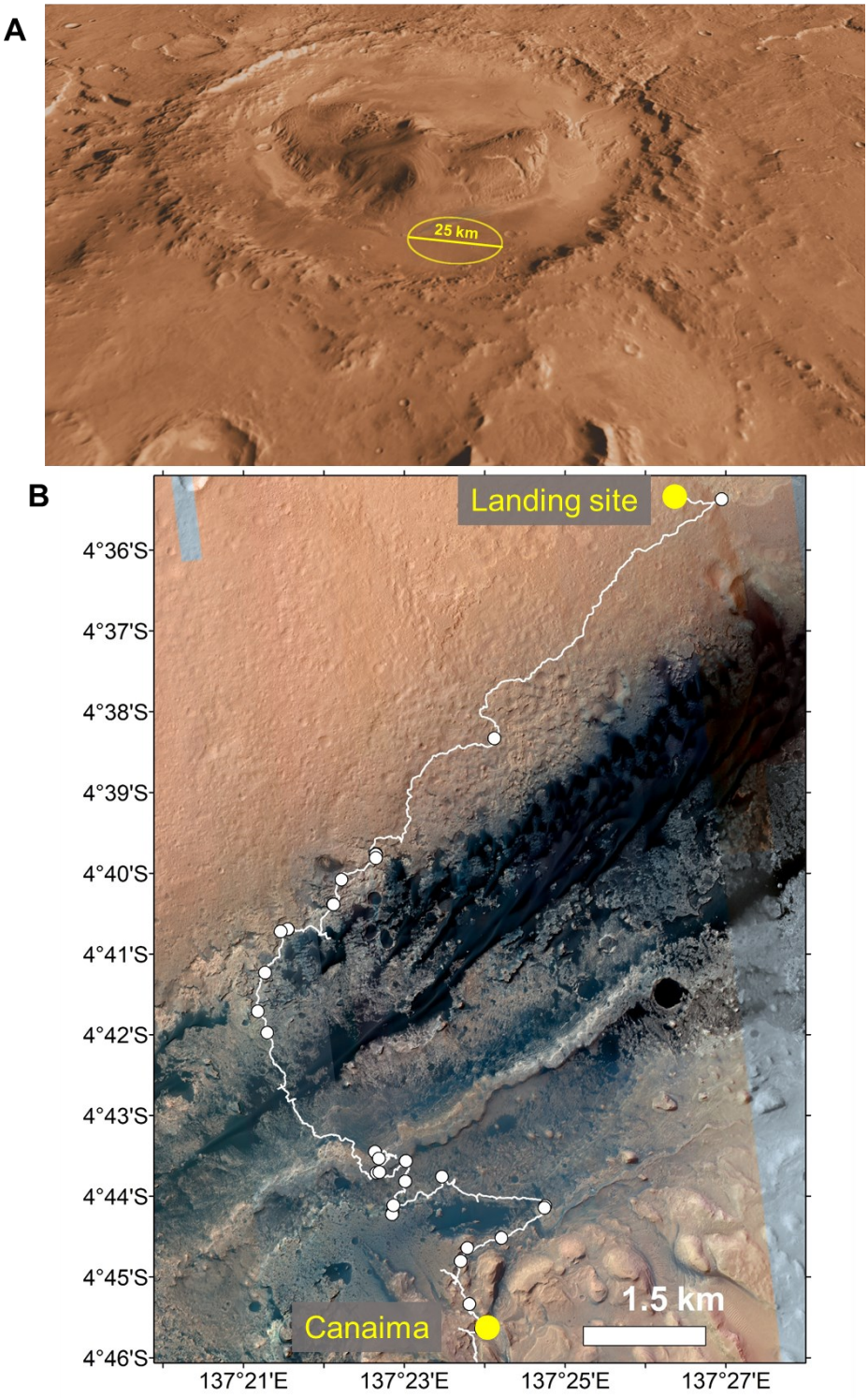

Fig. S1. Gale crater on Mars. (A) The southward-looking orbital view of the crater with the landing area marked by a 25-km yellow ellipse (*58*). The actual landing site is 2.39 km from the ellipse center (*59*). (B) Rover traverse (white line) from the landing site to Canaima (yellow circles) over a color mosaic of High Resolution Imaging Science Experiment (HiRISE) images (*60*). The white circles show locations of drill targets.

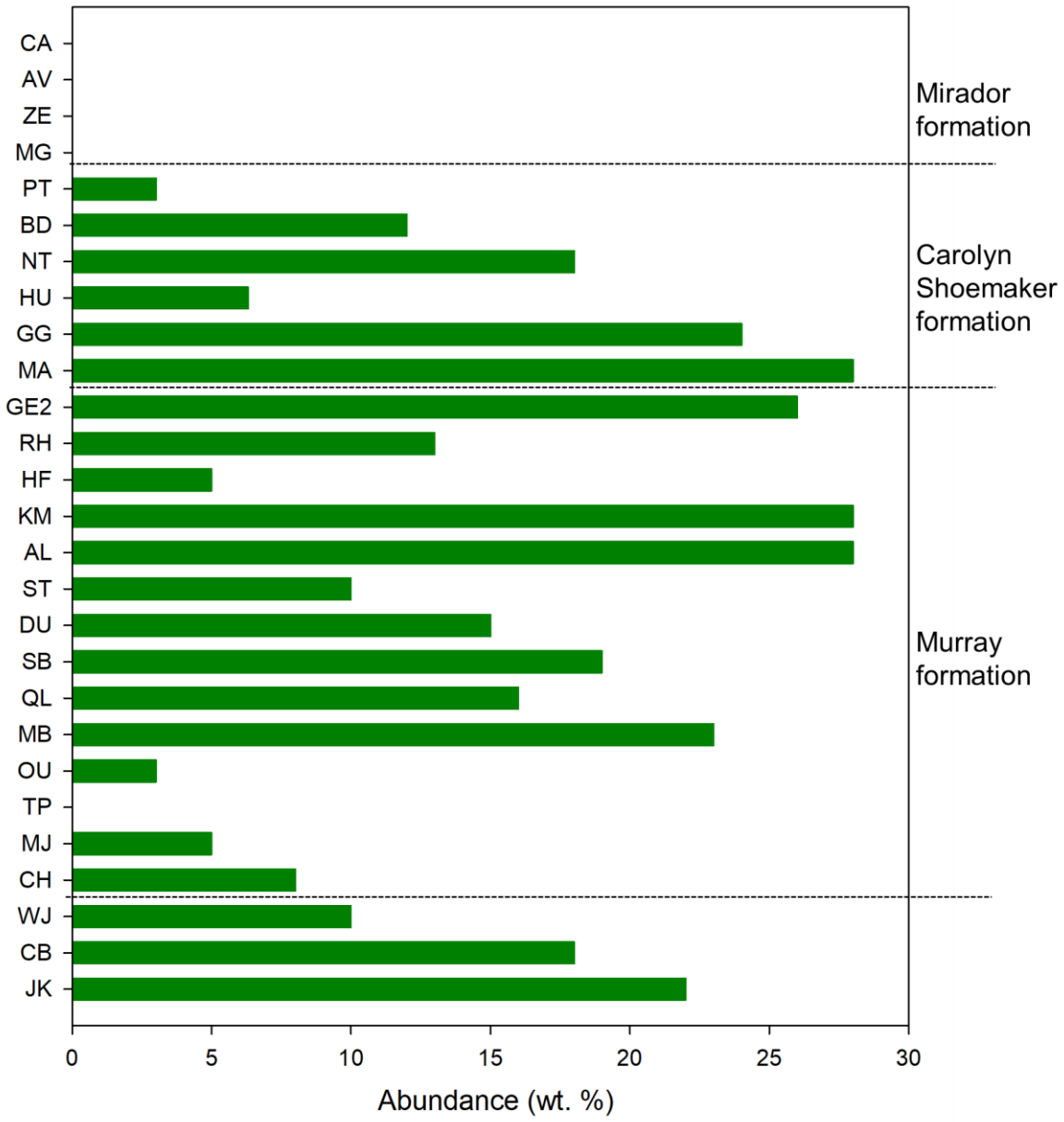

Fig. S2. Phyllosilicate abundances in Gale crater samples. Abbreviated sample names are shown, and abundances are indicated by dark green bars. Smectite is the dominant phyllosilicate mineral in all samples (*7, 17*). Abundant phyllosilicates are present in the samples from the Murray and Carolyn Shoemaker formations but are not detected in the Mirador formation. Abundances are reported in the AHED repository (*10*). Dotted black lines mark the boundaries of the Murray, Carolyn Shoemaker and Mirador formations.

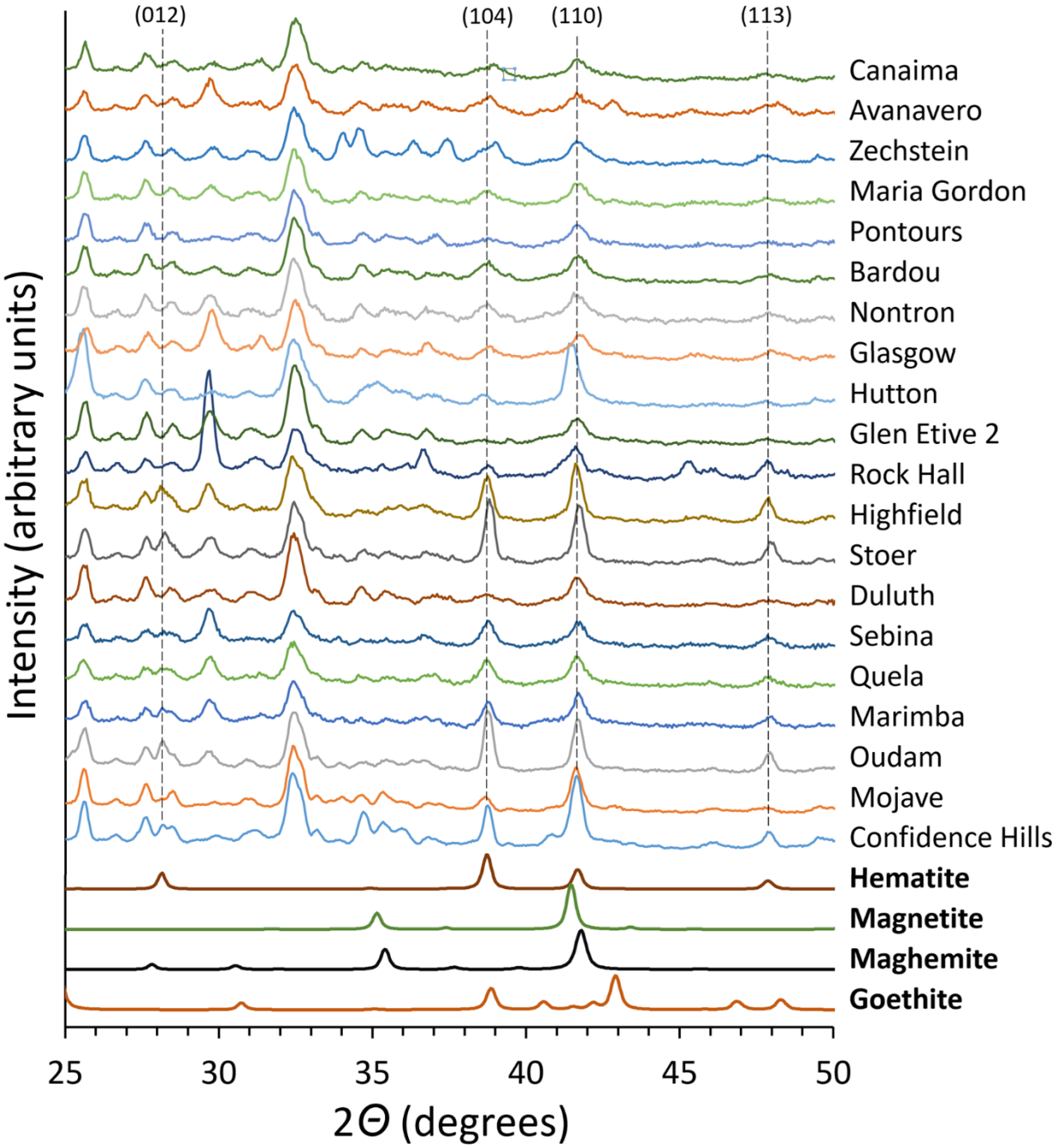

Fig. S3. Comparison of X-ray diffraction patterns measured by the CheMin instrument (thin solid lines) with calculated reference patterns of major iron oxide and oxyhydroxide phases (thick solid lines). Vertical dashed lines indicate four main hematite peaks. The XRD patterns are available in the AHED repository (*10*).

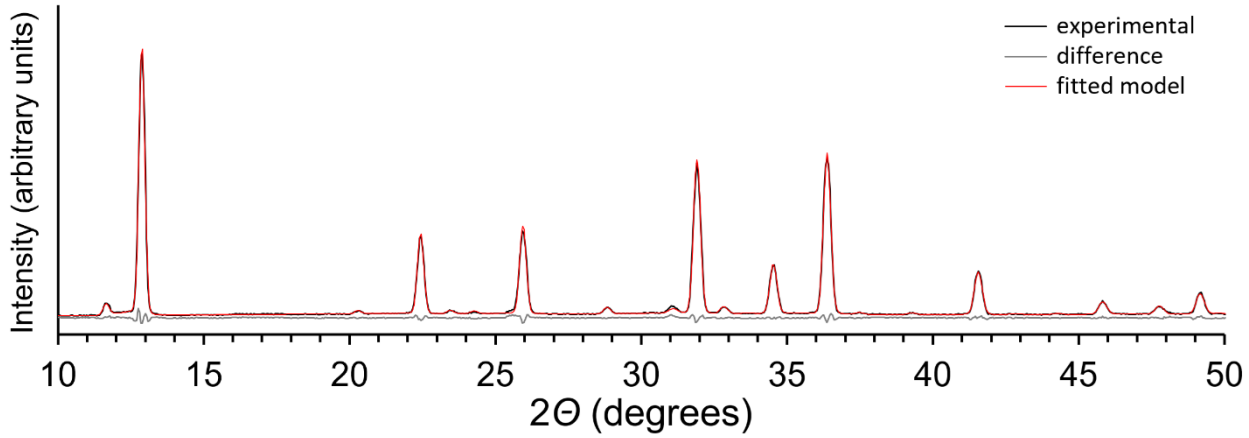

Fig. S4. Comparison of measured diffractogram (Co Kα source) of quartz-beryl 3:97 standard (black line), model (thin red line), and difference curve (grey line).

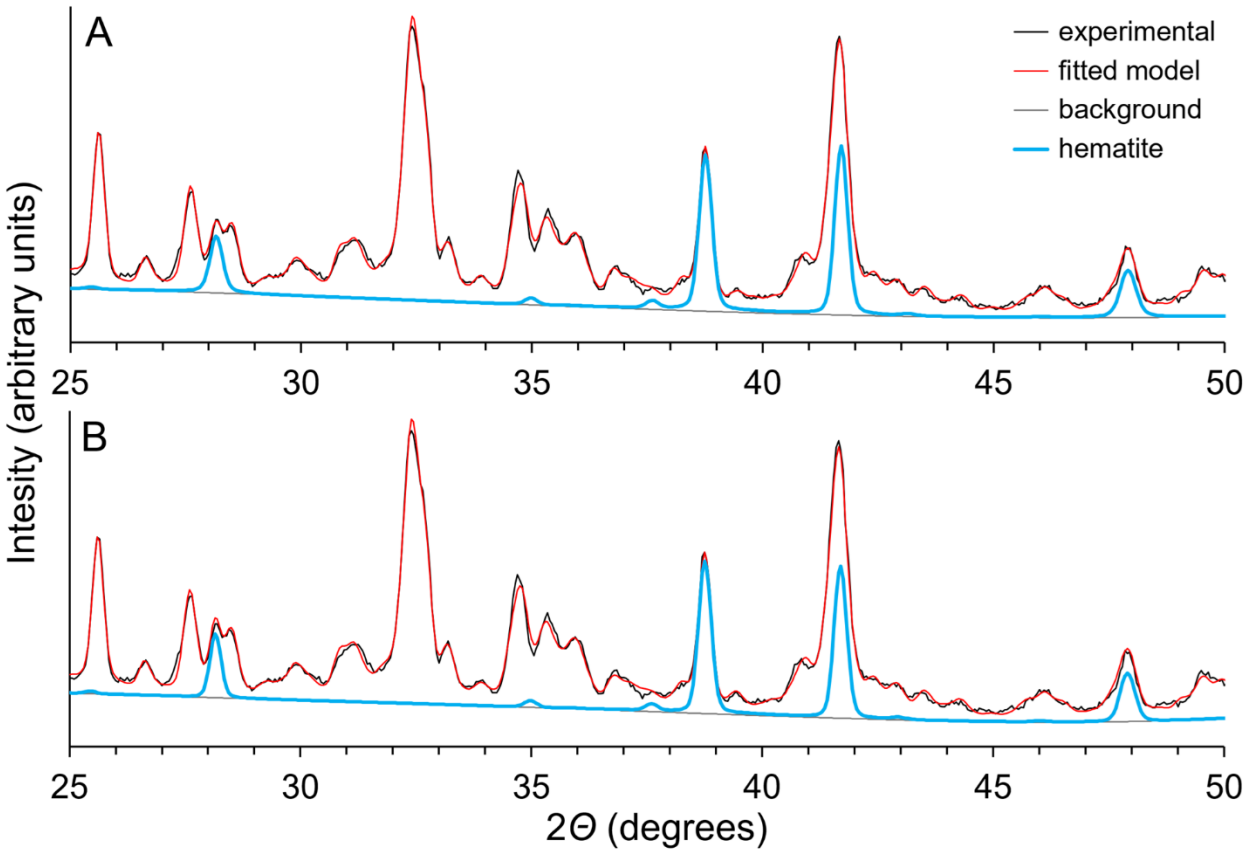

Fig. S5. Comparison of measured diffractograms (Co Kα source) of Confidence Hills (black line), and models fitted to the data (red line). Hematite peaks are shown as thick blue line, while background as grey line. (A) Model with independent fitting of mean sizes of crystallites for the four most intense hematite peaks. (B) Model assuming a log-normal distribution of crystallite sizes for four hematite peaks.

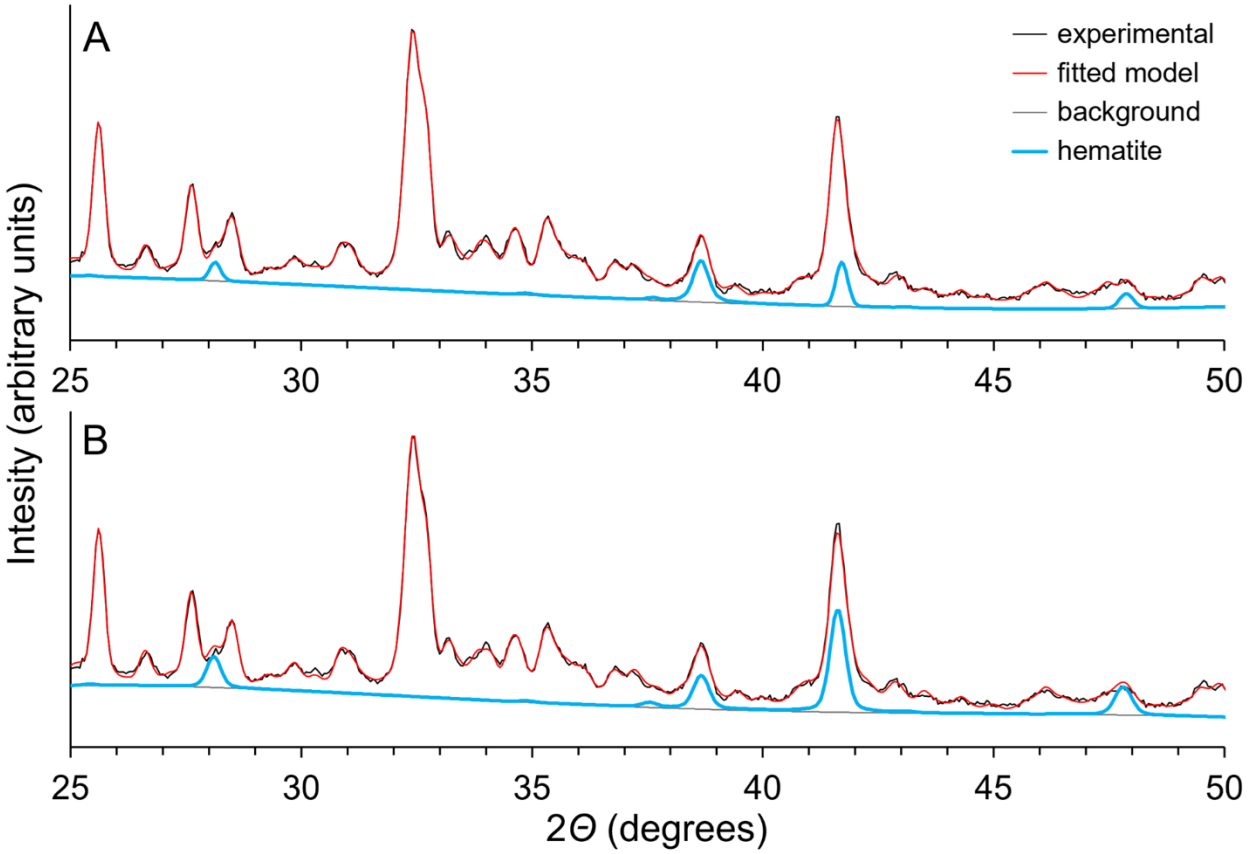

Fig. S6. Same as Fig. S5 but for Mojave2.

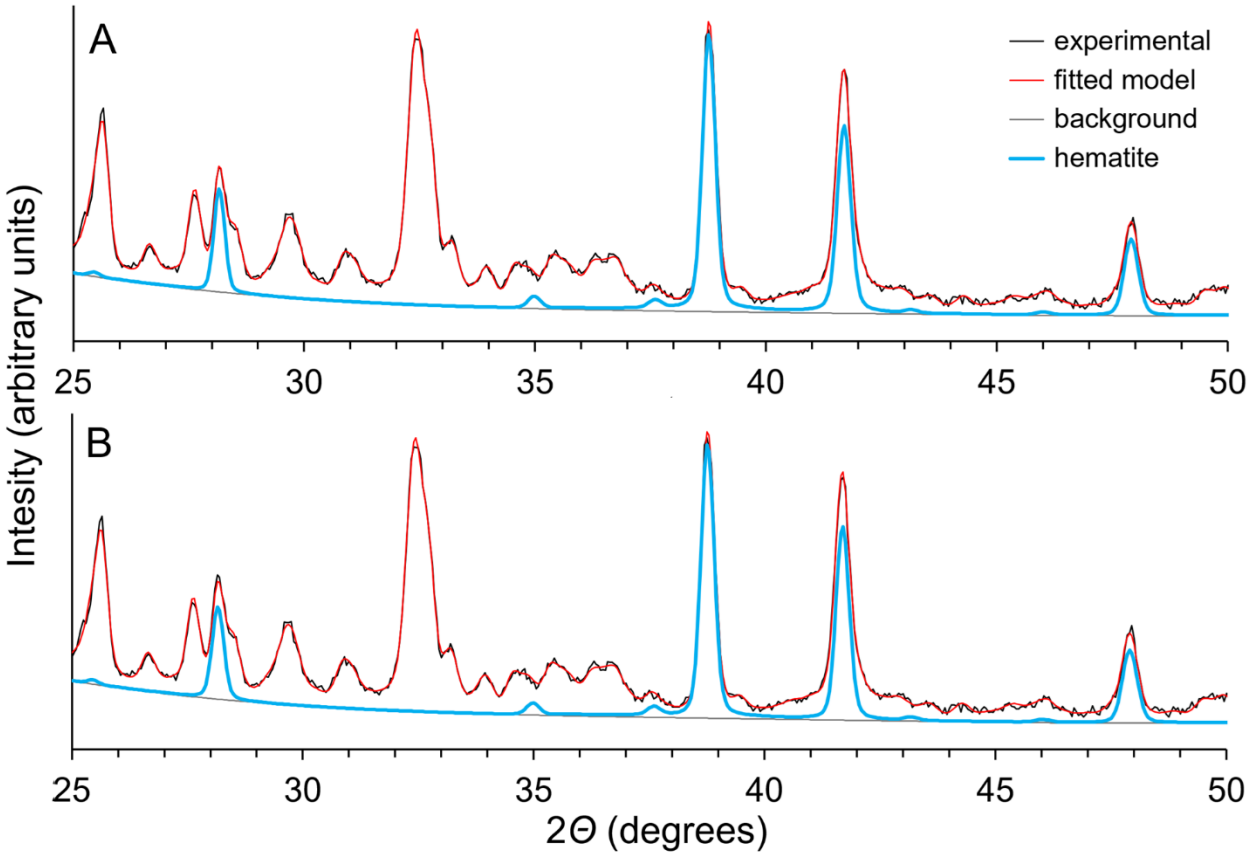

Fig. S7. Same as Fig. S5 but for Oudam.

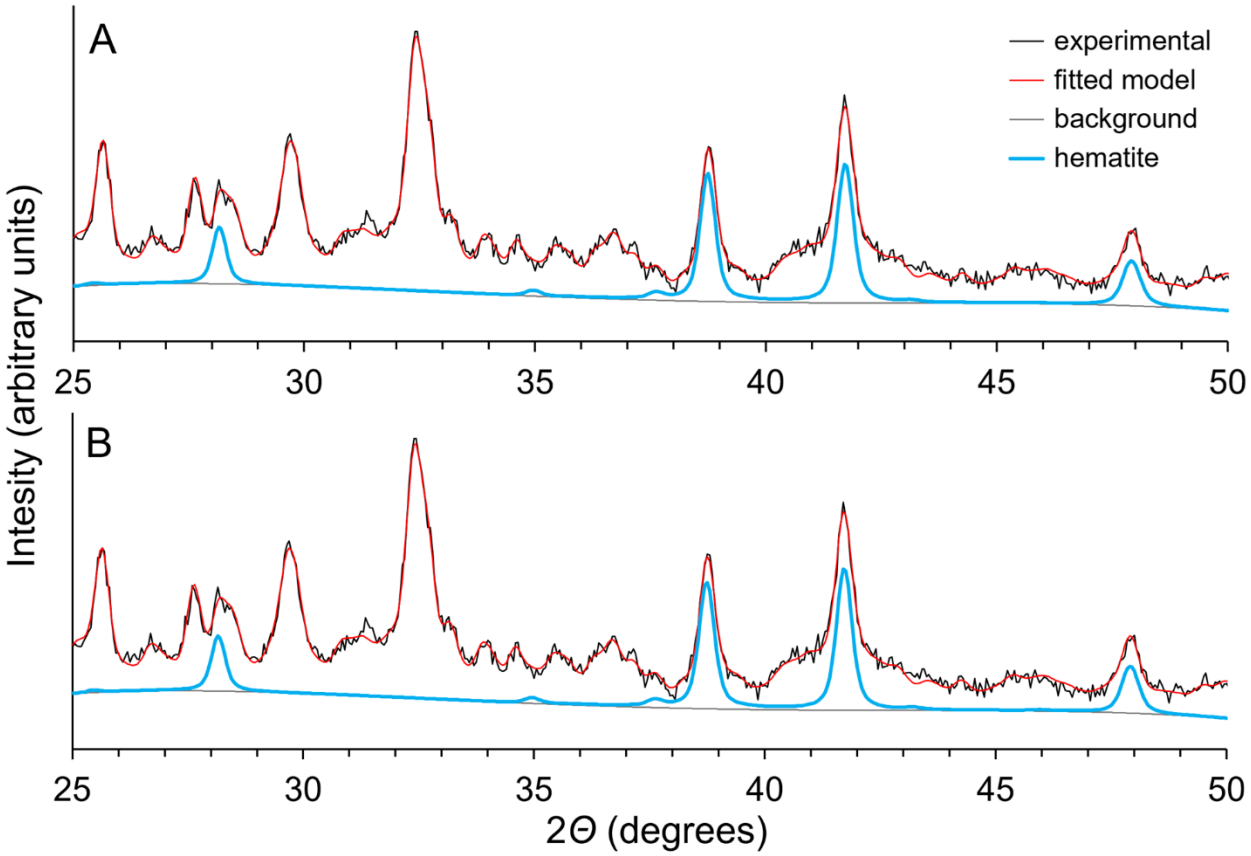

Fig. S8. Same as Fig. S5 but for Marimba.

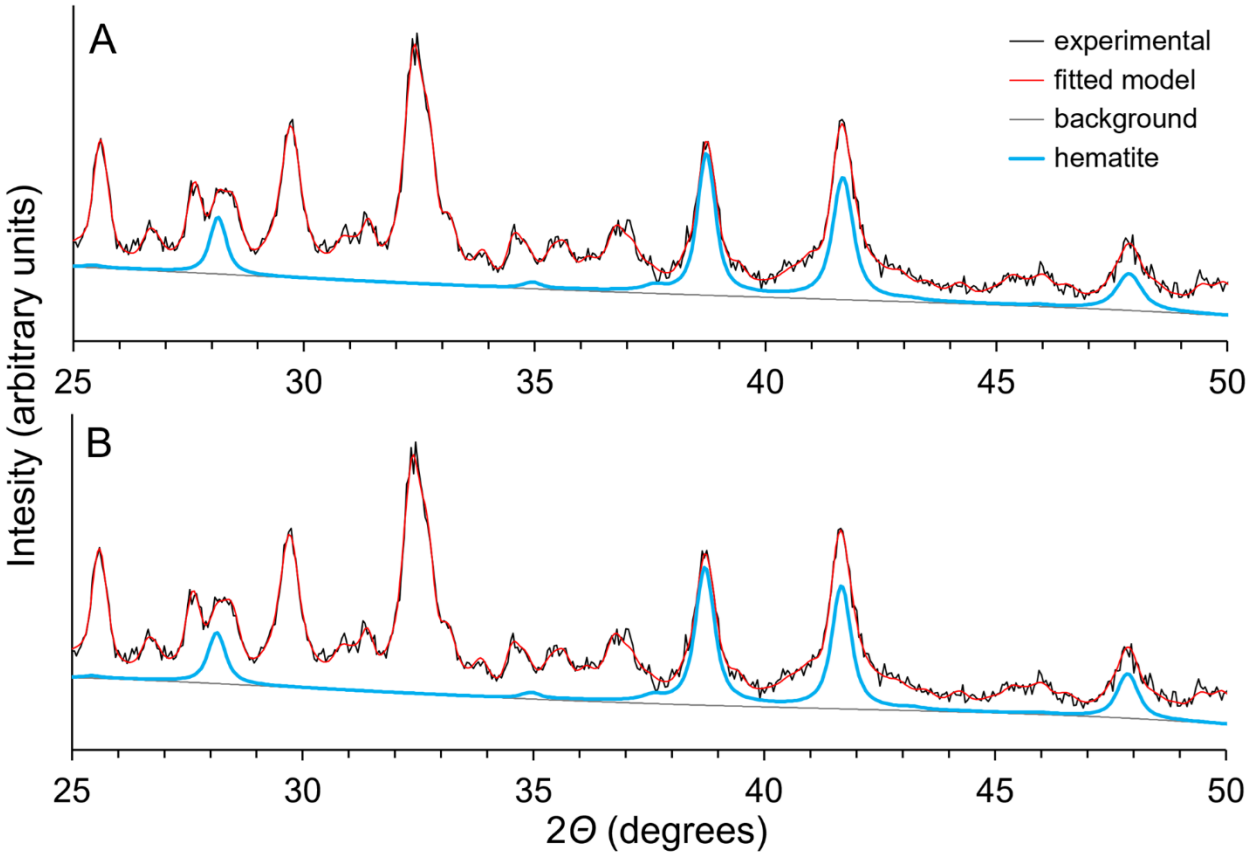

Fig. S9. Same as Fig. S5 but for Quela.

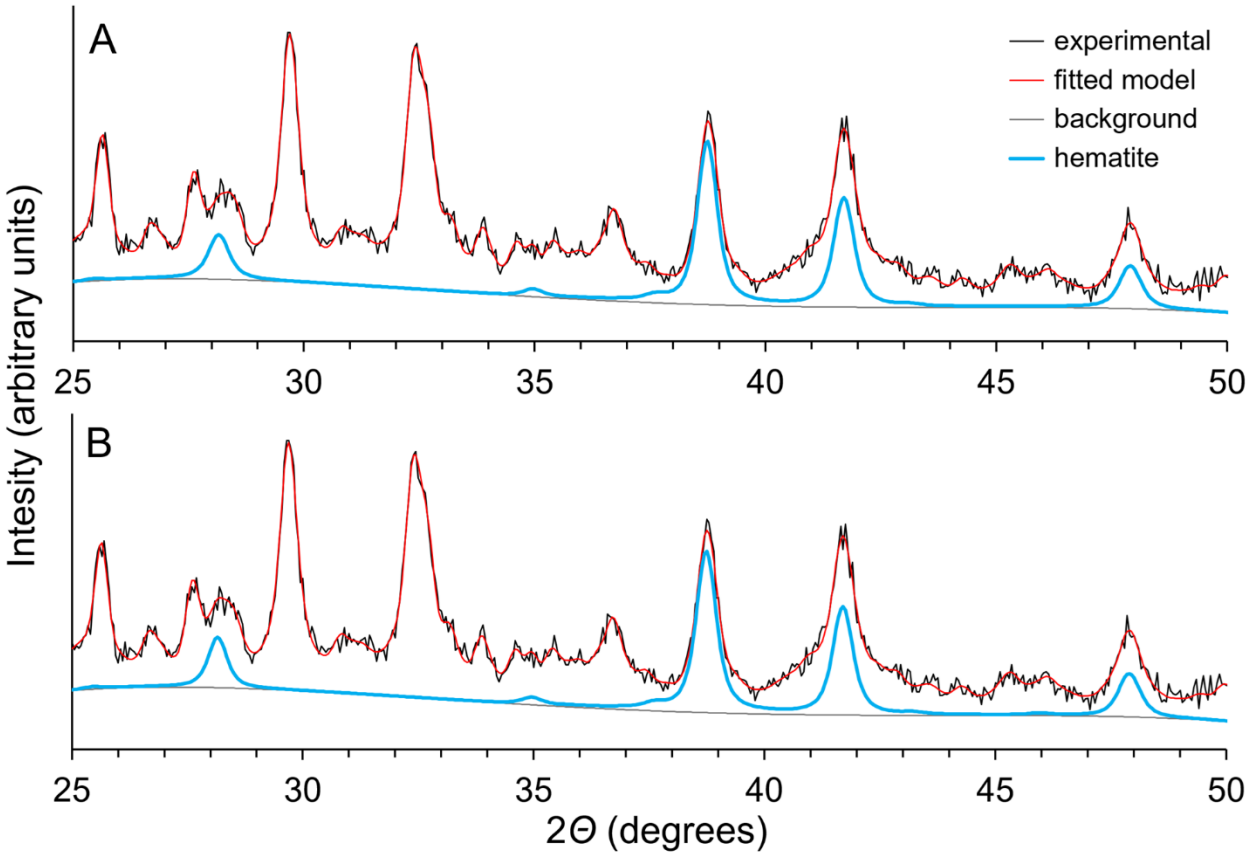

Fig. S10. Same as Fig. S5 but for Sebina.

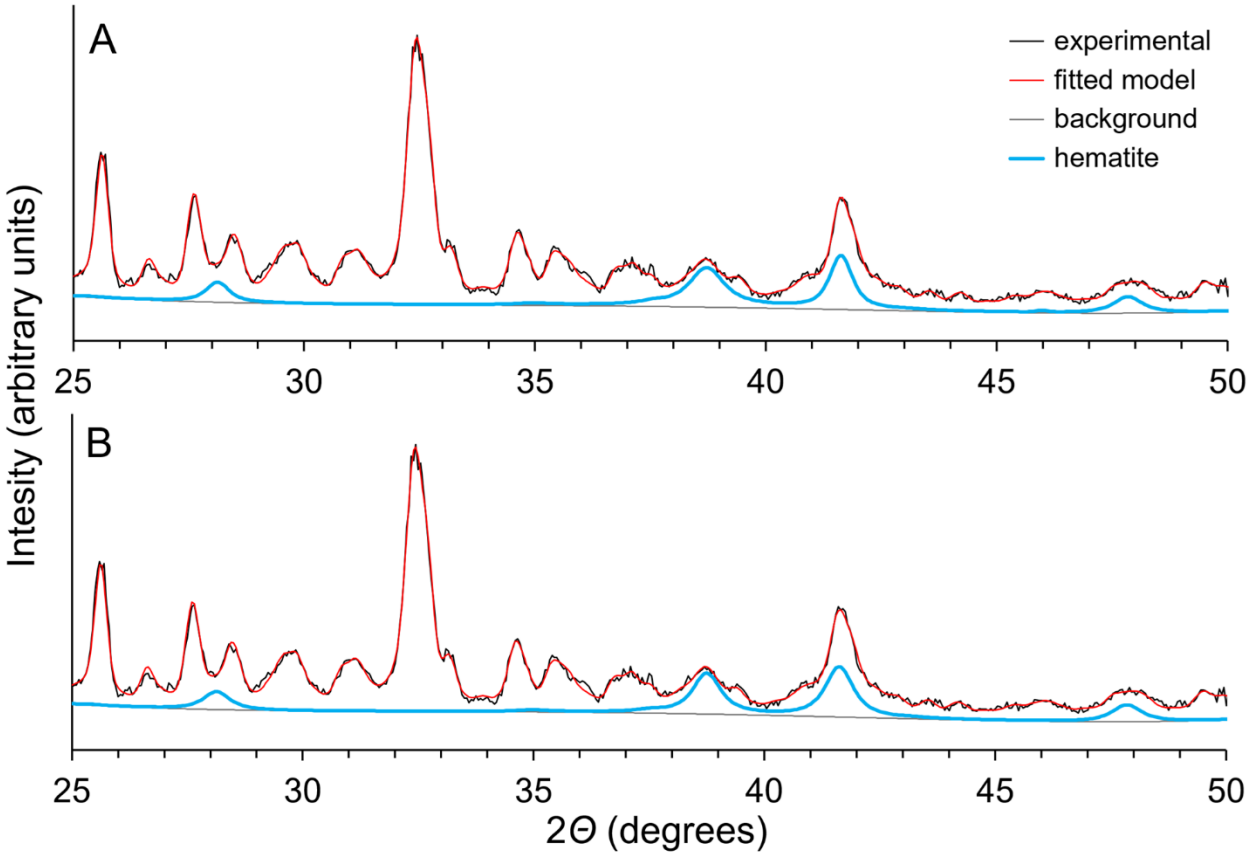

Fig. S11. Same as Fig. S5 but for Duluth.

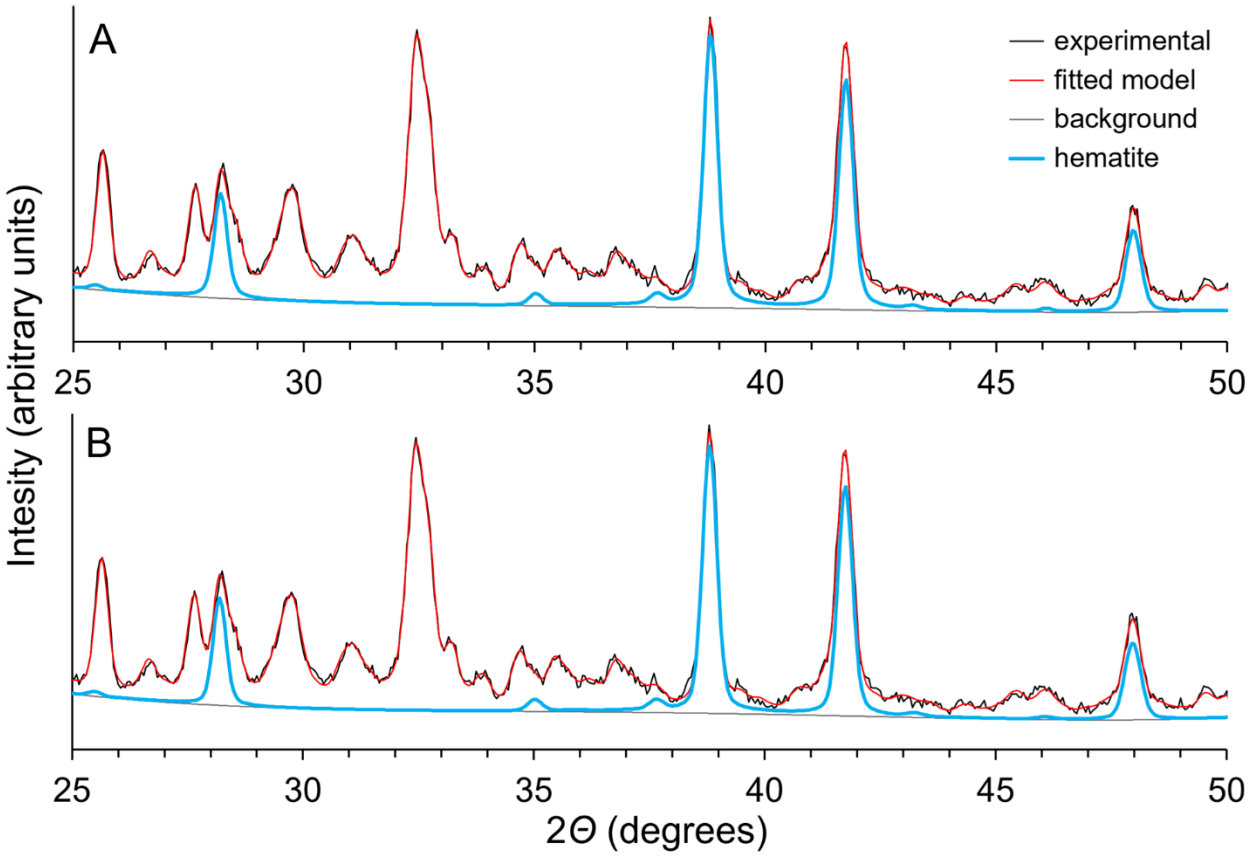

Fig. S12. Same as Fig. S5 but for Stoer.

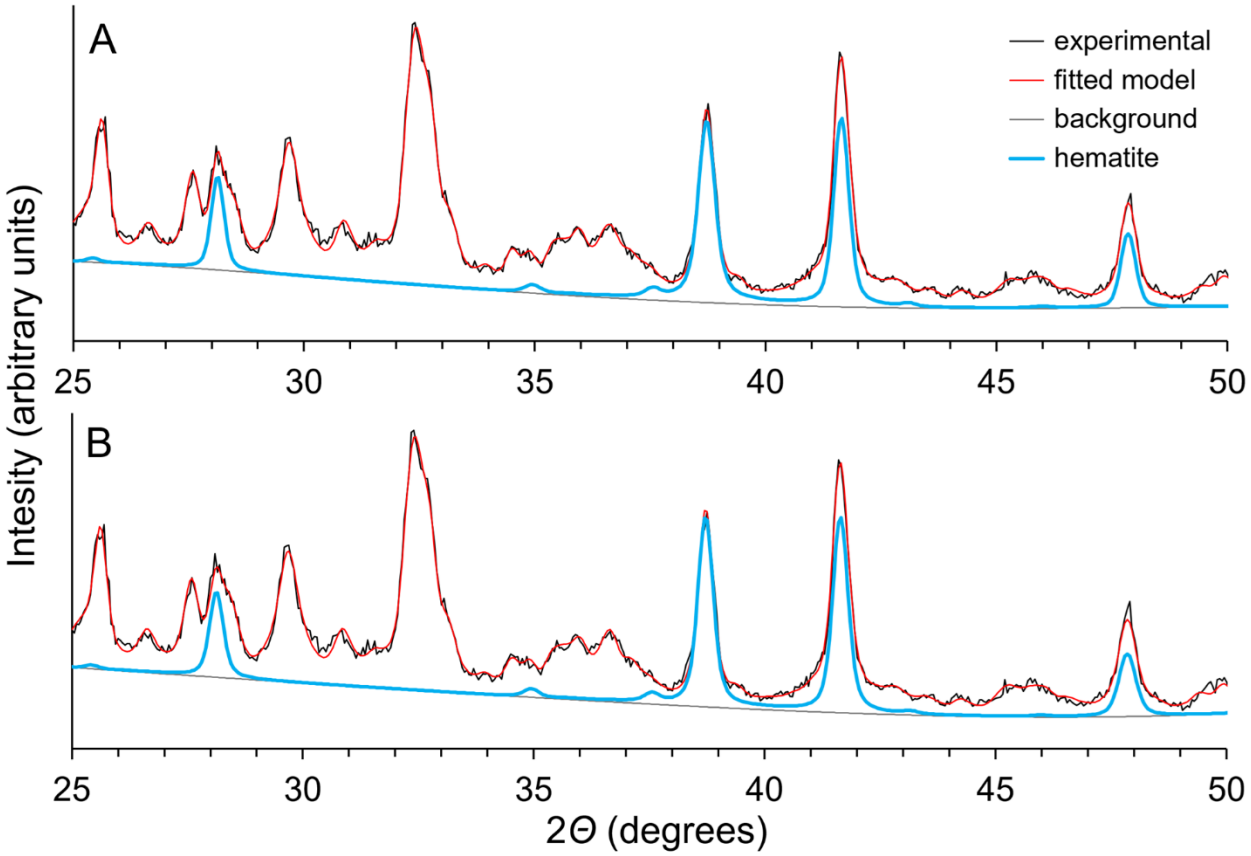

Fig. S13. Same as Fig. S5 but for Highfield.

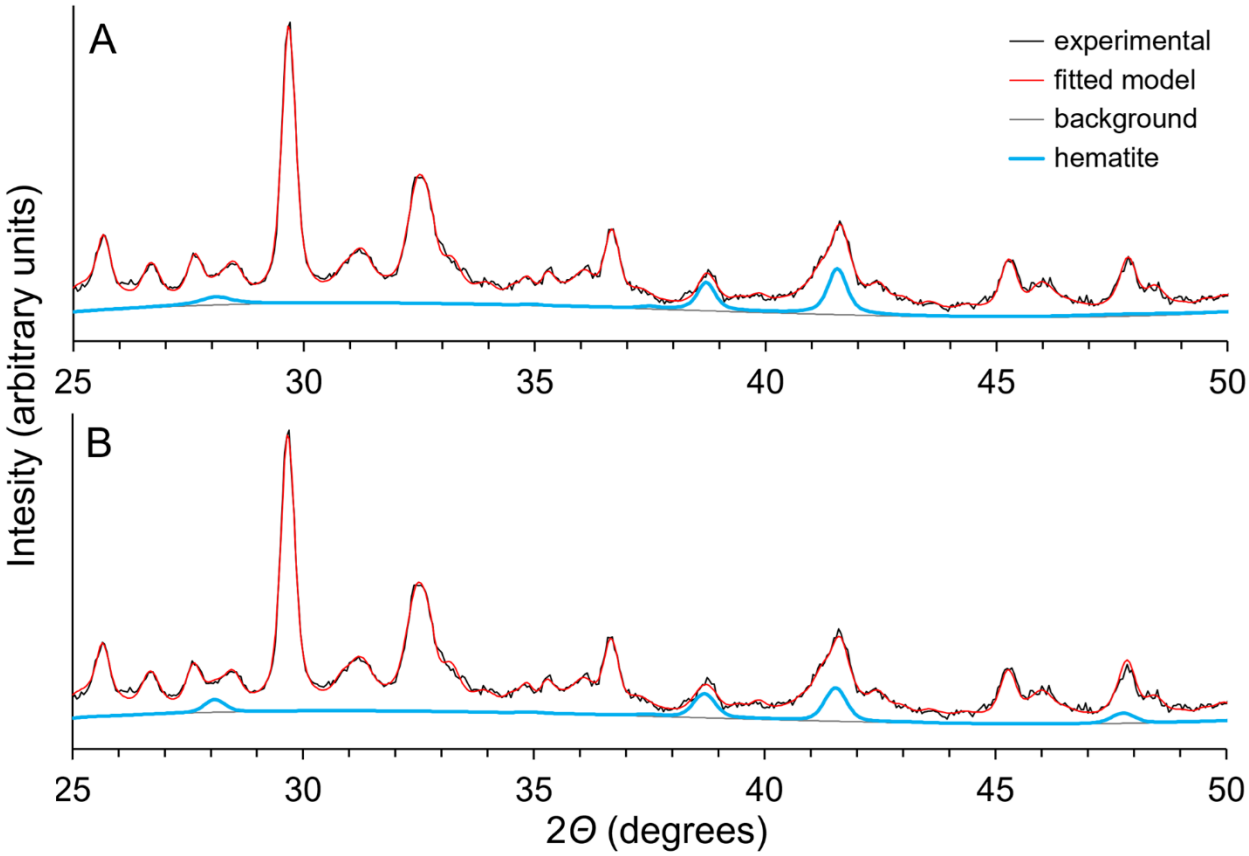

Fig. S14. Same as Fig. S5 but for Rock Hall.

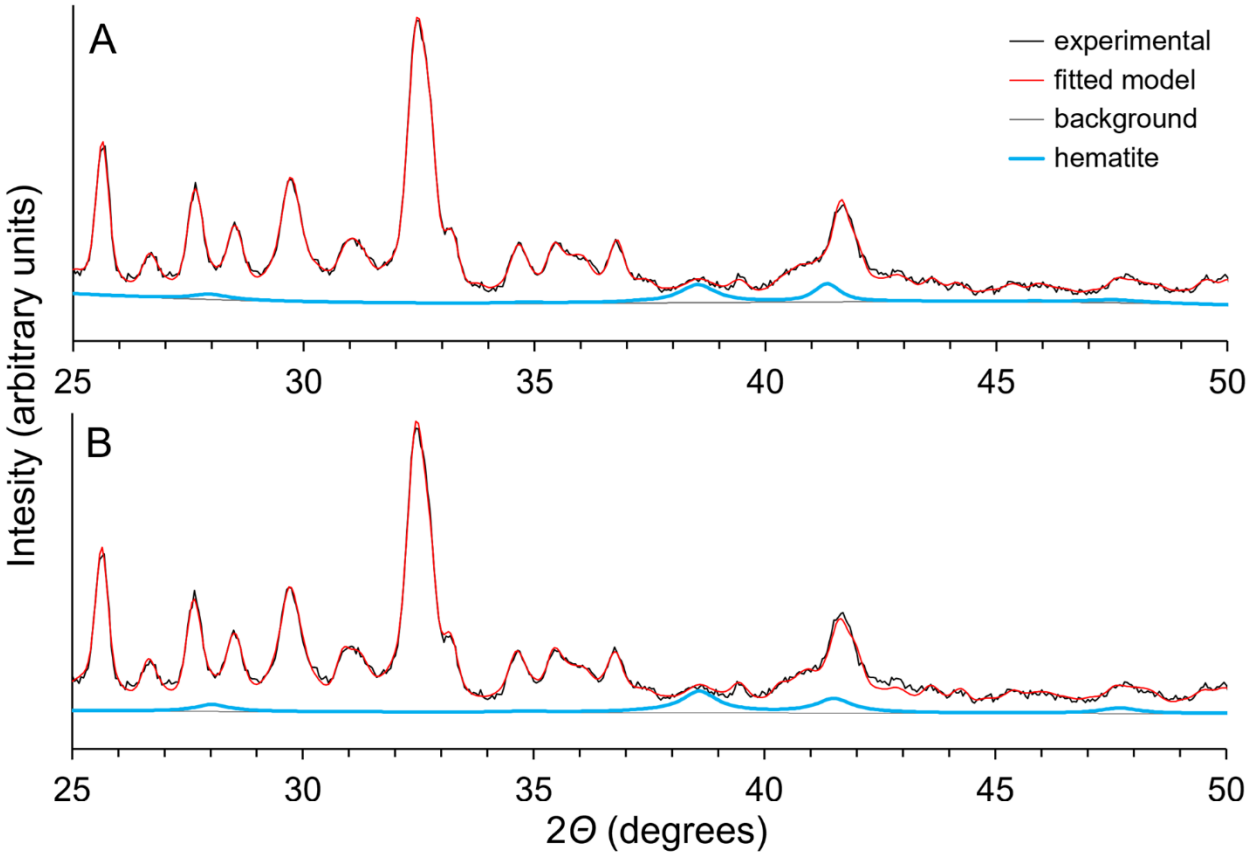

Fig. S15. Same as Fig. S5 but for Glen Etive2.

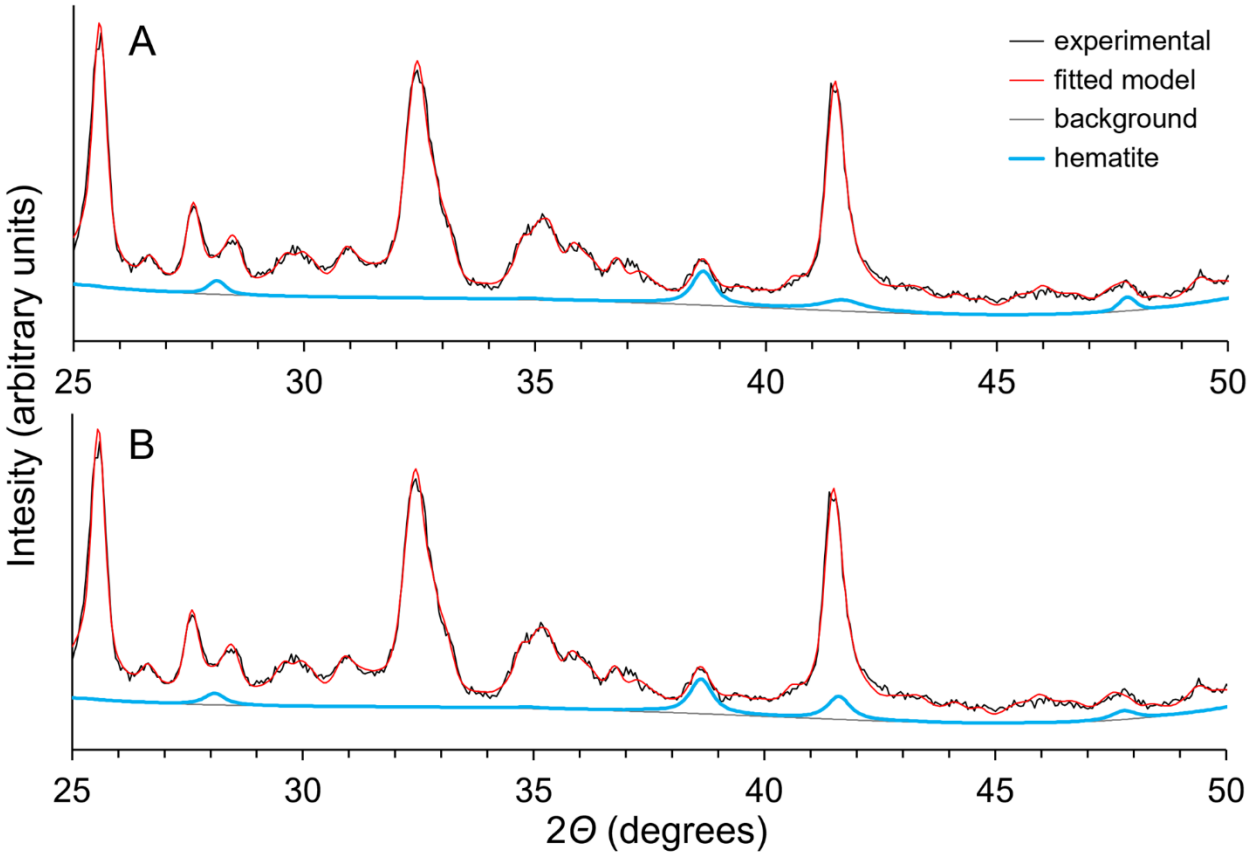

Fig. S16. Same as Fig. S5 but for Hutton.

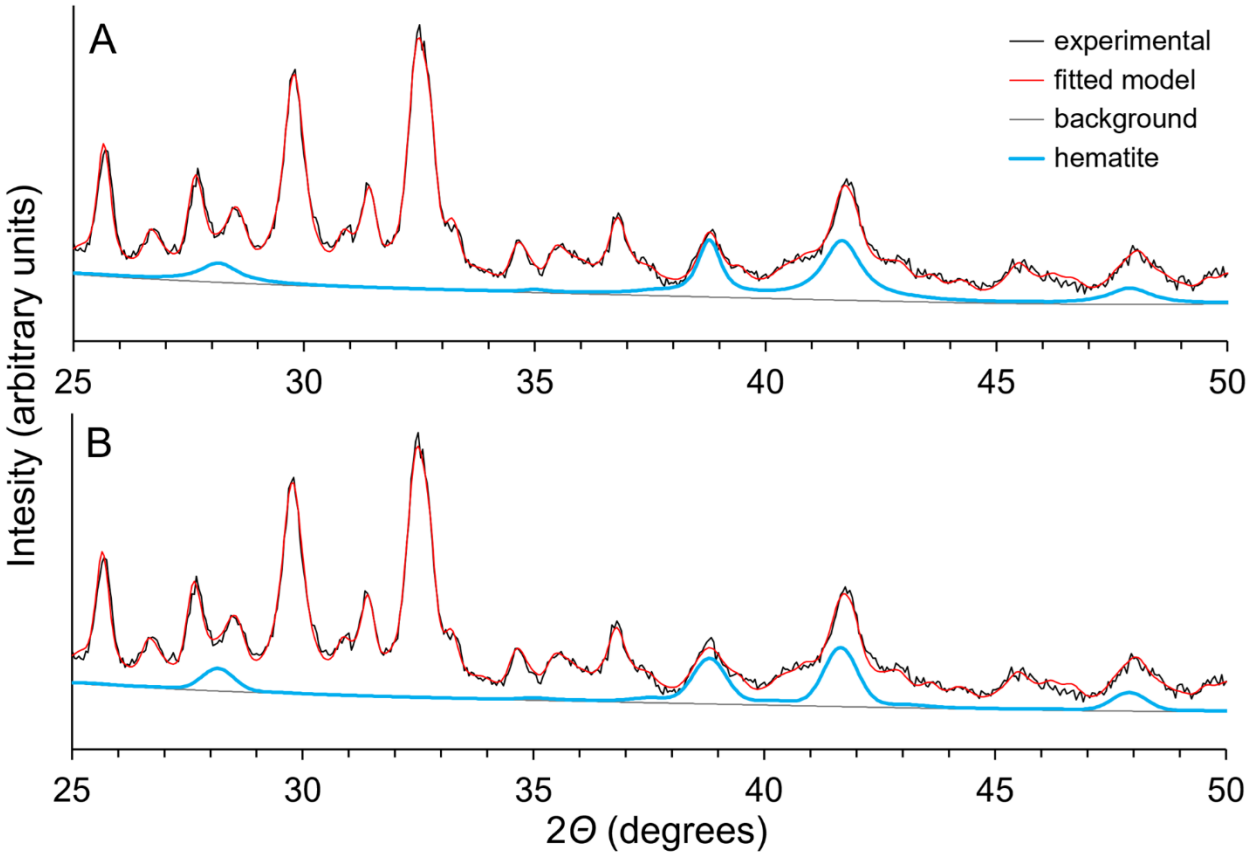

Fig. S17. Same as Fig. S5 but for Glasgow.

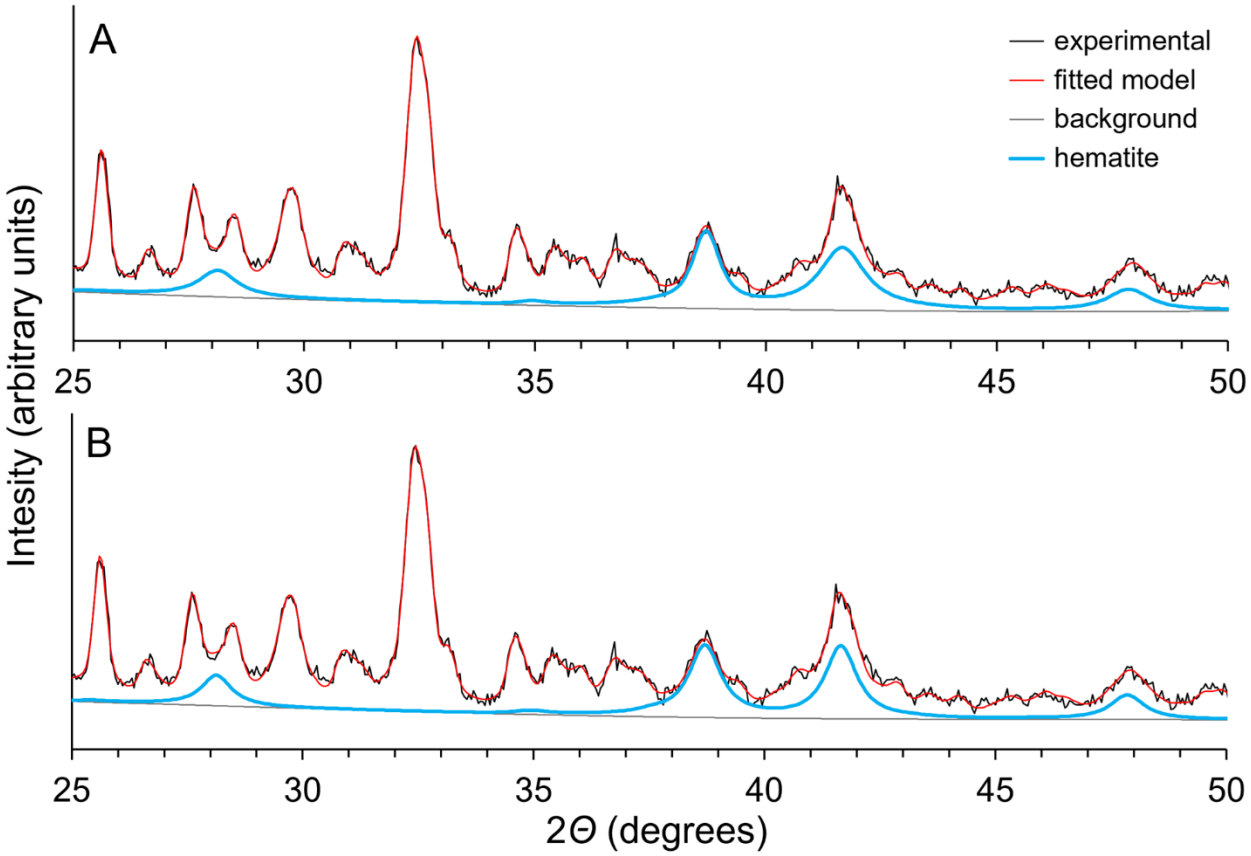

Fig. S18. Same as Fig. S5 but for Nontron.

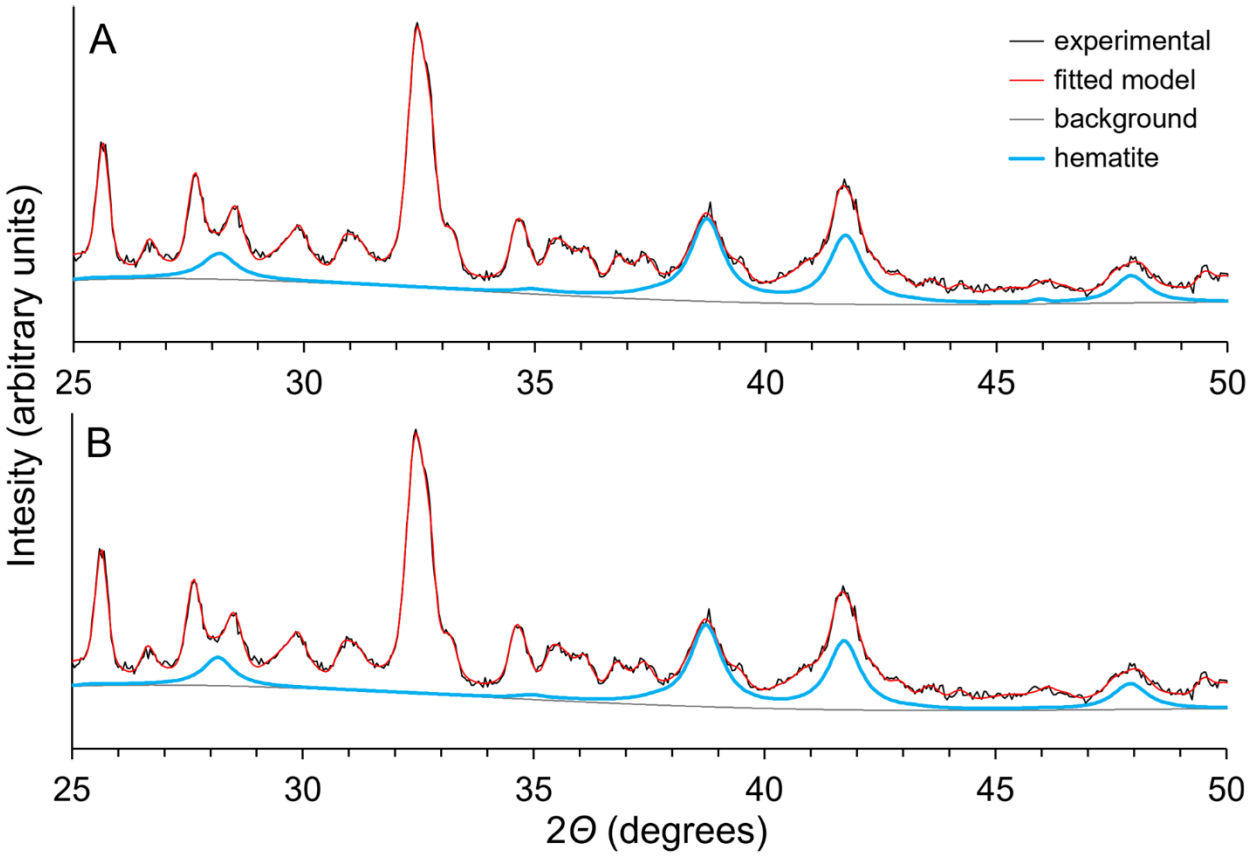

Fig. S19. Same as Fig. S5 but for Bardou.

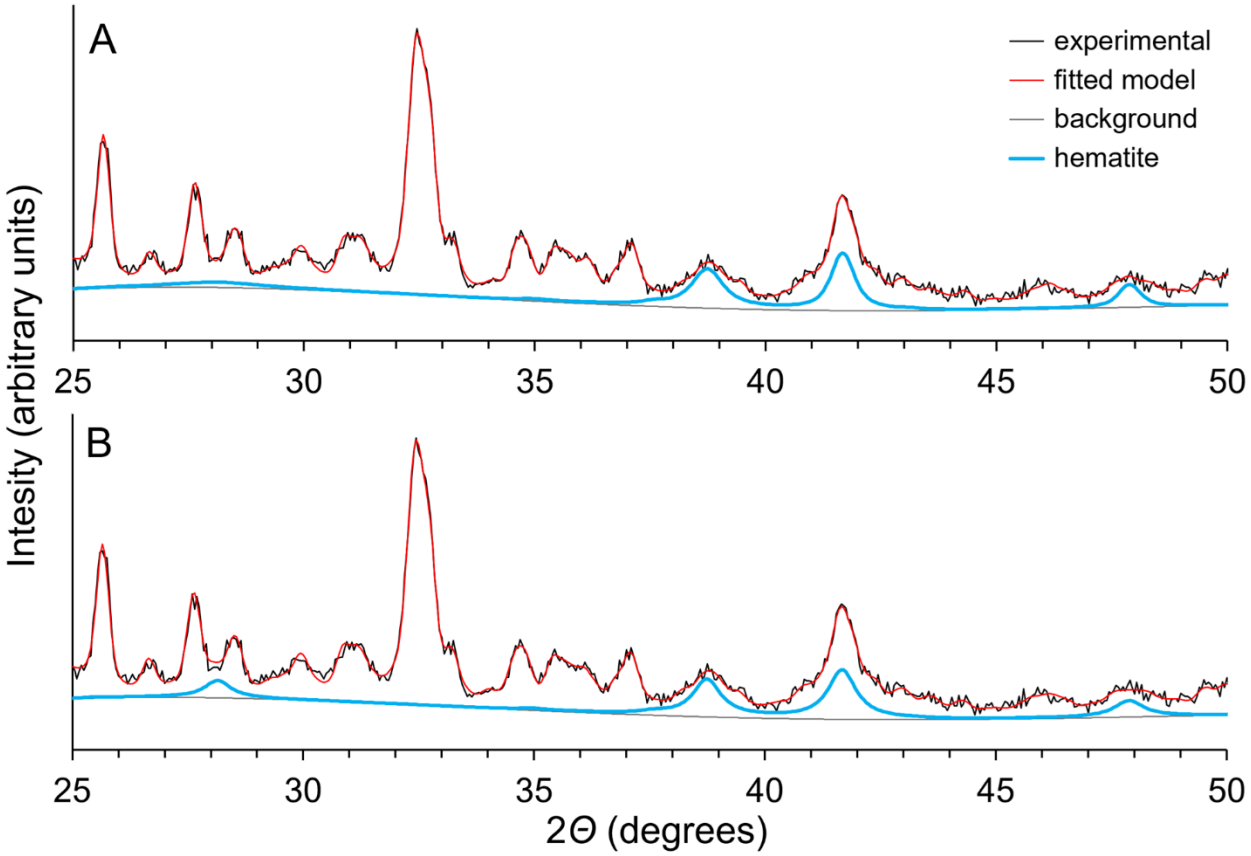

Fig. S20. Same as Fig. S5 but for Pontours.

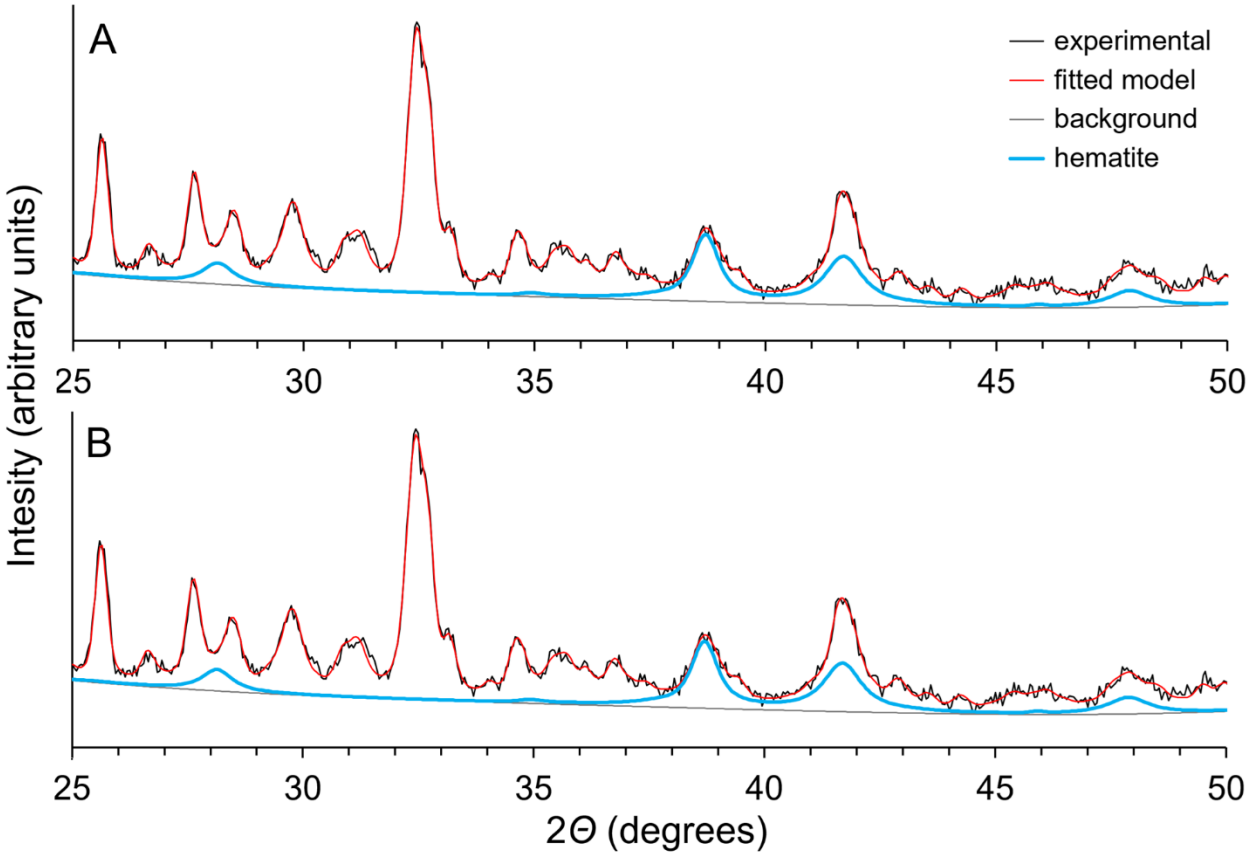

Fig. S21. Same as Fig. S5 but for Maria Gordon.

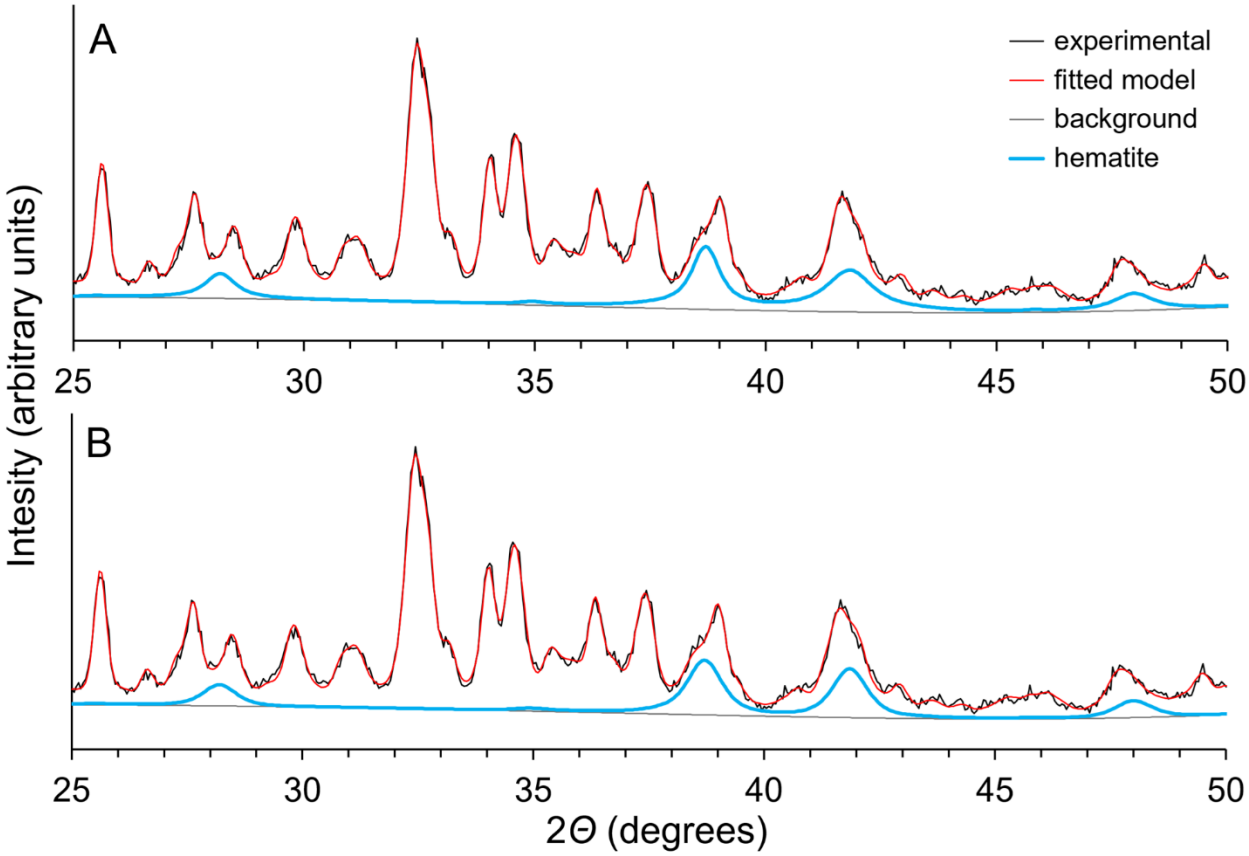

Fig. S22. Same as Fig. S5 but for Zechstein.

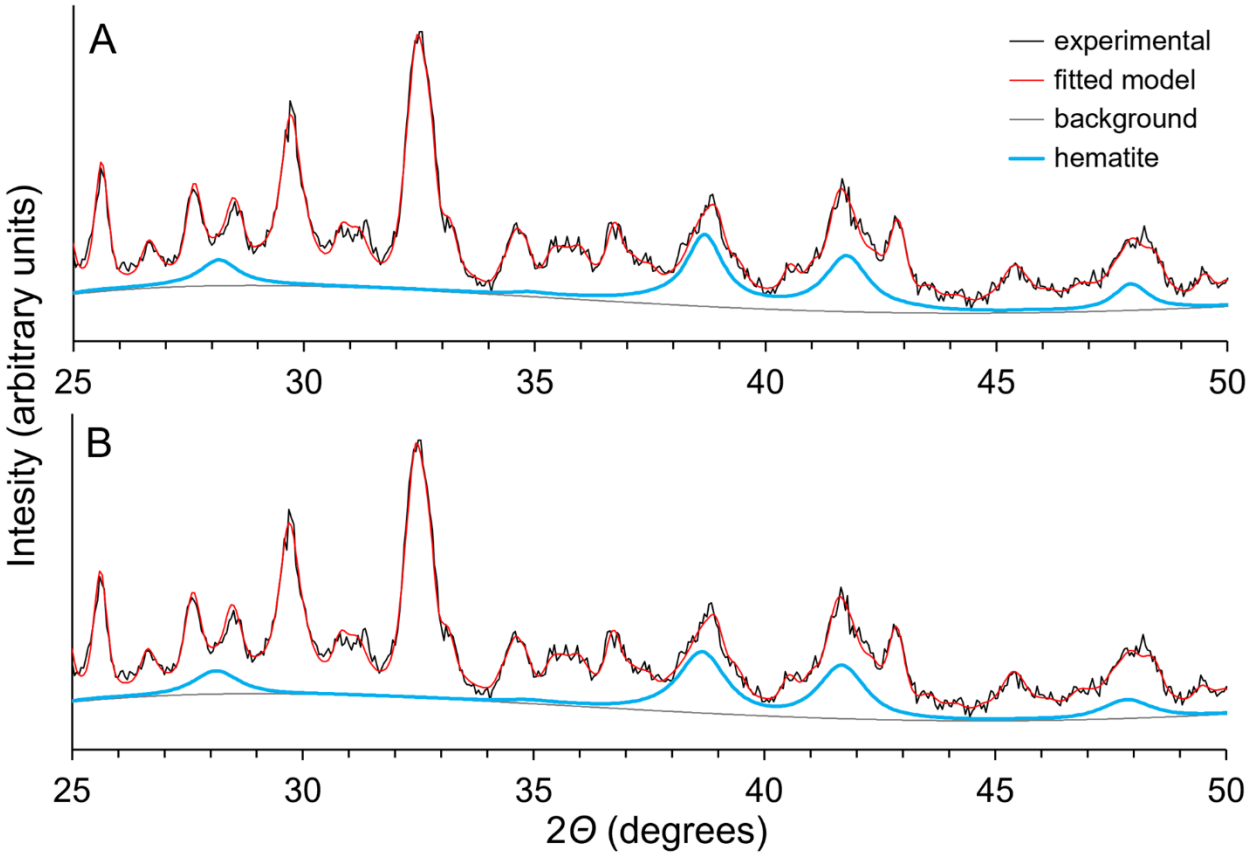

Fig. S23. Same as Fig. S5 but for Avanavero.

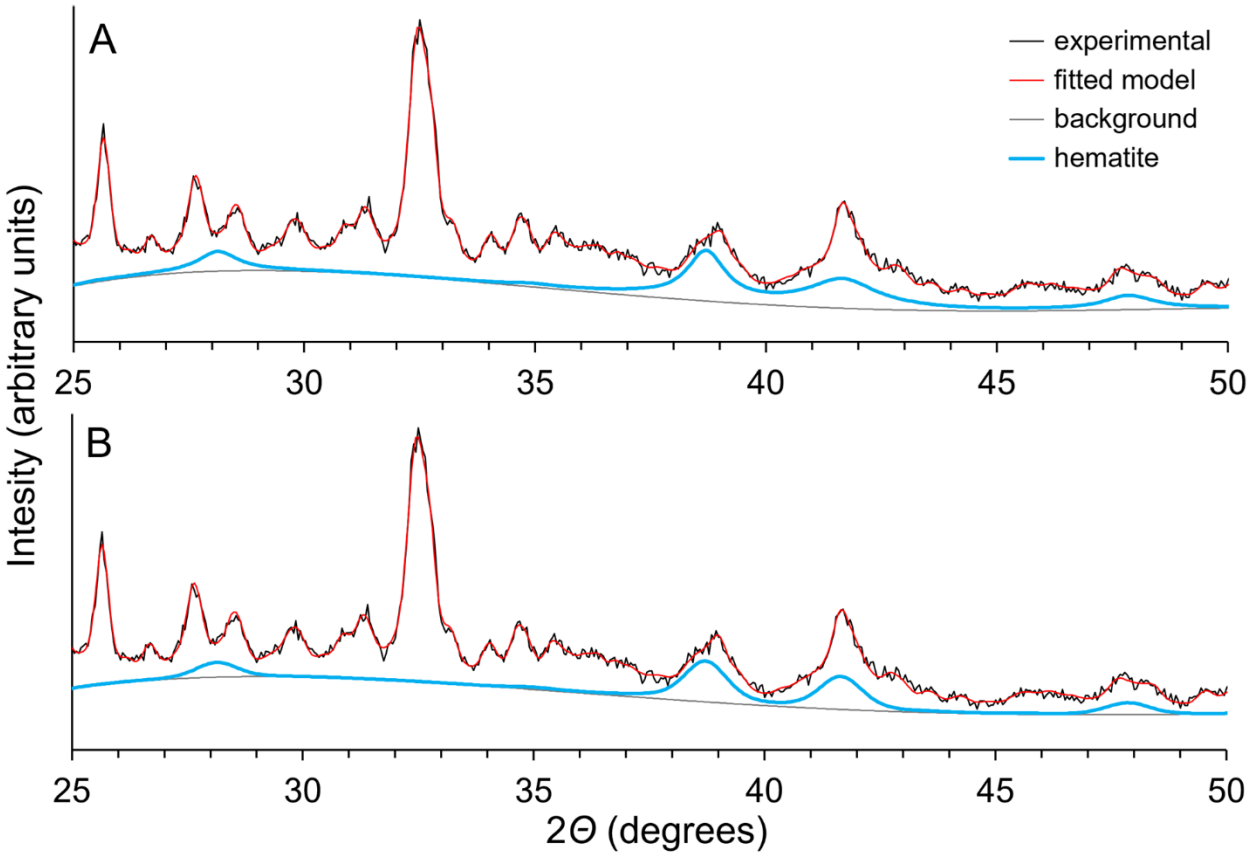

Fig. S24. Same as Fig. S5 but for Canaima.

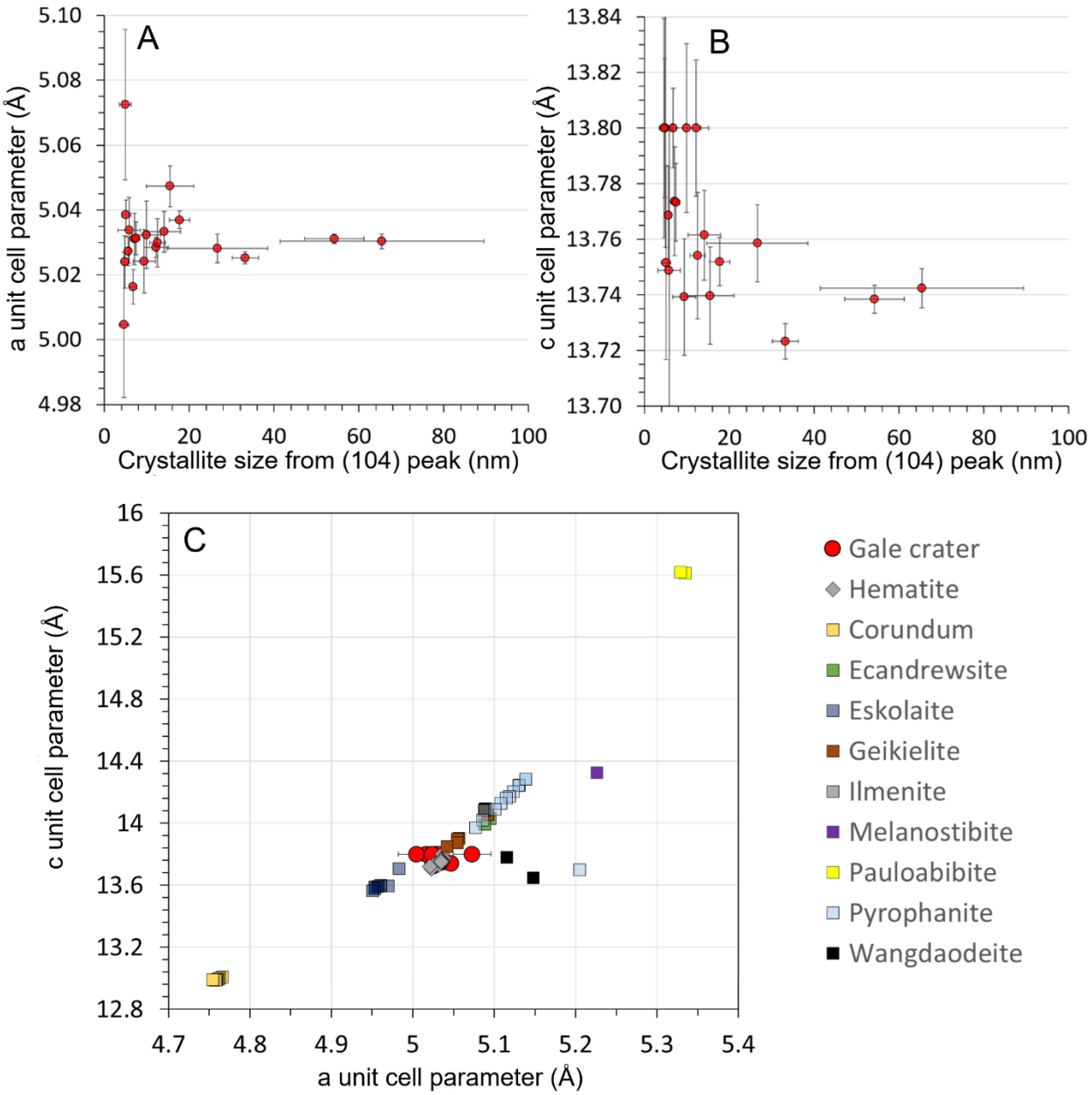

Figure S25. The lattice crystallographic parameters a and c. (A) Lattice parameter a versus crystallite size from (104) peak of hematite. (B) Lattice parameter *c* versus crystallite size from (104) peak of hematite. Error bars represent are 1 sigma derived from the refinement uncertainties. (C) Comparison of the unit-cell parameters with data for various isostructural minerals obtained from the American Mineralogist Crystal Structure Database (*61*). The unit cell parameters of Gale crater samples (red circles) are similar to values for hematite, indicating negligible substitution of other elements.

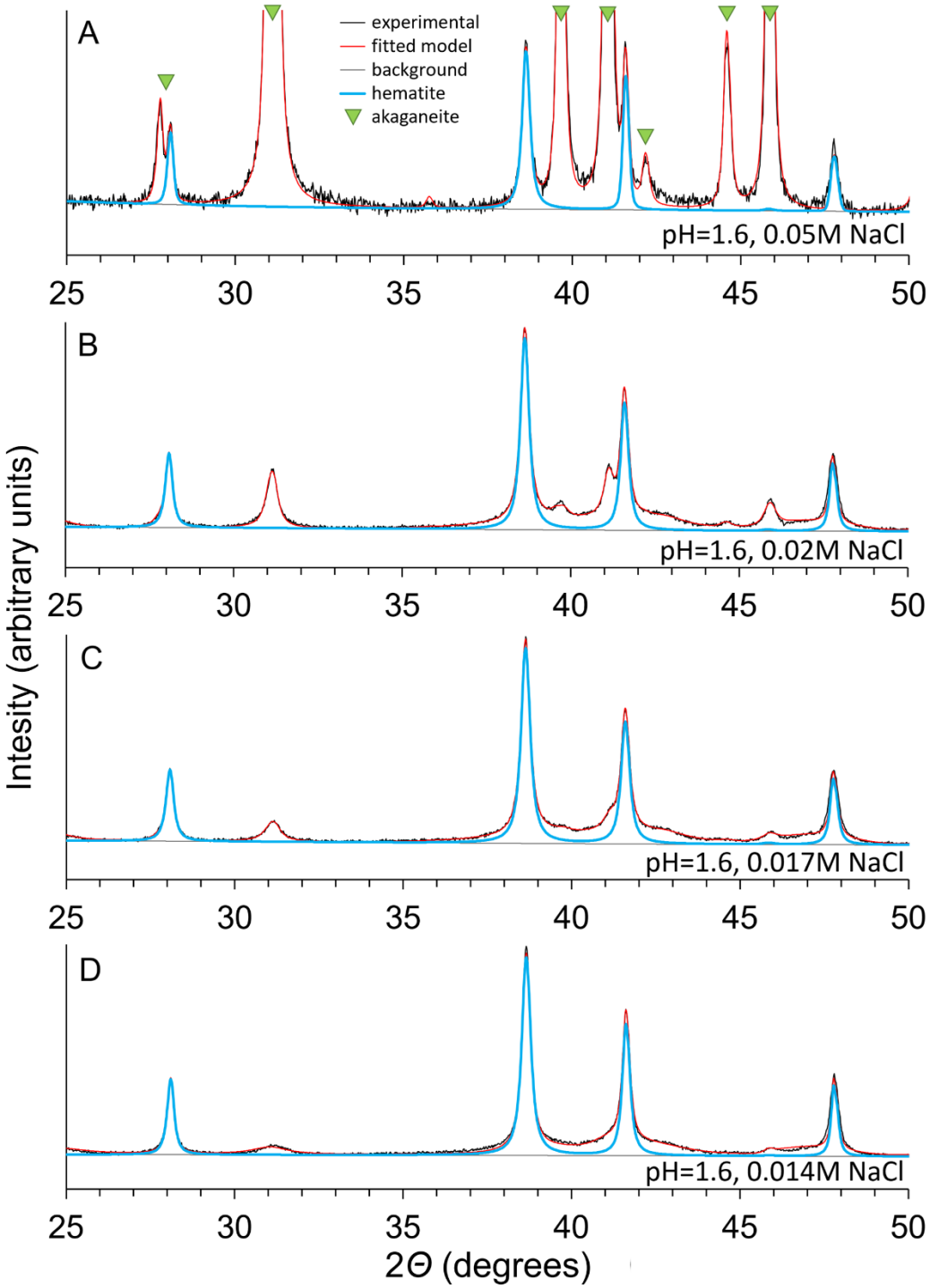

Fig. S26. Same as Fig. S5, but for synthetic hematite formed by hydrolysis of 0.1 M $Fe(ClO_4)_3$ at pH 1.6 with varying NaCl concentrations: (A) 0.05 M, (B) 0.02 M, (C) 0.017 M, and (D) 0.014 M (*22*). The model has independent fitting of mean sizes of crystallites for all four most intense hematite peaks. Peaks of akageneite are also visible (green triangles).

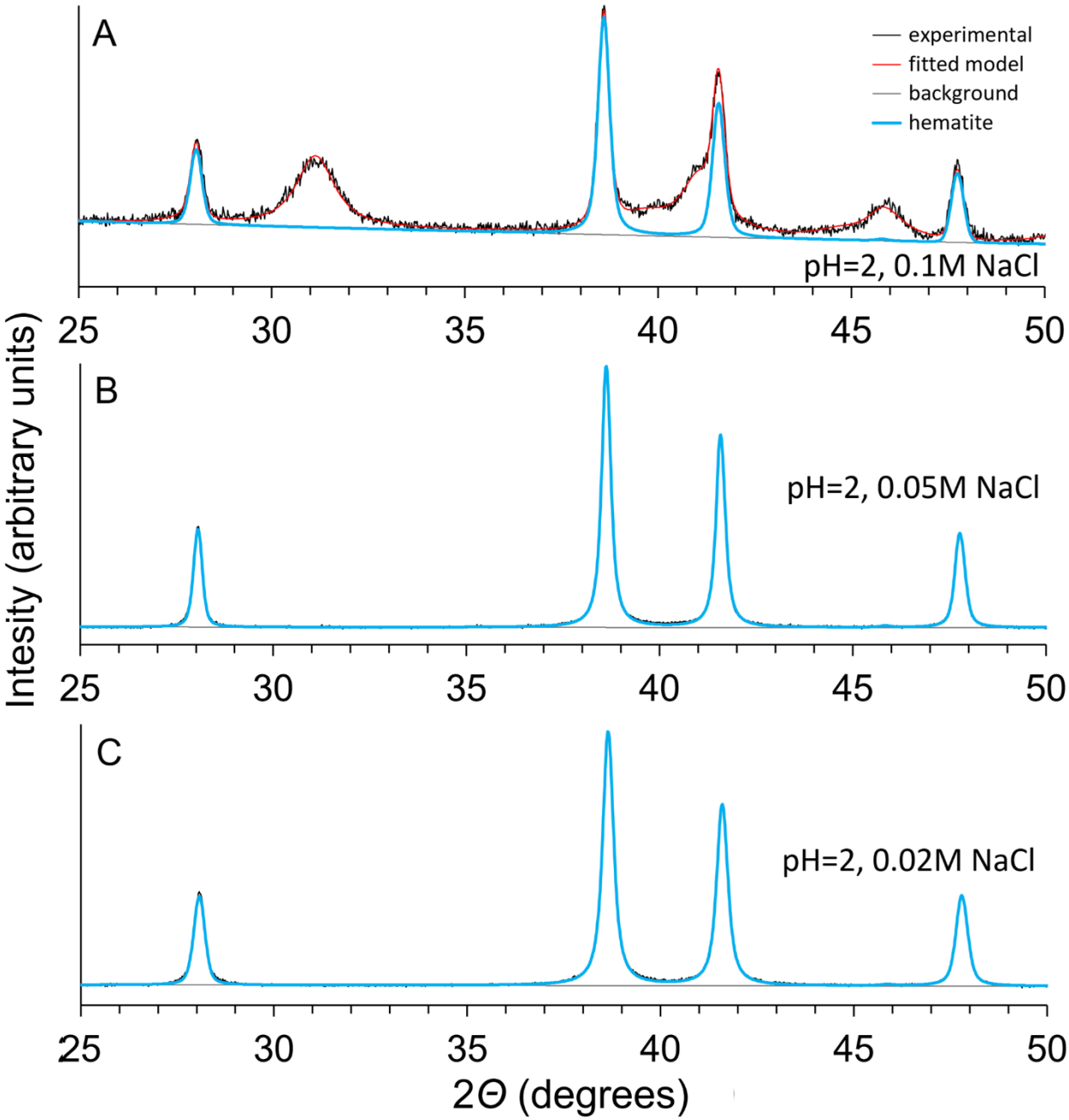

Fig. S27. Same as Fig. S26, but for synthetic hematite formed by hydrolysis of 0.1 M $Fe(ClO_4)_3$ at pH 2 with varying NaCl concentrations: (A) 0.1 M, (B) 0.05 M, and (C) 0.02 M (*22*).

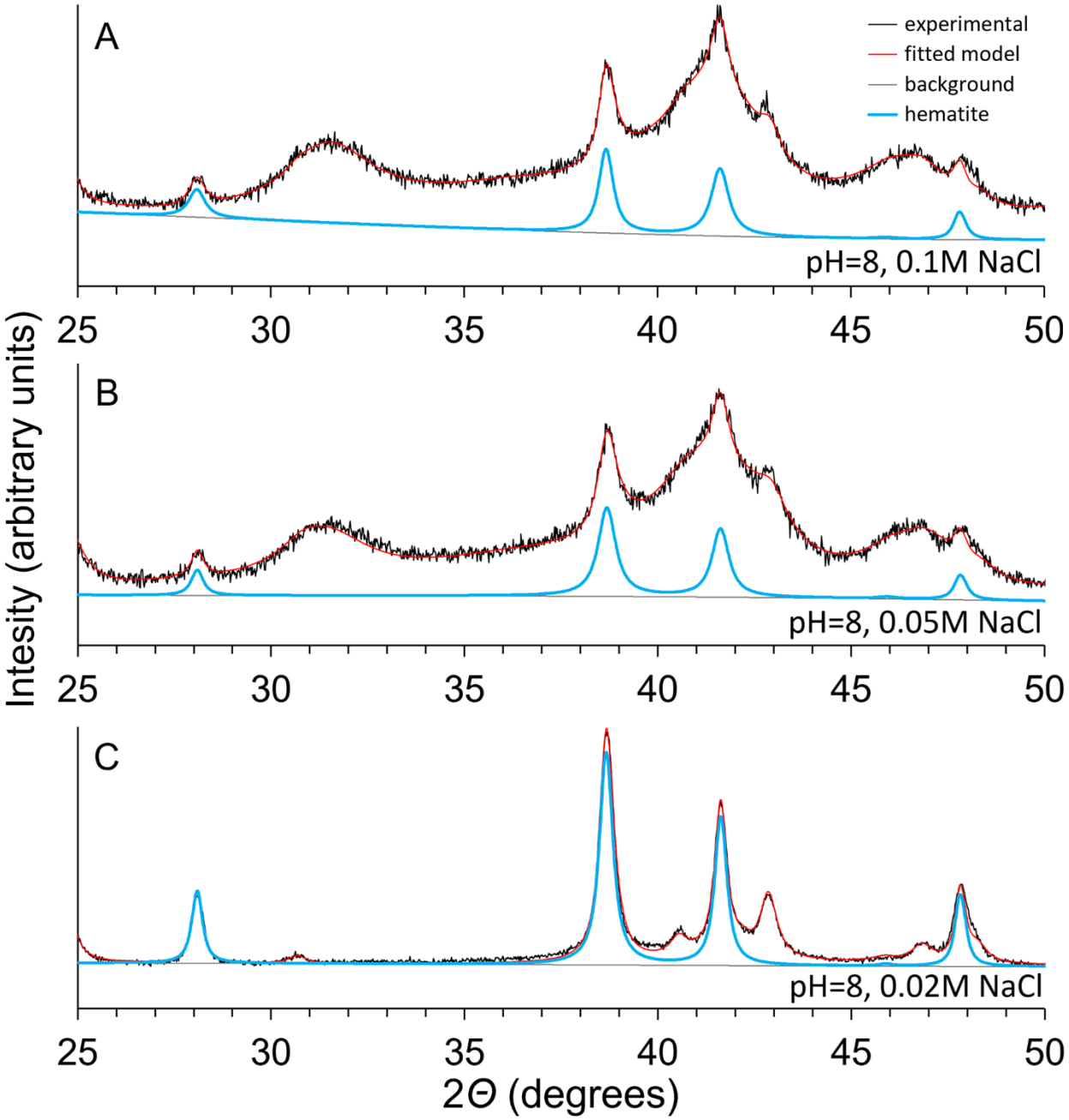

Fig. S28. Same as Fig. S26, but for synthetic hematite formed by ferrihydrite crystallization from 0.1 M $Fe(ClO_4)_3$ solution at pH 8 with varying NaCl concentrations: (A) 0.1 M, (B) 0.05 M, and (C) 0.02 M (*22*).

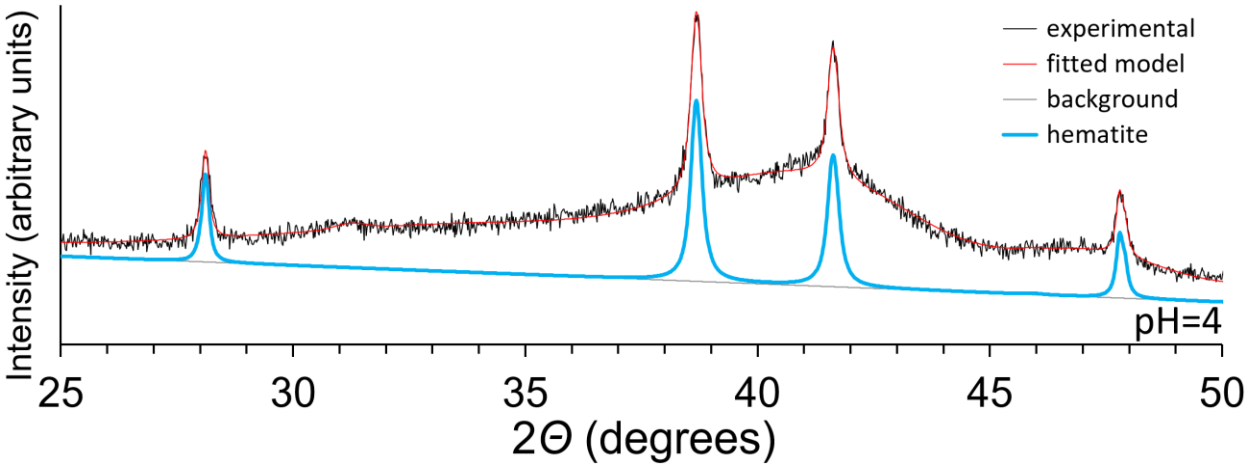

Fig. S29. Same as Fig. S26, but for synthetic hematite formed by ferrihydrite crystallization from 0.2 M $FeCl_3$ solution at pH 4 (*23*).

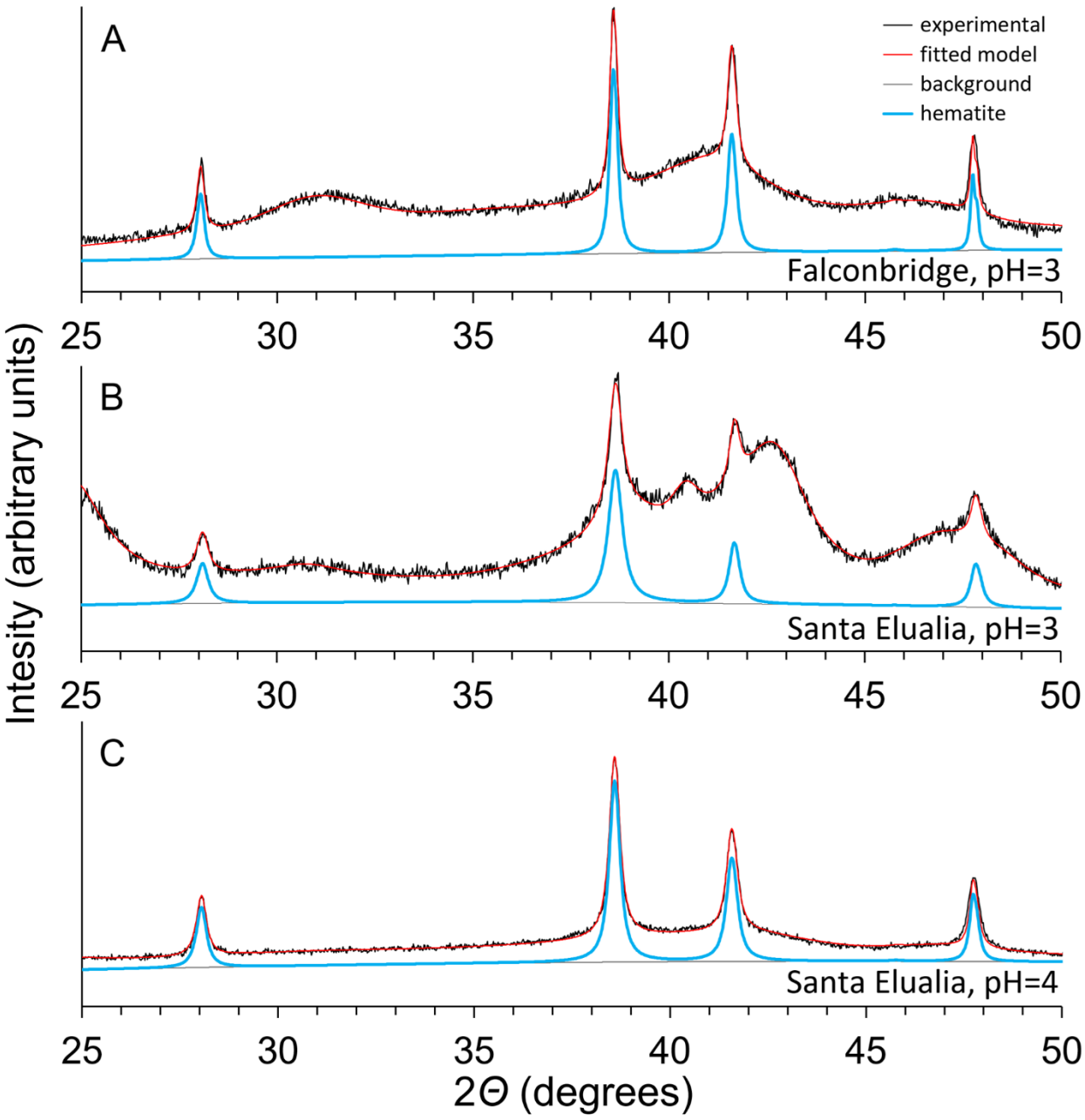

Fig. S30. Same as Fig. S26, but for synthetic hematite formed by crystallization of ferrihydrite precipitated in solution leached from (A) Falconbridge natural pyrrhotite at pH 3, and Santa Elualia natural pyrrhotite (B) at pH 3, and (C) at pH 4 (*24*).

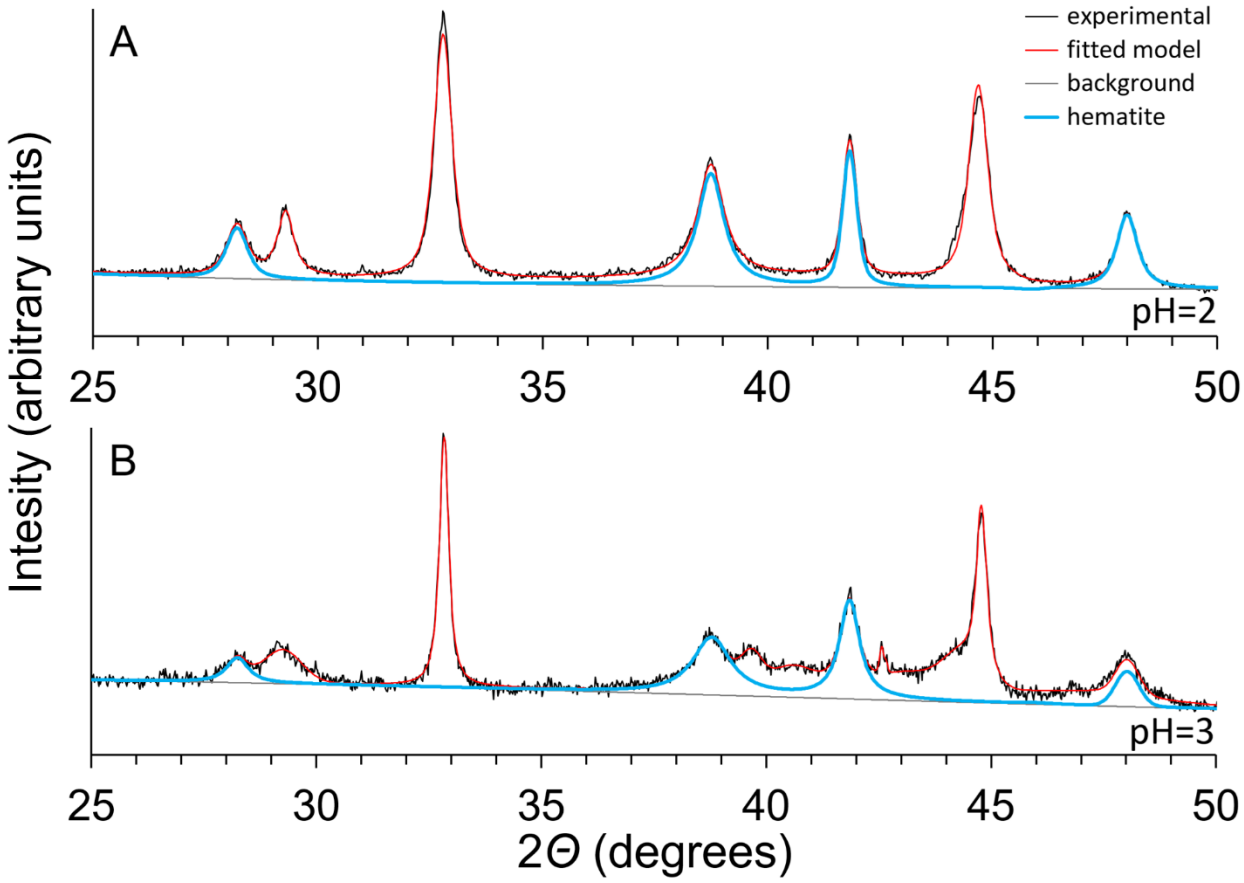

Fig. S31. Same as Fig. S26, but for synthetic hematite formed through hydrothermal basalt alteration in flow through experiments at (A) pH 2, and (B) pH 3 (*25*).

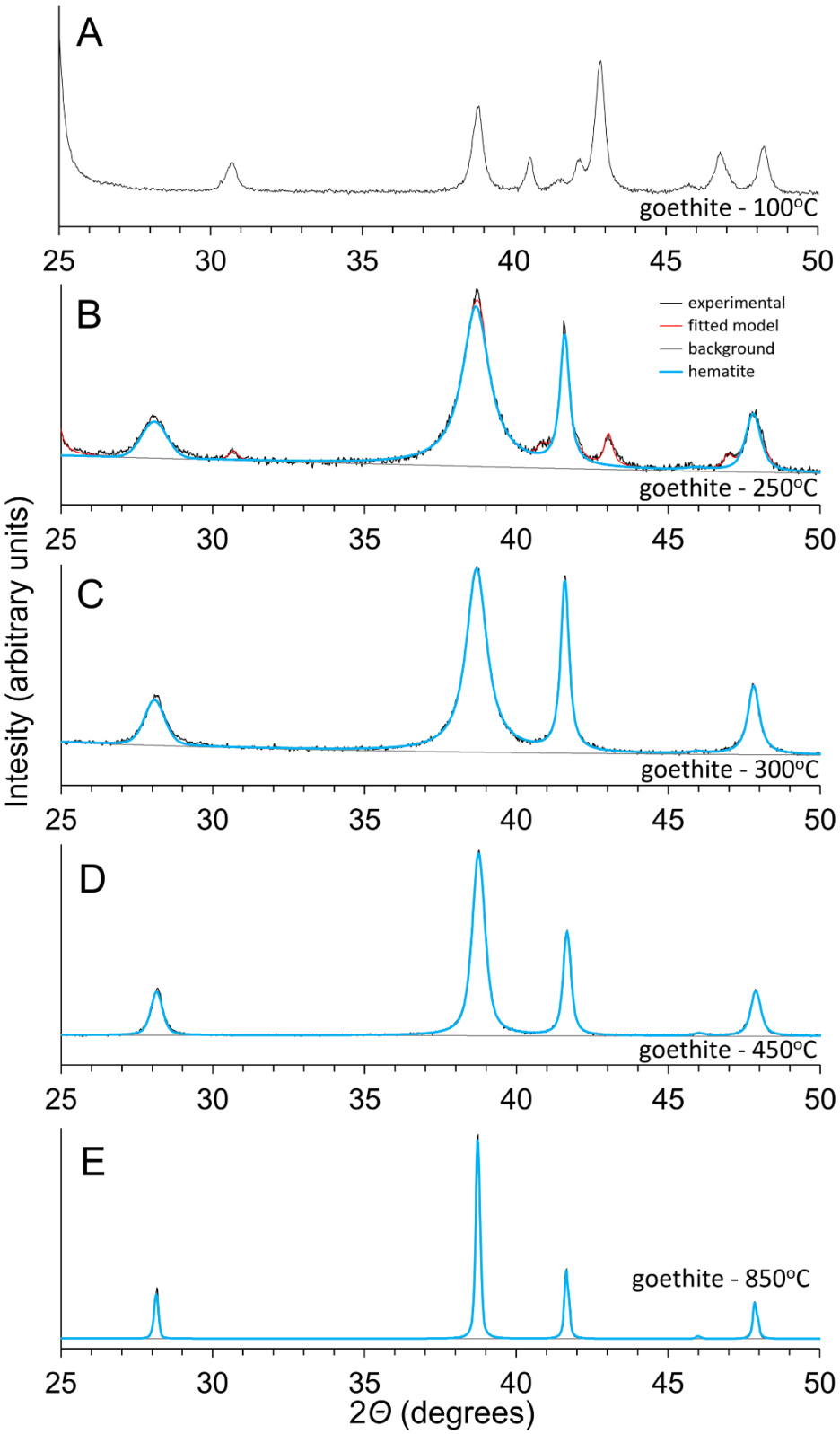

Fig. S32. Same as Fig. S26, but for goethite heated to (A) 100 °C, (B) 250 °C, (C) 300 °C, (D) 450 °C, and (E) 850 °C for 2 hrs. at each temperature. Hematite was formed at ≥250 °C, and its peaks are shown as thick blue lines. Hematite did not form at 100 °C, therefore no fitting model is presented.

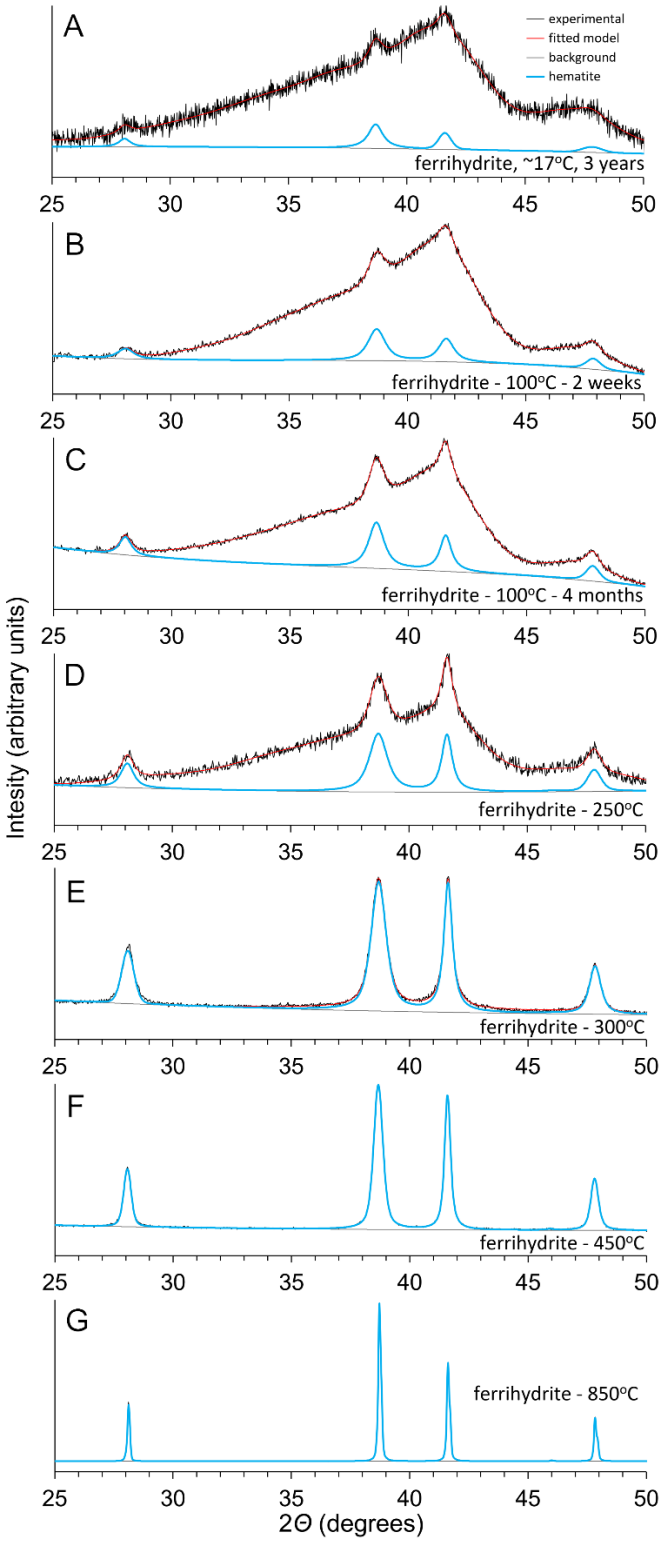

Fig. S33. Same as Fig. S26, but for ferrihydrite (A) stored for 3 years at 17 °C and 65 % relative humidity (*29*), and ferrihydrite heated to (B) 100 °C for 2 weeks, (C) 100 °C for 4 months, (D) 250 °C, (E) 300 °C, (F) 450 °C, and (G) 850 °C for 2 hrs.

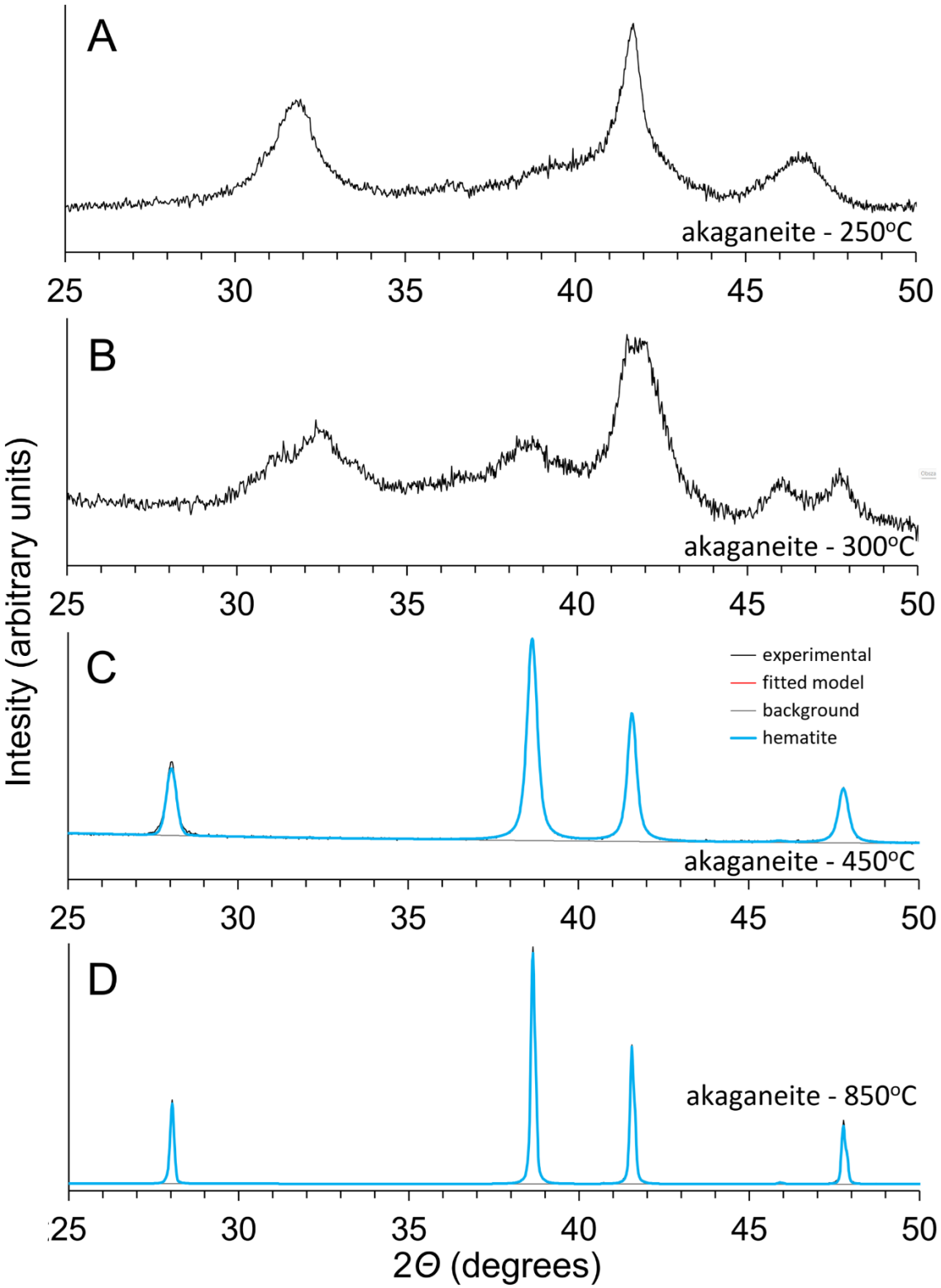

Fig. S34. Same as Fig. S26, but for akaganeite heated to (A) 250 °C, (B) 300 °C, (C) 450 °C, and (D) 850 °C for 2 hrs. at each temperature. Hematite did not form at 250 and 300 °C, therefore no fitting model is presented.

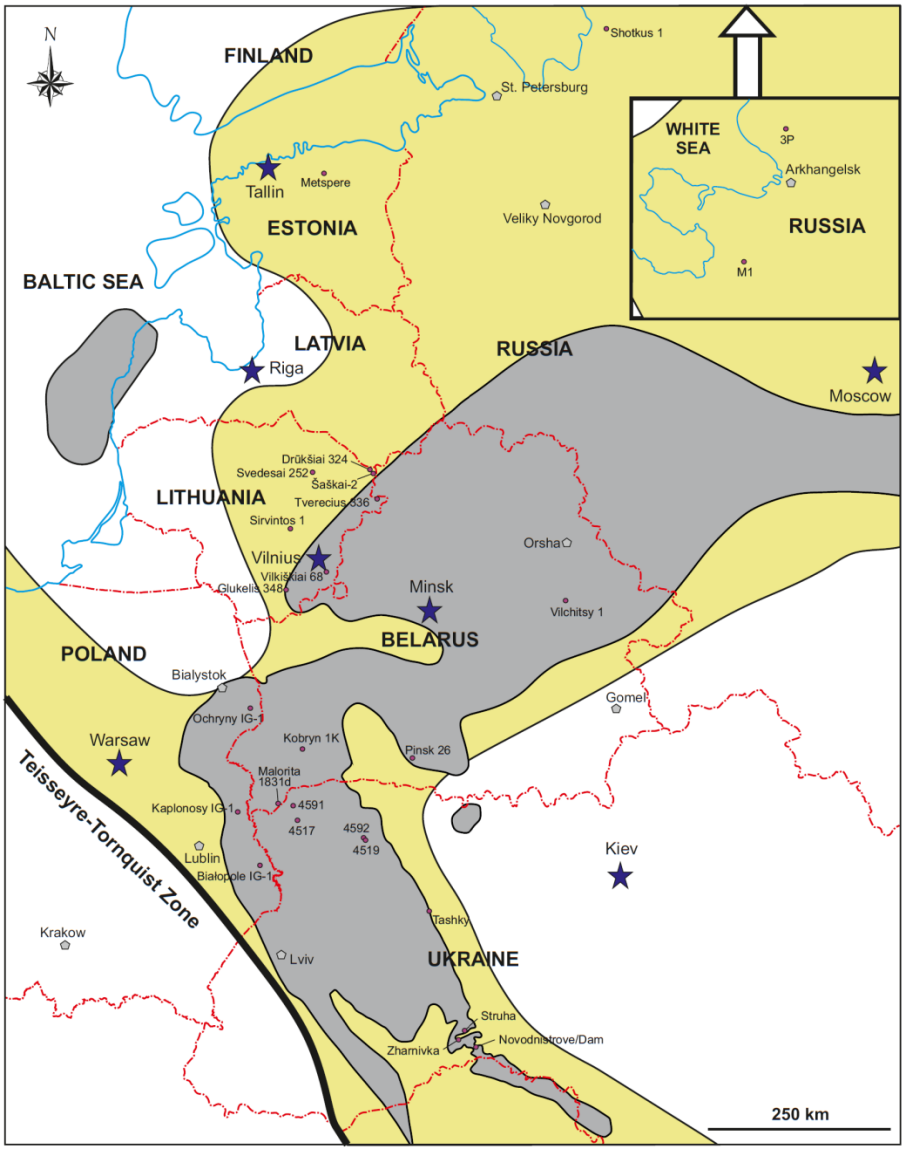

Fig. S35. Collection locations of the Ediacaran sample boreholes. The background map shows extent of the Ediacaran sedimentary rocks (yellow) and the underlying Ediacaran volcanic rocks of the Volyn Large Igneous Province (gray). Reproduced from (*62*) with permission from Elsevier. Blue lines – shoreline, red – country borders, black lines – borders of sedimentary/volcanic provinces. Blue stars – country capitals, grey pentagons – larger cities, purple circles – drilling locations.

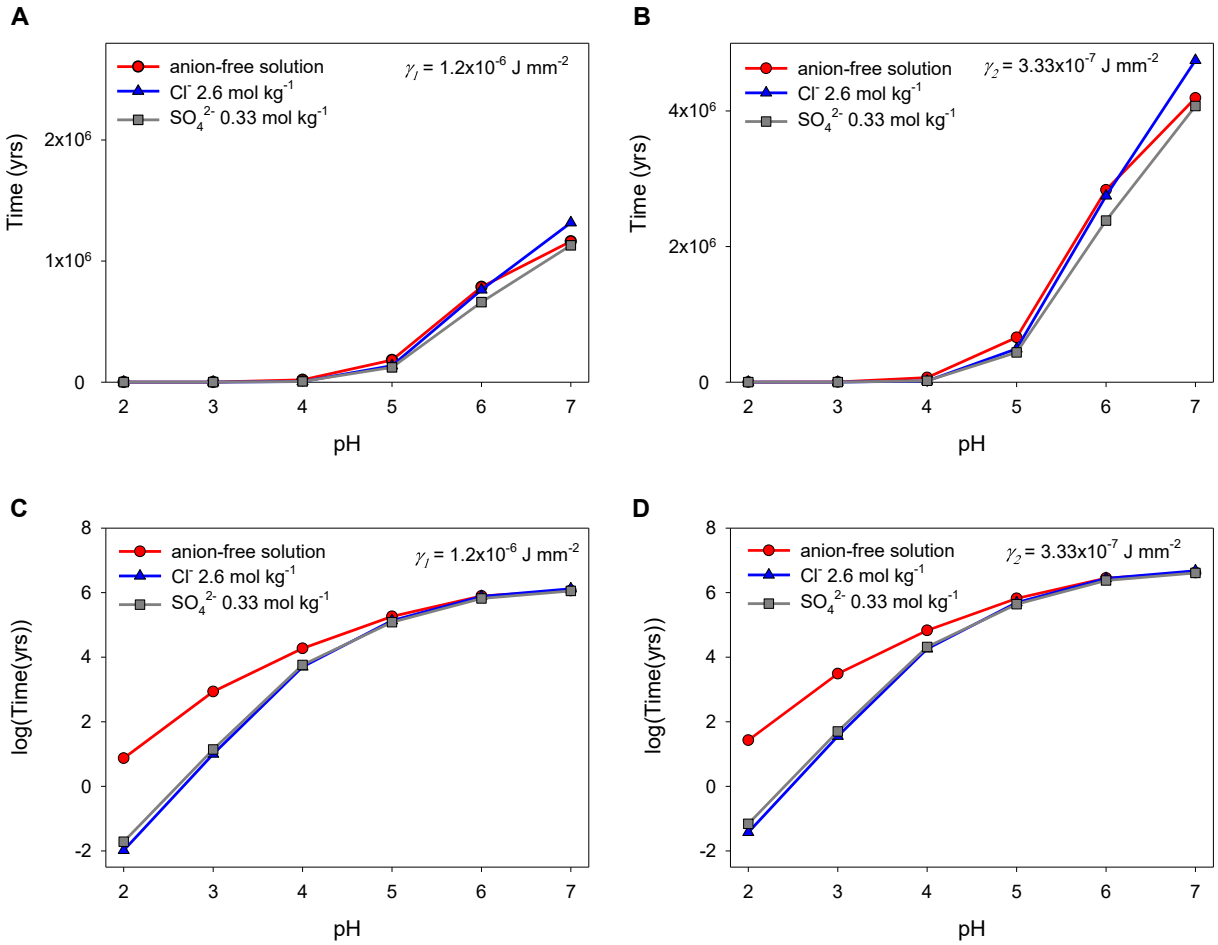

Fig. S36. Calculated time required for Ostwald ripening from 5 to 65 nm crystallite size at 50 °C as a function of pH in anion-free solution (red circles and line) and in solutions containing 2.6 mol kg^{-1} Cl^- (blue triangles and line) or 0.33 mol kg^{-1} SO_4^{2-} (gray squares and line). Panels show results for interfacial energy of (A) bulk hematite (γ_1) and (B) nanoparticles (γ_2). Panels (C) and (D) show the same data plotted as common logarithm of time for bulk hematite and nanoparticles, respectively.

Table S1. Volume-weighted mean crystallite sizes (LVol, in nm) for hematite reflections (104) and (110) calculated from XRD peak broadening. σ $LVol_{(104)}$ and σ $LVol_{(110)}$ denote the corresponding standard uncertainties. The refined unit cell parameters (a and c, in Å) are listed together with their standard uncertainties (σ a and σ c).

	Sample name	$LVol_{(104)}$	σ $LVol_{(104)}$	$LVol_{(110)}$	σ $LVol_{(110)}$	a	σ a	c	σ c
Gale crater	Confidence Hills	65.4	24.0	77.1	78.3	5.030	0.002	13.742	0.007
	Mojave2	12.2	2.9	22.9	8.8	5.028	0.003	13.800	0.024
	Oudam	54.2	7.0	48.6	10.7	5.031	0.002	13.738	0.005
	Marimba	26.6	11.9	18.7	5.6	5.028	0.004	13.759	0.014
	Quela	14.1	3.8	11.6	2.2	5.033	0.006	13.761	0.016
	Sebina	12.5	1.8	11.9	3.2	5.030	0.007	13.754	0.023
	Duluth	5.1	1.1	9.8	2.9	5.039	0.005	13.751	0.035
	Stoer	33.2	3.1	32.9	4.5	5.025	0.002	13.723	0.006
	Highfield	17.7	2.4	26.4	6.8	5.037	0.008	13.752	0.009
	Rock Hall	15.5	5.6	14.2	8.2	5.047	0.006	13.740	0.018
	Glen Etive2	4.9	1.4	8.3	8.1	5.073	0.023	13.800	0.043
	Glasgow	9.4	2.7	4.9	1.8	5.024	0.010	13.739	0.021
	Hutton	9.9	3.4	4.2	9.4	5.032	0.010	13.800	0.030
	Nontron	7.1	0.9	3.9	1.2	5.031	0.008	13.773	0.020
	Bardou	5.6	0.7	5.8	1.3	5.027	0.004	13.769	0.018
	Pontours	5.8	2.7	9.3	4.2	5.034	0.010	13.749	0.052
	Maria Gordon	7.4	0.9	4.9	1.0	5.031	0.005	13.773	0.014
	Zechstein	6.8	0.8	3.8	0.7	5.016	0.005	13.800	0.014
	Avanavero	4.8	0.8	4.1	0.9	5.024	0.008	13.800	0.025
	Canaima	4.6	1.1	2.5	2.1	5.005	0.022	13.800	0.040
Formation in solution	pH 1.6, 0.05M NaCl	22.3	4.0	40.0	8.4	5.039	0.001	13.783	0.001
	pH 1.6, 0.02M NaCl	17.1	0.2	21.2	0.4	5.041	0.001	13.788	0.001
	pH 1.6, 0.017M NaCl	16.1	0.1	18.7	0.3	5.041	0.001	13.789	0.001
	pH 1.6, 0.014M NaCl	16.6	0.2	22.6	0.5	5.041	0.001	13.789	0.001
	pH 2, 0.1M NaCl	15.2	0.6	16.4	1.0	5.043	0.001	13.800	0.001
	pH 2, 0.05M NaCl	19.6	0.3	21.2	0.4	5.039	0.001	13.781	0.001
	pH 2, 0.02M NaCl	15.6	0.2	16.1	0.3	5.038	0.001	13.774	0.001
	pH 8, 0.1M NaCl	7.9	0.3	9.5	0.5	5.037	0.001	13.769	0.004
	pH 8, 0.05M NaCl	6.6	0.2	8.5	0.5	5.035	0.001	13.756	0.005
	pH 8, 0.02M NaCl	11.6	0.1	13.4	0.2	5.037	0.001	13.776	0.001
	pH 4, 0.2 M $FeCl_3$	19.3	0.7	23.6	1.3	5.040	0.001	13.774	0.002
	Falconbridge, pH 3	24.8	0.7	25.5	1.1	5.036	0.001	13.800	0.001
	Santa Eulalia, pH 3	11.1	0.4	17.6	2.1	5.032	0.001	13.800	0.003
	Santa Eulalia, pH 4	15.8	0.2	16.0	0.3	5.039	0.001	13.800	0.001
	Basalt alteration, pH 2	4.3	1.4	14.1	2.6	5.017	0.001	13.788	0.002
	Basalt alteration, pH 3	3.1	0.1	12.3	0.9	5.020	0.001	13.783	0.006
Heating of Fe oxyhydroxides	Goethite, 250 °C, 2 hrs.	4.0	0.1	13.5	1.7	5.035	0.001	13.760	0.002
	Goethite, 300 °C, 2 hrs.	5.4	0.1	16.4	1.0	5.040	0.001	13.754	0.001
	Goethite, 450 °C, 2 hrs.	10.1	0.1	19.2	0.5	5.038	0.001	13.753	0.001
	Goethite, 850 °C, 2 hrs.	51.2	1.1	58.6	3.0	5.036	0.001	13.751	0.001
	Ferrihydrite, ~17 °C, 3 years	5.9	9.4	9.8	7.1	5.035	0.006	13.747	0.019
	Ferrihydrite, 100 °C, 2 weeks	5.4	1.2	6.2	2.0	5.031	0.006	13.747	0.018
	Ferrihydrite, 100 °C, 4 months	5.7	0.8	8.0	3.9	5.034	0.003	13.747	0.008
	Ferrihydrite, 250 °C, 2 hrs.	5.0	0.7	9.0	1.6	5.039	0.001	13.747	0.007
	Ferrihydrite, 300 °C, 2 hrs.	6.3	0.1	11.4	0.8	5.035	0.001	13.755	0.001
	Ferrihydrite, 450 °C, 2 hrs.	11.7	0.1	19.7	0.3	5.037	0.001	13.755	0.001
	Ferrihydrite, 850 °C, 2 hrs.	91.4	1.8	103.6	3.2	5.037	0.001	13.742	0.001
	Akaganeite, 450 °C, 2 hrs.	15.5	0.3	19.0	0.5	5.037	0.001	13.758	0.001
	Akaganeite, 850 °C, 2 hrs,	79.5	1.9	80.6	2.6	5.036	0.001	13.747	0.001

Table S2. Refined parameters of the number-weighted log-normal crystallite size distribution (μ and σ^2) obtained by WPPM analysis, with estimated uncertainties for the analyzed samples.

Sample name	σ^2	$\sigma\,\sigma^2$	μ	$\sigma\,\mu$
Confidence Hills	0.33	4.81	3.41	14.23
Mojave2	0.17	0.47	2.77	1.26
Oudam	0.14	0.85	3.58	2.18
Marimba	0.65	0.32	1.42	1.29
Quela	0.61	0.19	0.95	0.76
Sebina	0.43	0.20	1.37	0.77
Duluth	0.42	0.19	0.86	0.78
Stoer	0.17	0.36	3.00	0.92
Highfield	0.56	0.18	1.70	0.67
Rock Hall	0.16	0.38	2.19	1.13

Table S3. Earth hematite samples used for analysis. Maximum paleotemperatures, were derived from illite-smectite paleothermometry (*4, 63, 64*). Depths are reported only for samples collected as core materials; all others are surface samples.

Location	Latitude	Longitude	Depth (m)	Sample names	Max paleotemp. (ºC)
Lithuania	55° 35′ 4.35″ N	26° 31′ 57.40″ E	738.1	SAS-9	103
			737.4	SAS-11	
			634.8	SAS-17A	
			634.8	SAS-17AKD	
			634.0	SAS-18	
			630.6	SAS-20A	
			628.0	SAS-21A	
	55° 40′ 19.96″ N	25° 23′ 0.02″ E	825.0	Svedesai 252-4	123
	55° 31′ 12″ N	26° 28′ 12″ E	636.9	TVE-5	111
			636.4	TVE-6	
			496.0	TVE-11	
	54° 26′ 43.13″ N	25° 26′ 26.11″ E	526.0	VIL-5	117
			524.0	VIL-6	
			520.2	VIL-9	
			515.2	VIL-10	
			416.0	VIL-15	
			416.0	VIL-15KD	
			412.0	VIL-16	
	54° 16′ 56″ N	24° 35′ 18″ E	404.0	GLU-5	121
	55° 40′ 0.12″ N	26° 31′ 59.88″ E	623.9	Druksiai-324/1	ca. 110
			633.0	Druksiai-324/2	
			639.1	Druksiai-324/3	
			651.0	Druksiai-324/4	
			663.1	Druksiai-324/5	
			623.9	DRU-1KD	
			633.0	DRU-2KD	
	55° 40′ 33.6″ N	25° 22′ 30.0″ E	383.5	Visikiai-68-1	ca. 110
			410.5	Visikiai-68-2	
Estonia	59° 15′ 31″ N	26° 7′ 49″ E	333.0	Meta-7	ca. 120
			333.0	Meta-7KD	
			309.0	Meta-8	
			297.8	Meta-11	
Russia, St Petersburg	60° 33′ 15″ N	33° 14′ 53″ E	150.8	Shotkus-4	128
			252.6	Shotkus-17	
Russia, Archangelsk	61° 51′ N	40° 27′ E	112.8	M-1/31	93
			113.2	M-1/32	
			114.8	M-1/36	
	64° 00′ N	40° 30′ E	26.0	3P-26	93
			40.0	3P-40	
Ukraine, Podolia	46° 36′ 36.9″ N	27° 12′ 2.9″ E	1.0	Zarnivka-2	152
			1.7	Zarnivka-3	
			2.5	Zarnivka-4	
	48° 47′ 71.0″ N	27° 16′ 65.1″ E	0	Struha-1	156
			0	Struha-12	
	48° 35′ 30.5″ N	27° 27′ 95.6″ E	2.8	Tama-9	151
			4.5	Tama-10	

Table S3. Cont.

Location	Latitude	Longitude	Depth (m)	Sample names	Max paleotemp. (ºC)
Poland	52° 52′ 34.22″ N	23° 41′ 26.44″ E	746.7	Ochrymy-5	135
			738.8	Ochrymy-16	
	51° 37′ 13.42″ N	23° 21′ 24.46″ E	1450.1	Kaplonosy-1	148
			1450.9	Kaplonosy-2	
			1449.8	Kaplonosy-3	
			1448.7	Kaplonosy-4	
			1445.2	Kaplonosy-5	
			1444.2	Kaplonosy-6	
			1441.5	Kaplonosy-7	
			1437.6	Kaplonosy-8	
	50° 58′ 52.32″ N	23° 44′ 16.68″ E	2959.1	Bialopole-4	148
			2958.8	Bialopole-5	
			2958.4	Bialopole-6	
Ukraine, Volyn	51° 9′ 31.12″ N	25° 50′ 8.43″ E	96.5	4519-37	94
			95.0	4519-38	
			93.3	4519-39	
			92.3	4519-40	
			91.1	4519-41	
	51° 44′ 20″ N	24° 24′ 20″ E	286.0	4591-OA	ca. 120
			286.0	4591-1	
			285.6	4591-2	
	51° 41′ 25″ N	24° 18′ 18″ E	285.0	4504-8KD	105
			281.0	4504-9KD	
			278.0	4504-11KD	
	51° 14′ 05″ N	25° 43′ 28″ E	205.4	4592-2	105
			201.8	4592-4n-022KD	
	51° 30′ 10″ N	24° 33′ 30″ E	162.0	4517-4	119
	50° 15' 26.4" N	26° 53' 46.7" E		Tashky-1	hydrothermal
				Tashky-3	
				Tashky-5	
				Tashky-6	
				Tashky-8	
				Tashky-9	
				Tashky-10	
Belarus	52° 22′ 7.67″ N	24° 41′ 9.83″ E	776.0	Kob-4	hydrothermal
			716.3	Kob-17	
			679.5	Kob-21	
			614.5	Kob-27A	
			552.5	Kob-32	
			530.0	Kob-33	
			508.4	Kob-37AiBKD	
	52° 6′ 55.18″ N	26° 50′ 4.79″ E	698.0	Pinsk-39	hydrothermal
	51° 40′ 46″ N	24° 5′ 7″ E	232.0	Mal-1	99
	53° 47′ 4.34″ N	30° 20′ 28.65″ E	478.0	Vilch-12	103

Table S3. Cont.

Location	Latitude	Longitude	Depth (m)	Sample names	Max paleotemp. (ºC)
Holy Cross Mts. - Devonian	50° 47' 50" N	20° 33' 56" E		Kow-47 Kow-49	120
Tatra Mts. -Triassic	49° 14′ 20″ N	19° 48′ 54″ E		IWA-2 IWA-3	180-270
	49° 13′ 38″ N	19° 53′ 54″ E		TOM-4 TOM-6	180-270
	49° 13′ 26″ N	19° 53′ 1″ E		Cz.Z-12 Cz.Z-15	180-270
Velebit Mts. - Triassic	44° 31' 5" N	15° 12' 59" E		Vel-21	180-250
Island of Hawaii, HI, Maunakea volcano, erosional gully, Pu'u Poliahu cinder cone				HW13MK001 HW13MK011A HW13MK030 HW13MK030B HW13MK030D HW13MK030Drill	hydrothermal
Island of Hawaii, HI, Maunakea volcano, float rock from Pu'u Poliahu, gully entrance				HWMK125	hydrothermal
Island of Hawai'i, HI, Maunakea volcano, summit switchback				HWMK011_LT1000_FP	hydrothermal
Island of Hawai'i, HI, Maunakea volcano, Subaru cone				HWMK020_LT0005	hydrothermal
Island of Hawai'i, HI, Maunakea volcano, cone W of Pu'u Poliahu				HWMK030_0500-1000_FP	hydrothermal
Island of Hawai'i, HI, Maunakea volcano, unnamed cone SW of Visitor's Center				HWMK759_FP	hydrothermal
Island of Maui, HI, Haleakula volcano, within summit cone				MUHL904_LT1000	hydrothermal

Table S4. Volume-weighted mean crystallite sizes (LVol, in nm) for hematite reflections (104) and (110) calculated from XRD peak broadening of natural hematite. σ $LVol_{(104)}$ and σ $LVol_{(110)}$ denote the corresponding standard uncertainties.

	Sample name	$LVol_{(104)}$	σ $LVol_{(104)}$	$LVol_{(110)}$	σ $LVol_{(110)}$
	SAS-9	20.0	3.8	38.1	3.6
	SAS-11	18.3	3.0	41.9	3.7
	SAS-17A	14.0	1.3	49.5	4.2
	SAS-17AKD	11.1	0.6	48.9	8.7
	SAS-18	10.7	0.4	35.2	2.3
	SAS-20A	10.8	0.5	31.3	2.9
	SAS-21A	15.4	0.6	74.2	11.4
	Svedesai 252-4	14.5	0.6	52.8	12.9
	TVE-5	20.8	0.8	53.9	8.6
	TVE-6	28.1	1.2	46.5	9.0
	TVE-11	9.8	0.3	45.8	4.3
	VIL-5	18.5	2.8	48.5	4.2
Lithuania	VIL-6	15.8	1.5	47.7	5.7
	VIL-9	14.0	0.5	63.2	7.4
	VIL-10	15.4	1.8	60.3	10.3
	VIL-15	9.8	1.3	49.5	7.6
	VIL-15KD	11.7	1.7	55.1	9.1
	VIL-16	12.9	1.0	46.9	8.0
	GLU-5	14.5	1.9	50.0	5.8
	Druksiai-324/1	10.4	1.6	37.8	9.2
	Druksiai-324/2	14.2	3.4	42.0	6.4
	Druksiai-324/3	9.5	1.5	45.1	4.0
	Druksiai-324/4	11.8	0.6	43.9	4.8
	Druksiai-324/5	10.8	0.6	46.6	5.8
	Visikiai-68-1	11.8	0.6	42.1	4.8
	Visikiai-68-2	13.1	0.7	47.7	6.5
	DRU-1KD	10.8	0.9	51.3	7.7
	DRU-2KD	10.8	1.0	54.8	11.3
	Meta-7	15.1	0.7	45.3	5.1
Estonia	Meta-7KD	14.7	1.3	59.1	4.2
	Meta-8	18.4	0.9	56.3	6.9
	Meta-11	13.2	1.2	47.6	4.0
Russia,	Shotkus-4	19.8	1.7	53.1	3.1
St Petersburg	Shotkus-17	29.4	6.8	82.1	5.9
	M-1/31	20.3	1.5	43.2	3.4
Russia,	M-1/32	25.3	2.7	38.2	11.1
Archangelsk	M-1/36	20.7	1.1	38.9	5.3
	3P-26	16.9	1.4	54.9	1.5
	3P-40	24.0	3.5	45.4	5.0
	Zarnivka-2	25.4	1.5	61.9	12.3
	Zarnivka-3	22.6	1.1	60.7	9.1
Ukraine,	Zarnivka-4	25.8	6.2	50.7	3.0
Podolia	Struha-1	25.7	9.3	47.9	7.8
	Struha-12	43.9	9.8	71.3	29.6
	Tama-9	38.0	7.6	60.0	8.4
	Tama-10	48.1	1.6	51.0	7.1
	Ochrymy-5	41.3	2.3	51.2	4.8
	Ochrymy-16	56.2	4.3	68.4	14.1
	Kaplonosy-1	25.6	1.1	45.1	10.1
	Kaplonosy-2	35.4	1.3	60.9	4.9
	Kaplonosy-3	22.7	0.9	39.7	3.8
Poland	Kaplonosy-4	29.9	4.1	49.1	7.2

Table S4. Cont.

	Sample name	$LVol_{(104)}$	$\sigma LVol_{(104)}$	$LVol_{(110)}$	$\sigma LVol_{(110)}$
	Kaplonosy-5	21.3	1.2	44.7	5.3
	Kaplonosy-6	21.4	0.8	47.2	3.8
	Kaplonosy-7	24.0	0.9	35.4	2.4
	Kaplonosy-8	26.2	1.0	51.0	11.7
	Bialopole-4	37.9	2.8	26.5	3.9
	Bialopole-5	18.4	1.0	54.0	6.6
	Bialopole-6	17.5	0.8	51.2	6.4
	4519-37	41.6	1.8	53.0	12.7
	4519-38	25.8	1.9	24.7	7.0
	4519-39	40.4	3.0	44.0	5.1
	4519-40	28.4	2.2	38.9	9.9
	4519-41	36.3	3.4	41.7	11.9
	4591-OA	31.5	3.1	46.0	9.3
	4519-1	28.9	3.2	37.1	19.0
	4591-2	38.2	4.2	53.5	6.9
Ukraine,	4504-8KD	11.8	0.7	46.2	4.4
Volyn	4504-9KD	11.4	0.7	47.3	4.6
	4504-11KD	12.1	0.8	38.3	4.3
	4592-4n-022KD	24.2	1.1	73.2	7.3
	4592-2	18.4	1.3	38.0	3.6
	4517-4	13.8	0.9	21.3	1.4
	Tashky-1	23.7	3.7	55.8	15.9
	Tashky-3	34.6	4.1	38.6	5.3
	Tashky-5	33.3	8.3	38.0	9.0
	Tashky-6	30.8	3.3	36.9	15.0
	Tashky-8	39.6	5.1	37.8	5.2
	Tashky-9	25.6	2.8	57.3	19.8
	Tashky-10	25.2	3.1	61.9	18.8
	Kob-4	53.9	3.6	52.1	6.4
	Kob-17	39.1	2.7	36.9	6.6
	Kob-21	43.2	5.8	43.0	5.3
	Kob-27A	35.1	4.1	52.7	4.8
Belarus	Kob-32	16.6	1.6	47.1	4.6
	Kob-33	17.7	1.7	50.5	3.8
	Kob-37AiBKD	12.1	0.3	53.5	3.7
	Pinsk-39	25.7	2.5	47.7	9.6
	Mal-1	11.0	4.0	45.2	5.3
	Vilch-12	12.8	4.0	54.4	10.4
Holy Cross					
Mts. -	Kow-47	4.3	2.4	29.5	15.7
Devonian	Kow-49	4.8	4.5	35.4	16.2
	IWA-2	27.6	3.2	36.4	11.2
	IWA-3	46.1	6.5	55.0	19.0
Tatra Mts. -	TOM-4	26.8	5.1	62.3	18.8
Triassic	TOM-6	27.5	4.5	51.1	15.1
	Cz.Z-12	21.7	2.2	46.2	14.1
	Cz.Z-15	26.6	5.0	56.6	14.4
Velebit Mts. -					
Triassic	Vel-21	40.9	3.5	58.8	12.9

Table S4. Cont.

	Sample name	$LVol_{(104)}$	$\sigma LVol_{(104)}$	$LVol_{(110)}$	$\sigma LVol_{(110)}$
Hawaii gray hematite[1]	HW13MK001	151.2	6.2	2233.6	1718014.2[2]
	HW13MK011A	74.9	3.3	2233.6	1806413.9
	HW13MK030	146.2	7.2	2233.6	1908067.5
	HW13MK030B	84.5	3.0	2233.6	2120027.5
	HW13MK030D	129.4	5.0	2233.6	1826476.7
	HW13MK030Drill	136.3	4.7	2233.6	1882256.4
	HWMK125	84.4	3.0	2233.6	2120935.0
Hawaii red hematite	HWMK011_LT1000_FP	39.7	11.7	16.6	15.3
	HWMK020_LT0005	16.9	1.2	19.9	2.6
	HWMK030_0500-1000_FP	38.8	8.7	42.6	28.8
	HWMK759_FP	34.5	5.8	25.0	4.4
	MUHL904_LT1000	24.9	1.3	28.6	2.4

[1]crystallite sizes for gray hematite are not shown in Fig. 2B, the large errors are because there is no additional broadening caused by crystallite sizes for (110) peak.

Table S5. Calculated effective equilibrium concentration of hematite at pH 2 to 7 in anion-free solution and in solutions containing chloride or sulfate.

pH	$C_{eff\infty}$, mol mm^{-3} anion-free solution	$C_{eff\infty}$, mol mm^{-3} 2.6 mol kg^{-1} Cl^-	$C_{eff\infty}$, mol mm^{-3} 0.33 mol kg^{-1} SO_4^{2-}
7	$2.56x10^{-20}$	$2.26x10^{-20}$	$2.63x10^{-20}$
6	$3.78x10^{-20}$	$3.90x10^{-20}$	$4.50x10^{-20}$
5	$1.63x10^{-19}$	$2.18x10^{-19}$	$2.44x10^{-19}$
4	$1.58x10^{-18}$	$5.91x10^{-18}$	$5.14x10^{-18}$
3	$3.47x10^{-17}$	$2.98x10^{-15}$	$2.14x10^{-15}$
2	$4.00x10^{-15}$	$2.85x10^{-12}$	$1.54x10^{-12}$

Table S6. Parameters used in Eqs. S2 and S3 for calculation of crystallite growth time.

Parameter	Value	Reference
D_{eff}	3.16 mm^2 yr^{-1}	(*34*)
γ_1	$1.2x10^{-6}$ J mm^{-2}	Bulk hematite (*65*)
γ_2	$3.33x10^{-7}$ J mm^{-2}	10 nm nanoparticles (*66*)
$R_m(0)$	$2.5x10^{-6}$ mm	Mean radius of crystallite in Duluth (Table S1)
$R_m(t)$	$32.5x10^{-6}$ mm	Mean radius of crystallite in Confidence Hills (Table S1)
υ	$3.03x10^4$ mm^3 mol^{-1}	
R	8.31 J mol^{-1} K^{-1}	
T	323 K (50 °C)	

Table S7. Calculated crystallite growth times at different pH for two interfacial energies (γ_1 = 1.2×10^{-6} J mm^{-2}, γ_2 = 3.33×10^{-7} J mm^{-2}) at 50 °C.

anion-free solution				
pH	time, years (γ_1 =1.2x10^{-6} J mm^{-2})	log(time/yr)	time, years (γ_2 =3.33x10^{-7} J)	log(time/yr)
7	1.16x10^{6}	6.07	4.19x10^{6}	6.62
6	7.87x10^{5}	5.90	2.84x10^{6}	6.45
5	1.83x10^{5}	5.26	6.60x10^{5}	5.82
4	1.88x10^{4}	4.27	6.77x10^{4}	4.83
3	8.58x10^{2}	2.93	3.09x10^{3}	3.49
2	7.44x10^{0}	0.87	2.68x10^{1}	1.43
2.6 mol/kg Cl^{-}				
pH	time, years (γ_1 =1.2x10^{-6} J mm^{-2})	log(time/yr)	time, years (γ_2 =3.33x10^{-7} J mm^{-2})	log(time/yr)
7	1.32x10^{6}	6.12	4.75x10^{6}	6.68
6	7.62x10^{5}	5.88	2.75x10^{6}	6.44
5	1.37x10^{5}	5.13	4.92x10^{5}	5.69
4	5.04x10^{3}	3.70	1.81x10^{4}	4.26
3	9.99x10^{0}	1.00	3.60x10^{1}	1.56
2	1.04x10^{-2}	-1.98	3.76x10^{-2}	-1.42
0.33 mol/kg SO$_4^{2-}$				
pH	time, years (γ_1 =1.2x10^{-6} J mm^{-2})	log(time/yr)	time, years (γ_2 =3.33x10^{-7} J mm^{-2})	log(time/yr)
7	1.13x10^{6}	6.05	4.07x10^{6}	6.61
6	6.61x10^{5}	5.82	2.38x10^{6}	6.38
5	1.22x10^{5}	5.09	4.39x10^{5}	5.64
4	5.78x10^{3}	3.76	2.08x10^{4}	4.32
3	1.39x10^{1}	1.14	5.00x10^{1}	1.70
2	1.93x10^{-2}	-1.71	6.94x10^{-2}	-1.16

Table S8. Elevation and distance from the near-landing site (0 km on the x-axis in FIG. 5) for key stratigraphic horizons in the Murray formation.

Location	Elevation, m (FIG. 1A)	Distance, km [(*21*), their figure 4B]
beginning of the Murray formation	-4460	~5.7
Murray/Carolyn Shoemaker transition	-4140	~11
Carolyn Shoemaker/ Mirador transition	-4040	~12